A SPIN- AND ANGLE-RESOLVED PHOTOEMISSION STUDY OF COUPLED SPIN-ORBITAL TEXTURES DRIVEN BY GLOBAL AND LOCAL INVERSION SYMMETRY BREAKING

Lewis Bawden

A Thesis Submitted for the Degree of PhD
at the
University of St Andrews

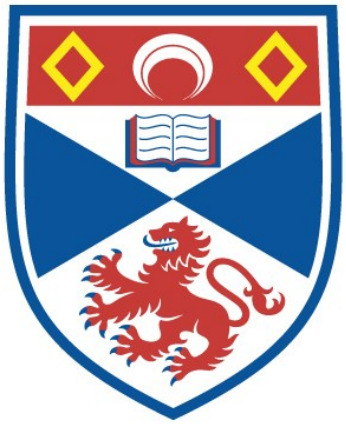

2017

A spin- and angle-resolved photoemission study of coupled spin-orbital textures driven by global and local inversion symmetry breaking

Author:
Lewis Bawden

Supervisor:
Dr. Phil D. King

University of
St Andrews

A thesis submitted in fulfilment of the requirements for the degree of Doctor of Philosophy in Physics

at the

University of St Andrews

October 19, 2017

Declaration of Authorship

1. Candidate's declarations:

I, Lewis Bawden, hereby certify that this thesis, which is approximately **37,000** words in length, has been written by me, and that it is the record of work carried out by me, or principally by myself in collaboration with others as acknowledged, and that it has not been submitted in any previous application for a higher degree. I was admitted as a research student in 09/2013 and as a candidate for the degree of Doctor of Philosophy in Physics completed by 07/2017; the higher study for which this is a record was carried out in the University of St Andrews between 2013 and 2017.

Date ..... signature of candidate .....

2. Supervisor's declarations:

I hereby certify that the candidate has fulfilled the conditions of the Resolution and Regulations appropriate for the degree of Doctor of Philosophy in Physics in the University of St Andrews and that the candidate is qualified to submit this thesis in application for that degree.

Date ..... signature of supervisor .....

3. Permission for publication: (to be signed by both candidate and supervisor)

In submitting this thesis to the University of St Andrews I understand that I am giving permission for it to be made available for use in accordance with the regulations of the University Library for the time being in force, subject to any copyright vested in the work not being affected thereby. I also understand that the title and the abstract will be published, and that the title and the abstract will be published, and that a copy of the work may be made and supplied to any bona fide library or research worker, that my thesis will be electronically accessible for personal or research use unless exempt by award of an embargo as requested below, and that the library has the right to migrate my thesis into new electronic forms as required to ensure continued access to the thesis. I have obtained any third-party copyright permissions that may be required in order to allow such access and migration, or have requested the appropriate embargo below.

The following is an agreed request by candidate and supervisor regarding the publication of this thesis:

PRINTED COPY
No embargo on print copy

ELECTRONIC COPY
No embargo on electronic copy

Date ..... signature of candidate .....

Date ..... signature of supervisor .....

"Well you know what they say, persistence is its own reward"

Oliver J. Clark

Abstract

The effect of spin-orbit coupling had once been thought to be a minor perturbation to the low energy band structure that could be ignored. Instead, a surge in recent theoretical and experimental efforts have shown spin-orbit interactions to have significant consequences. The main objective of this thesis is to investigate the role of the orbital sector and crystal symmetries in governing the spin texture in materials that have strong spin-orbit interactions. This can be accessed through a combination of spin- and angle-resolved photoemission spectroscopy (ARPES and spin-ARPES), both of which are powerful techniques for probing the one-electron band structure plus interactions, and supported by density functional theory calculations (DFT).

We focus first on a globally inversion asymmetric material, the layered semiconductor BiTeI, which hosts a giant spin-splitting of its bulk bands. We show that these spin-split bands develop a previously undiscovered, momentum-space ordering of the atomic orbitals. We demonstrate this orbital texture to be atomic element specific by exploiting resonant enhancements in ARPES. These orbital textures drive a hierarchy of spin textures that are then tied to the constituent atomic layers. This opens routes to controlling the spin-splitting through manipulation of the atomic orbitals.

This is contrasted against a material where inversion symmetry is globally upheld but locally broken within each monolayer of a two layer unit cell. Through our ARPES and spin-ARPES measurements of 2H-$NbSe_2$, we discover the first experimental evidence for a strong out-of-plane spin polarisation that persists up to the Fermi surface in this globally inversion symmetric material. This is found to be intrinsically linked to the orbital character and dimensionality of the underlying bands. So far, previous theories underpinning this (and related) materials' collective phases assume a spin-degenerate Fermi sea. We therefore expect this spin-polarisation to play a role in determining the underlying mechanism for the charge density wave phase and superconductivity.

Through these studies, this thesis then develops the importance of global versus local inversion symmetry breaking and uncovers how this is intricately tied to the underlying atomic orbital configuration.

Acknowledgements

A PhD is without question an enormous undertaking and while the work I'm presenting is my own, it would not have been at all possible without the help of many others.

I would first like to thank my supervisor Phil King without whom none of this would have been possible. He always knew when to push and when to relax making these last four years a great balance between being productive and enjoyable. It's been very satisfying seeing the group grow from just the three of us into one that is now well established (and even now it's hard to keep Phil away from a beamtime!). I feel privileged to have been a part of it. I greatly appreciate all the support and mentoring over the years.

Comfortable and efficient round the clock operation of a beamtime would simply not be possible without the help of a great team and so thank you to everyone who participated in acquiring measurements for the beamtimes we've been on over the years. They have been some of the best times of the PhD largely thanks to the support and dedication of the team, as well as keeping each other sane and just having fun! There have been many beamtimes with many different people including mainly our group itself, our good collaborators in Justin's group at NTNU, and our collaborators at Aarhus. A special thanks to Jon, Oliver, Veronika, Federico, Simon, Maciek and Matteo, who contributed an enormous amount (in both the science and enjoyment) to so many of the beamtimes. Things like the beamtime playlist, our special MaxLab cooling system, and the multiple 'airport specials' are the sorts of things that made them great.

While academia is a lot of work, it's important that it's not all work, or both your work and wellbeing suffer. So next, a huge thanks goes to all my friends, family and drinking buddies who have kept me grounded (and put up with my inane dry sense of humour, especially Oliver for having to share an office with me for so long). The whole pie and/or pint crew of St Andrews Physics, our Physics badminton crew, and anyone along the way who contributed to my continuing sanity, even those outside of St Andrews: Henry, Alex, Alex, John and Dan.

Finally, it's no exaggeration to say this would not have been possible without my amazing girlfriend (mijn schattige lief) certainly in the last few stressful, dense months of writing (although even before that period, the fun we had together when we should have been working was really great!). Thank you so much for all your support, cooking with me so I could destress and work late, walks and picnics, hug attacks and teas and laughs and silly faces and generally being amazing every step of the way. I really hope I can repay you when it's your turn!

Thank you everyone!

List of Papers

1. **Highly Anisotropic electronic structure of ReS_2**
   D. Biswas, A. Ganose, R. Yano, J. M. Riley, L. Bawden, O. J. Clark, J. Feng, L. Collins-McIntyre, W. Meevasana, T. K. Kim, M. Hoesch, J. Rault, T. Sasagawa, D. O. Scanlon and P. D. C. King.
   arXiv:1703.04725 - Submitted

2. **Ubiquitous formation of type-II bulk Dirac cones and topological surface states from a single orbital manifold in transition-metal dichalcogenides**
   M. S. Bahramy, O. J. Clark, B.-J. Yang, J. Feng, L. Bawden, J. M. Riley, I. Marković, F. Mazzola, V. Sunko, D. Biswas, S. P. Cooil, M. Jorge, J. W. Wells, M. Leandersson, T. Balasubramanian, J. Fujii, I. Vobornik, J. Rault, T. K. Kim, M. Hoesch, G. Balakrishnan, K. Okawa, M. Asakawa, T. Sasagawa, T. Eknapakul, W. Meevasana and P. D. C. King.
   arXiv:1702.08177 - Submitted

3. **Maximal Rashba-like spin splitting via kinetic energy-driven inversion symmetry breaking**
   V. Sunko, H. Rosner, P. Kushwaha, S. Khim, F. Mazzola, L. Bawden, O. J. Clark, J. M. Riley, D. Kasinathan, M. W. Haverkort, T. K. Kim, M. Hoesch, J. Fujii, I. Vobornik, A. P. Mackenzie, and P. D. C. King.
   Submitted

4. **Nearly-free-electron system of monolayer Na on the surface of single-crystal $HfSe_2$**
   T. Eknapakul, I. Fongkaew, S. Siriroj, R. Vidyasagar, J. D. Denlinger, L. Bawden, S.-K. Mo, P. D. C. King, H. Takagi, S. Limpijumnong, and W. Meevasana.
   Physical Review B **94**, 201121(R), (2016).

5. **Spin-valley locking in the normal state of a transition-metal dichalcogenide superconductor**
   L. Bawden, S. P . Cooil, F . Mazzola, J. M. Riley , L. J. Collins-McIntyre, V . Sunko, K. Hunvik, M. Leandersson, C. Polley, T. Balasubramanian, T. Kim, M. Hoesch, J. W. Wells, G. Balakrishnan, M. S. Bahramy, and P. D. C. King.
   Nature Communications **7**, 11711, (2016).

6. **Negative electronic compressibility and tuneable spin splitting in WSe_2**
   J. M. Riley, W. Meevasana, L. Bawden, M. Asakawa, T. Takayama, T. Eknapakul, T. K. Kim, M. Hoesch, S.-K. Mo, H. Takagi, T. Sasagawa,

M. S. Bahramy and P. D. C. King.
Nature Nanotechnology **10**, 1043-1047, (2015).

7. **Nearly free electrons in a 5d delafossite oxide metal.**
P. Kushwaha, V. Sunko, P. J. W. Moll, L. Bawden, J. M. Riley, N. Nandi, H. Rosner, M. P. Schmidt, F. Arnold, E. Hassinger, T. K. Kim, M. Hoesch, A. P. Mackenzie, and P. D. C. King.
Science Advances **1**, 1500692, (2015).

8. **Hierarchical spin-orbital polarization of a giant Rashba system.**
L. Bawden, J. M. Riley, C. H. Kim, R. Sankar, E. J. Monkman, D. E. Shai, H. I. Wei, E. Lochocki, J. W. Wells, W. Meevasana, T. K. Kim, M. Hoesch, Y. Ohtsubo, P. Le Fèvre, C. J. Fennie, K. M. Shen, F. Chou and P. D. C. King.
Science Advances **1**, 1500495, (2015).

9. **Direct observation of spin-polarized bulk in an semiconductor bulk inversion-symmetric**
J. M. Riley, F. Mazzola, M. Dendzik, M. Michiardi, T. Takayama, L. Bawden, C. Granerød, M. Leandersson, T. Balasubramanian, M. Hoesch, T. K. Kim, H. Takagi, W. Meevasana, Ph. Hofmann, M. S. Bahramy, J. W. Wells, and P. D. C. King.
Nature Physics **10**, 835-839, (2014).

Contents

List of Figures

Chapter 1

Motivation

1.1 Importance of the spin-orbit interaction

How electrons behave in the solid state is one of the most fundamental and important questions in condensed matter. It has underpinned a great deal of theoretical progress and technological applications in the last century such as the now ubiquitous field effect transistor (FET) and multiple Nobel prizes. One active vein of research has then been to attempt to surpass the intrinsic limit in efficiency imposed by the heat dissipation and size restrictions in conventional semiconductor FETs. A possible route is through the ability to manipulate the spin degree of freedom that electrons possess. However, in the solid state, there is a degeneracy of the spin-up and spin-down electrons enforced by two symmetries: inversion symmetry and time reversal symmetry. It is well known that application of a magnetic field can lift the inherent spin-degeneracy, breaking time reversal symmetry within a Stoner picture (fig. 1.1b). On the other hand, a spin-splitting can be achieved without magnetism through breaking inversion symmetry in the solid state, in combination with spin-orbit coupling. This is a relativistic effect that has historically often been neglected but now is experiencing a resurgence in condensed matter in pure academic research and technological applications alike [1].

Through the spin-orbit interaction, an electron moving relativistically through an electric field can experience this in its own rest frame as an effective magnetic field. This effective magnetic field (the spin-orbit field), can

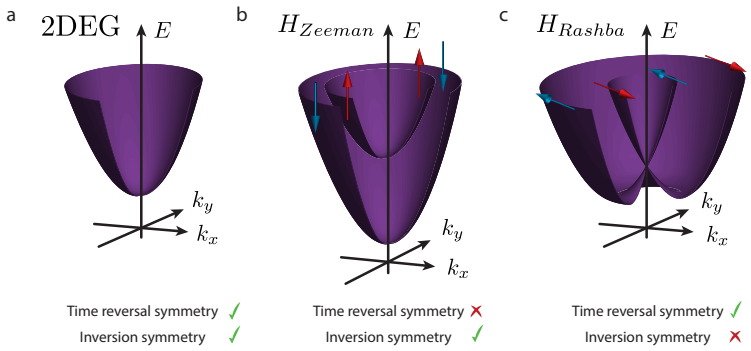

FIGURE 1.1: a) Nearly-free electronic dispersion relation for a parabolic band with spin-degenerate electrons. b) Zeeman splitting from an applied magnetic field, breaking time reversal symmetry but preserving inversion symmetry. Electrons spin-polarised in the z direction c) Rashba splitting from a broken inversion symmetry (and preserved time reversal symmetry). Electrons spin-polarised in the x-y plane according to the spin-orbit field.

then couple to the intrinsic magnetic moment the electron possessess, related to its spin. In the solid state, in the presence of an inversion symmetry breaking, spin-orbit interactions can lift the inherent spin-degeneracy, often through the so-called Rashba effect [2]. In the case of inversion symmetry breaking normal to the sample surface, Rashba spin-splitting leads to states spin-polarised within the sample plane (fig. 1.1c).

This spin-splitting without magnetism is then a key ingredient in a concept device which would surpass the conventional semiconductor FET. The idea proposed by Datta and Das was a spin-FET [3] (fig. 1.2). Spin-polarised contacts are used to inject and detect spins (the source and drain) of a given orientation and a semiconductor with strong spin-orbit coupling is used as the gated channel. The gate then provides a tuneable electric field which induces a tuneable spin-splitting through the Rashba effect. A spin-splitting is required such that there is a precession of the electron's spin in the spin-orbit field through the gated channel (in analogy to Larmor precession in a magnetic field). The channel length and the gate voltage (or equivalently the spin-splitting) then dictate the precession length. Spin-precession of multiples of 2π then equate to a current being detected as the spin will have precessed such that it is parallel with the drain spin (as in fig. 1.2). Suitable

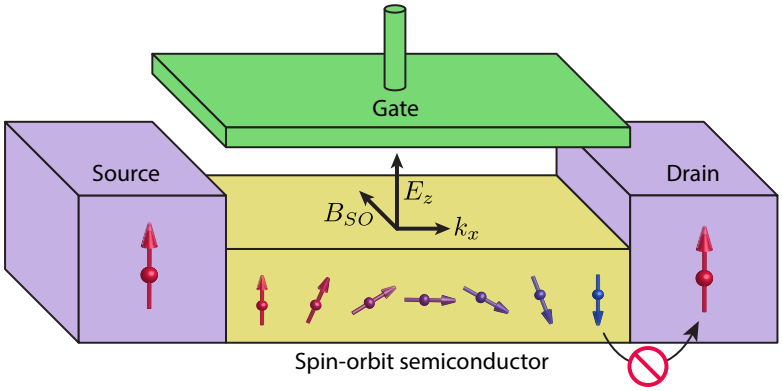

FIGURE 1.2: A schematic spin field-effect-transistor (spin-FET) according to Datta and Das [3]. Spin-polarised source injects spins that are polarised in the z direction, which travel through the semiconducting channel with momentum k_x. These precess in the x-z plane according to the spin-orbit field B_{SO}, induced by the electric field E_z supplied by the gate voltage. These can be detected in the spin-polarised drain if they have precessed such they align with the drain spin-polarisation. The precession is proportional to the spin-splitting, which is tuneable by the gate voltage.

candidates for the spin-orbit semiconducting channel have renewed interest in spin-orbit coupling in materials, with an emphasis on understanding and controlling of the size of the spin-splitting (a comprehensive review on spin-splitting at surfaces has been published by Krasovskii [4]).

In addition to this more device oriented application, the spin-orbit interaction has prompted a surge of interest as the key ingredient in stabilising a novel form of spin-polarised state: topological surface states [5, 6]. States existing as a product of the topology of the material have been known about for some time, for example due to the quantum Hall effect [7, 8]. A bulk material under an applied magnetic field, quantises the electron motion in the bulk (normal to the applied field) into cyclotron orbits corresponding to their Landau levels. However, at the edge these cyclotron orbits cannot be formed and instead intersect with the boundary. These then form a single conducting skipping mode around the edge of the material (fig. 1.3b). This has the properties that it is chiral, with a handedness imposed by the magnetic field. Additionally, it is a topological property, so the shape of the material is unimportant: simply that the electrons are in cyclotron orbits in the bulk means skipping modes will exist along the edge regardless of its

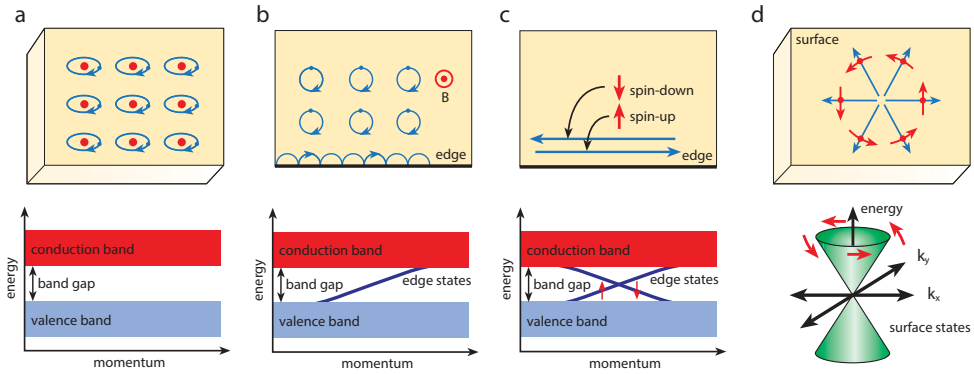

FIGURE 1.3: a) An example band insulator having a gap between the conduction and valence bands. b) Quantum Hall insulator with cyclotron orbits in the bulk and 'skipping' modes along the edge induced by the magnetic field applied perpendicular to the surface. This gives a single metallic state bridging the band gap with a positive group velocity (in this example). c) Quantum spin-Hall state, where spin-orbit coupling is necessary. Spin-up and spin-down electrons have opposite momentum in the edge modes according to time reversal symmetry, leading to two metallic states that are spin-polarised bridging the gap. d) This effect in the bulk leads to the well-known in-plane spin-polarised Dirac cones of topological insulator surface states. Adapted from [5].

shape or any deformations. It was later shown that a similar effect can lead to topological surface states in certain materials even without an applied magnetic field, as a consequence of spin-orbit interactions and time reversal symmetry.

In such materials, spin-orbit coupling can drive an inversion of bands with different parity in the bulk. If the bulk material with an inverted band gap is interfaced with a material with a non-inverted band gap (e.g. the topologically trivial vacuum), then conducting states must exist at the interface between these materials. There is then a single state at the surface which connects the bulk bands of opposite parity at the interface. Since this is a spin-orbit effect, the electron spin degeneracy is lifted for these surface states in a way which preserves time reversal symmetry. This implies that a spin-up electronic state with positive momentum at the surface, necessitates a spin-down electronic state with negative momentum at the surface (fig. 1.3c). Topological surface states with opposite momentum are then not spin-degenerate. There is a spin-polarised gapless surface state bridging the

bulk band gap, which is protected as a property of the interface between two materials with a different $\mathbb{Z}_2$ topological invariant (a quantity describing topologically trivial or non-trivial materials). The spin-orbit interaction additionally results in this spin-polarisation being strongly in-plane and chiral, similar to the states in the Rashba model (fig. 1.3d). The difference is that, for a given energy, there are now an odd number of spin-polarised states between time reversal invariant points (fig. 1.3c), as opposed to the even number as with the topologically trivial Rashba spin-split states. By now topological states are rife, even found in materials that have been studied for decades such as bismuth chalcogenide semiconductors [6] and transition metal dichalcogenides [9], both of which are a focus for this thesis.

Spin-orbit coupling has then resulted in a mounting interest in materials with hidden exotic states in the spin and orbital sectors [1]. A detailed understanding of how the spin degree of freedom affects the atomic orbitals and vice versa is therefore vital to making progress. This thesis covers some of our findings on this topic.

1.2 Organisation of thesis

This brings us to a breakdown of how the following chapters of the thesis will unfold.

Chapter 2 gives an outline of some of the important concepts for the behaviour of electrons in solids, including how this can be calculated and interpreted. A key property of a solid is its electronic dispersion relation contained within the one-electron band structure. We show how this can arise by employing a tight binding picture, and then extend the result to real materials by considering surfaces. This chapter then introduces the important symmetry considerations in real materials and what effect the spin-orbit interaction can have in their presence (or absence).

Chapter 3 provides insight into the experimental techniques employed heavily in this thesis: spin- and angle-resolved photoemission spectroscopy

(ARPES). These are techniques that can not only measure the electronic dispersion in a material but additionally probe the interactions with other electrons and the solid itself. Through consideration of the theoretical framework surrounding the photoemission process we show how we can selectively probe the orbital character of the electronic structure. Further, through spin-ARPES, the spin-resolved electronic structure can be inferred. These techniques together provide an insight into the spin-orbit interaction in the materials studied.

Chapter 4 begins by motivating spin-splitting at surfaces and how the spin-splitting can be understood and controlled. We then introduce literature about an entirely new form of Rashba splitting, which has been found to occur in the bulk of a non-centrosymmetric semiconductor BiTeI, a topologically trivial analogue to the bismuth chalcogenide topological insulators. Through our research, we demonstrate that this material hosts a momentum-space ordering of the atomic orbitals, reminiscent of work on its topological counter-part. The chiral ordering of the orbitals, which switches through the Dirac point, makes this effectively an orbital-analogue of the Rashba effect. This shows that there are consequences of the spin-orbit interaction beyond the conventional expectation for the spin degree of freedom, potentially offering manipulation of the spin-polarisation and the spin-splitting through the orbital sector.

Chapter 5 focusses on the bulk transition metal dichalcogenide (TMD) $NbSe_2$, a globally centrosymmetric metal with instabilities to a charge density wave and superconducting phase at low temperature. It is shown how bulk TMDs can be understood as multilayer graphene analogues, with broken sublattice symmetry and strong spin-orbit interactions. In these materials, the global inversion symmetry should lead to a complete enforced spin-degeneracy through Kramer's theorem. However, through our research, we show that this material hosts a strong out-of-plane spin-polarisation even in the bulk, arising from a local inversion symmetry breaking within each layer. This suggests the spin to be a relevant quantity to consider in the collective phases, which has previously been overlooked in this material.

Before expanding on the main results underpinning this thesis and their impact on the community, we will therefore start discussing the most fundamental and important concept of how electrons generally behave in solids.

Chapter 2

Scientific Background

2.1 Electrons in solids

To begin to understand the foundations of how electrons behave in solids, relevant theory underpinning our research presented will be summarised. This information is covered in multiple well known textbooks [10–14]: this chapter draws mainly from [12–14]. This thesis will explore the effect of the orbital degree of freedom, and the spin-orbit interaction on electronic structure in solids. A simple and intuitive way to interpret and implement this is through the tight-binding method, and analysis of such models will form part of the results presented.

Understanding and manipulating how the electrons behave is the ultimate goal of condensed matter and a general starting point is the many-particle Schödinger equation:

$$H|\Psi\rangle = E|\Psi\rangle \tag{2.1}$$

where $|\Psi\rangle$ is the wavefunction of the electrons in the solid, E their energy and H is the Hamiltonian of the system. The Hamiltonian describing the kinetic energy and Coulomb interactions between the ions of a lattice and the electrons can be given by [14]:

$$H = \sum_i \frac{\boldsymbol{p}_i^2}{2m_i} + \sum_j \frac{\boldsymbol{P}_j^2}{2M_j} + \frac{1}{2}\sum_{j',j}{}' \frac{Z_j Z_{j'} e^2}{|\boldsymbol{R}_j - \boldsymbol{R}_{j'}|} - \sum_{j,i} \frac{Z_j e^2}{|\boldsymbol{r}_i - \boldsymbol{R}_j|} + \frac{1}{2}\sum_{i',i}{}' \frac{e^2}{|\boldsymbol{r}_i - \boldsymbol{r}_{i'}|} \tag{2.2}$$

where $\boldsymbol{r}_i$ ($\boldsymbol{R}_j$) denotes the position vector of the ith electron (jth nucleus),

$\boldsymbol{p}_i$ ($\boldsymbol{P}_j$) is the momentum operator, m_i (M_j) is the mass of the electron (nucleus), Z_j is the atomic number of the nucleus, and e is the electronic charge. The $\sum'$ indicates to not include the term with identical indices to avoid a divergence (which physically just corresponds to a particle not having a Coulomb interaction with itself). Practically, it is difficult to solve this for all electrons in the system and so we need to make simplifying assumptions. Two such assumptions are often made. The first is that the atomic nuclei of the lattice move slowly (or not at all) compared with the much lighter electrons so these are independent (the adiabatic approximation) [13]. The Hamiltonian (eq. 2.2) can then be separated into parts as such:

$$H = H_{ions}(\boldsymbol{R}_j) + H_e(\boldsymbol{r}_i, \boldsymbol{R}_{j0}) + H_{e-ion}(\boldsymbol{r}_j, \delta\boldsymbol{R}_j), \tag{2.3}$$

where the first term describes purely the ionic part, the second term describes the electronic part for fixed ion positions $\boldsymbol{R}_{j0}$, and the third term describes interactions between electrons and ions (an electron-phonon term), for ions shifted from their equilibrium positions by $\delta\boldsymbol{R}_j$.

Another approximation typically made is that the electrons do not interact with each other, except through the static potential set up in screening the positive charge of the atomic nuclei (the one electron approximation) [13]. This is equivalently described as a mean field approximation, in which the electrons are all said to experience the same averaged potential $V(\boldsymbol{r})$ [14]. Considering just the electronic sector, within the one-electron approximation, the Schödinger equation for each of the n electrons can be written:

$$H_{1e}\Psi_n(\boldsymbol{r}) = \left(\frac{p^2}{2m} + V(\boldsymbol{r})\right)\Psi_n(\boldsymbol{r}) = E_n\Psi_n(\boldsymbol{r}), \tag{2.4}$$

where H_{1e}, $\Psi_n(\boldsymbol{r})$ and E_n denote the one-electron Hamiltonian, the wavefunction and energy of an electron in eigenstate n.

The potential $V(\boldsymbol{r})$ is periodic in space, so solutions to the one-electron Schrödinger equation 2.4 are also periodic and it was realised by Felix Bloch that they could be described by modified plane waves (Bloch functions) of

the form:

$$\Psi_{\boldsymbol{k},n}(\boldsymbol{r}) = u_{\boldsymbol{k},n}(\boldsymbol{r})e^{i\boldsymbol{k}\cdot\boldsymbol{r}} \tag{2.5}$$

where $u_{\boldsymbol{k},n}(\boldsymbol{r})$ is a periodic function for the nth electronic state (ordered by energy) with momentum $\boldsymbol{k}$. These have the periodicity of the Bravais lattice with a lattice vector $\boldsymbol{R}$ such that:

$$u_{\boldsymbol{k},n}(\boldsymbol{r}) = u_{\boldsymbol{k},n}(\boldsymbol{r}+\boldsymbol{R}). \tag{2.6}$$

Consider now the wavefunction at a position $\boldsymbol{r}' = \boldsymbol{r} + \boldsymbol{R}$, and substituting equation 2.6 into equation 2.5, we see:

$$\Psi_{\boldsymbol{k},n}(\boldsymbol{r}+\boldsymbol{R}) = u_{\boldsymbol{k},n}(\boldsymbol{r}+\boldsymbol{R})e^{i\boldsymbol{k}\cdot(\boldsymbol{r}+\boldsymbol{R})} \tag{2.7}$$

$$\implies \Psi_{\boldsymbol{k},n}(\boldsymbol{r}+\boldsymbol{R}) = u_{\boldsymbol{k},n}(\boldsymbol{r})e^{i\boldsymbol{k}\cdot\boldsymbol{r}}e^{i\boldsymbol{k}\cdot\boldsymbol{R}} \tag{2.8}$$

$$\implies \Psi_{\boldsymbol{k},n}(\boldsymbol{r}+\boldsymbol{R}) = e^{i\boldsymbol{k}\cdot\boldsymbol{R}}\Psi_{\boldsymbol{k},n}(\boldsymbol{r}). \tag{2.9}$$

Therefore Bloch functions translated by a lattice vector are equivalent up to a phase factor. Similarly, electrons with momentum $\boldsymbol{k}$ and $\boldsymbol{k}+\boldsymbol{G}$ both satisfy equation 2.5 so the wavevector is not unique, i.e., there are multiple wavevectors which provide the same eigenenergy, i.e. $E(\boldsymbol{k}) = E(\boldsymbol{k}+\boldsymbol{G})$. This then means it is only necessary to consider electrons with a momentum between $\boldsymbol{k} = -\boldsymbol{G}/2, +\boldsymbol{G}/2$ termed the first Brillouin zone in a reduced zone scheme. The amount of k-space necessary to calculate the one-electron eigenstates is dramatically reduced by these approximations, the question now being how is equation 2.4 solved.

2.1.1 Tight Binding Method

Two of the main approaches for understanding how to calculate and interpret these solutions are the nearly free electron model and the tight binding approach. The latter of these two will be discussed in some detail here. The nearly-free electron method gives qualitatively similar results to the tight binding method by considering the kinetic energy part of the

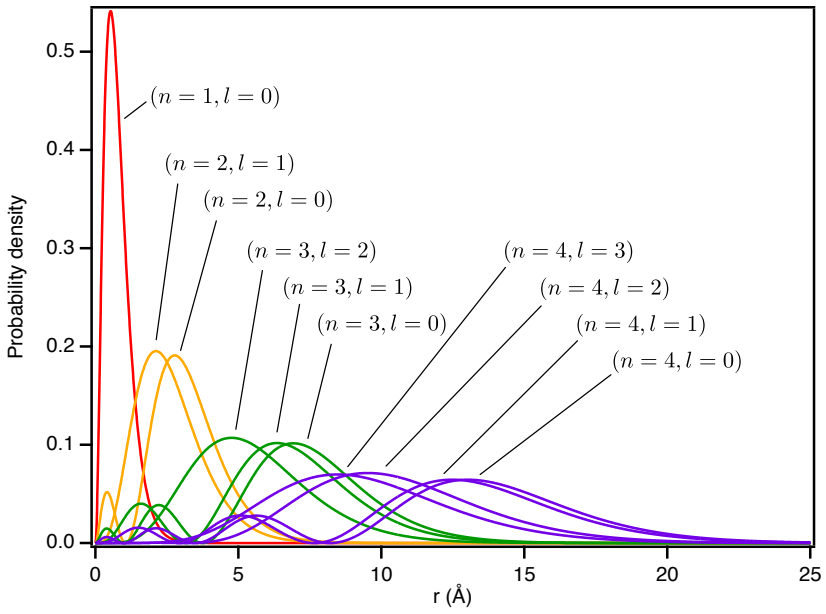

FIGURE 2.1: Probability densities of the radial part of a hydrogen wavefunction [15, 16] for various principle quantum numbers, n, and orbital angular momentum, l. Wavefunctions with larger n are more spatially extended.

Hamiltonian, and applying a crystal potential as a weak perturbation using perturbation theory. The tight binding method considers the opposite scale, where the potential is treated as being strong, with electronic states mostly localised to individual atoms (i.e. tightly bound). This approach will be the focus since theoretical results presented in this thesis (provided by collaborators) derive directly from tight binding models.

When atoms are brought into proximity with each other (e.g. in a lattice), the states of each atom can lower their total energy by forming bonding orbitals when their wavefunctions overlap. Generally, the largest, least bound orbitals have the greatest overlap with neighbouring atoms (fig. 2.1), and therefore contribute the most to the bonding of the atoms within the solid and its electronic properties. The deepest bound core electrons contribute much less to bonding and remain highly localised to a given atom and consequently have negligible electronic dispersion.

With this in mind, a trial wavefunction to solve equation 2.1 can be written as a linear combination of the relevant atomic orbitals (sometimes called

'the LCAO method', which is essentially equivalent to the tight binding method) that contribute to forming bonding and antibonding orbitals:

$$|\Psi_i\rangle = \sum_n c_{i,n}|\phi_n\rangle \tag{2.10}$$

where $|\Psi_i\rangle$ is the ith solution to the Schrödinger equation, expressed as a sum over all the relevant atomic orbitals, $|\phi_n\rangle$, multiplied by a complex coefficient, $c_{i,n}$, which encodes the weight of a given orbital component and the complex phase. Generally, the more orbitals that are included in the model, the better the approximation will be. Given the spatially localised nature of the deep core electrons, it is typically satisfactory to only include orbitals that lie close to the Fermi level: the valence electron states. With this, the Schrödinger equation can then be written as:

$$\sum_{n,m} c^*_{i,m}(\boldsymbol{k})c_{i,n}(\boldsymbol{k})[\langle\phi_m|H(\boldsymbol{k})|\phi_n\rangle - E_i(\boldsymbol{k})\langle\phi_m|\phi_n\rangle] = 0 \tag{2.11}$$

where $\langle\phi_m|H(\boldsymbol{k})|\phi_n\rangle$ is a matrix element of the Hamiltonian, describing hopping from an orbital m to an orbital n (or in the case that $m = n$, this is the onsite orbital energy and crystal field energy). The size of this hopping effectively relates to the bandwidth of a band, with larger hoppings typically corresponding to larger bandwidths. The term $\langle\phi_m|\phi_n\rangle$ is the overlap integral between two orbitals m and n, which in the case of orthogonal orbitals is a Kronecker delta but should in principle be calculated in the case that we have non-orthogonal orbitals. Atomic orbitals are not necessarily orthogonal so there are multiple methods to overcome this, the simplest method being to neglect the overlap which can anyway provide qualitatively reasonable results.

Another method is choosing an orthogonal basis set of orbitals. A popular choice of basis is Wannier orbitals, which are employed for our tight binding results in later chapters. These are an orthonormal set and are

Fourier transforms of Bloch functions [14]. The relation between the Wannier function $a_n(\boldsymbol{r} - \boldsymbol{R}_i)$ and the Bloch function $\Psi_{n\boldsymbol{k}}(\boldsymbol{r})$ is given by:

$$a_n(\boldsymbol{r} - \boldsymbol{R}_i) = N^{-1/2} \sum_{\boldsymbol{k}} e^{-i\boldsymbol{k}\cdot\boldsymbol{R}_i} \Psi_{n\boldsymbol{k}}(\boldsymbol{r}) \tag{2.12}$$

$$\Psi_{n\boldsymbol{k}}(\boldsymbol{r}) = N^{-1/2} \sum_{\boldsymbol{R}_i} e^{i\boldsymbol{k}\cdot\boldsymbol{R}_i} a_n(\boldsymbol{r}; \boldsymbol{R}_i) \tag{2.13}$$

where $\boldsymbol{R}_i$ is a lattice vector, $\boldsymbol{k}$ is the wavevector for the nth state, and N is the number of unit cells in the crystal [14]. Bloch functions consider the wavefunction indexed by a momentum $\boldsymbol{k}$ and are periodic in space. They are spatially extended across the crystal as described in the previous section, since Bloch functions are equivalent for $\boldsymbol{r}' = \boldsymbol{r} + \boldsymbol{R}$, up to a phase factor. Since Wannier functions are the Fourier transform of Bloch functions, these are then well localised to a region close to a lattice vector $(\boldsymbol{r} - \boldsymbol{R}_i)$. So-called maximally-localised Wannier orbitals are then qualitatively very similar to atomic orbitals (since they have minimal spread over multiple lattice sites / atoms), which makes them useful for solutions to tight binding models [17].

Finally, solving the secular equation 2.11 at a selection of $\boldsymbol{k}$-points throughout the Brillouin zone will approximate to the one-electron band structure. The solutions provide eigenenergies or band energies, $E_i(\boldsymbol{k})$, of the i eigenvectors or wavefunctions, $|\Psi_i\rangle$. These wavefunctions, $|\Psi_i\rangle$, contain all the information about the orbital composition of the bands at given $\boldsymbol{k}$-points of each band through the magnitude of the complex coefficients. These wavefunctions can then also be used to project any other important physical quantities such as the expectation of orbital angular momentum for a given eigenfunction at a point in $\boldsymbol{k}$, $\langle \boldsymbol{L} \rangle = \langle \Psi_i(\boldsymbol{k}) | \boldsymbol{L} | \Psi_i(\boldsymbol{k}) \rangle$, or the spin polarisation, $\langle \boldsymbol{S} \rangle = \langle \Psi_i(\boldsymbol{k}) | \boldsymbol{S} | \Psi_i(\boldsymbol{k}) \rangle$, where $\boldsymbol{L}$ and $\boldsymbol{S}$ are the quantum mechanical orbital angular momentum operator and spin angular momentum operator, respectively.

The power of this method is particularly well illustrated by Slater and Koster, who pioneered treating this as an interpolation method [18]. They provide a formalism in which the energy of the hopping (or the extent of the physical overlap) between two orbitals can be determined in a so-called

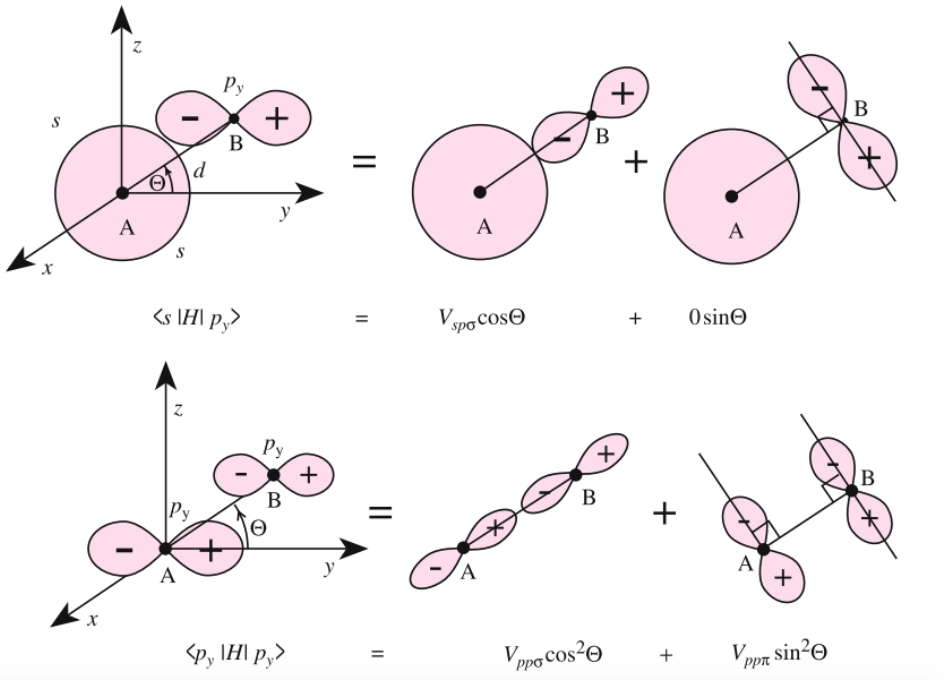

FIGURE 2.2: Interaction energies between orbitals on neighbouring atoms in a Slater-Koster, two-centre approximation with hopping (or Slater-Koster) parameters $V_{sp\sigma}$, $V_{pp\sigma}$ and $V_{pp\pi}$. Reproduced from [14].

two-center approximation. This decomposes the orbitals along the position vector connecting them, into combinations of appropriate bond types (e.g. $\sigma^{\pm}, \pi^{\pm}, \delta^{\pm}$ for d-orbitals), weighted by the angle between them and their separation distance. A simple illustration of this is found in Yu and Cardona [14] (fig. 2.2), with the full table up to d-orbitals published in Slater and Koster's 1954 paper [18]. With this simplification, tight binding models can be constructed and solved.

This method is computationally less expensive than more exact computational methods, and can be easily calculated at arbitrary $\boldsymbol{k}$-points off high-symmetry points, while getting the composition of the band, and the symmetry mostly correct. It can be fit to other methods reasonably easily by comparing quantities such as band energies and velocities close to high symmetry points. These models then provide an ideal testbed for determining the minimal ingredients necessary to produce the required results, highlighting for example the key interactions.

2.2 Spin-orbit interactions

Spin-orbit coupling has often historically been neglected from calculations of band structures since it enters as a relativistic correction to the Schrödinger equation. As described in the previous chapter, it is now being seen to play a key role in condensed matter with significant consequences for technological and fundamental physics. The majority of findings in this thesis are as a direct result of strong spin-orbit interactions, which are found to have rich and unexpected consequences. As a starting point, it will be helpful to consider how the spin-orbit interaction arises in atoms before exploring this in a lattice and looking into another manifestation of the spin-orbit interaction, the Rashba effect.

2.2.1 Atomic spin-orbit

So far we have discussed only non-relativistic physics but to include the spin-orbit interaction we need to consider a relativistic description of the electrons. These effects can be accounted for by introducing relativistic corrections to the Schrödinger equation, in order to approximate the Dirac equation, which treats these relativistic effects correctly. Taking account of these corrections, for a hydrogen-like atom with a spherical central potential, the Hamiltonian can be written [19]:

$$H = \Bigg(\underbrace{\frac{\boldsymbol{p}^2}{2m} + V}_{non\ rel.} - \underbrace{\frac{\boldsymbol{p}^4}{8m^3c^2}}_{mass\ corr.} - \underbrace{\frac{\hbar^2}{4m^2c^2}\frac{dV}{\partial r}\frac{\partial}{\partial r}}_{Darwin} + \underbrace{\frac{1}{2m^2c^2}\frac{1}{r}\frac{dV}{dr}\boldsymbol{L}\cdot\boldsymbol{S}}_{SOC} \Bigg) \tag{2.14}$$

where the first and second terms are simply the non relativistic part, the third term accounts for a variable mass. The fourth term is called the Darwin term, which applies only to $l = 0$ states. In the case of a Coulomb potential ($\sim \frac{1}{r}$), working out the matrix element by first order perturbation theory reduces this to an expression which depends solely on the amplitude of the radial part of the wavefunction evaluated at $r = 0$, where s-orbitals are the only orbitals to not have a node [16]. The final term is the spin-orbit

coupling (SOC) term, where there is a factor of a half included due to the Thomas correction.

The spin-orbit term is then be written as $H_{SOC} = \zeta \boldsymbol{L} \cdot \boldsymbol{S}$, where $\zeta = \frac{1}{2m^2c^2}\frac{1}{r}\frac{dV}{dr}$. This describes the spin-orbit coupling strength originating from a particular atomic species, which goes as $\zeta \sim Z^4$ (where Z is the atomic number): therefore, the spin-orbit coupling strength is generically larger for heavier elements [16]. This assumes a Coulomb potential $U(\boldsymbol{r}) = -Ze^2/\boldsymbol{r}$ however so in practice the spin-orbit strength is not simply monotonic with atom size. The spin-orbit term can anyway be straightforwardly incorporated into an effective Hamiltonian in the following way:

$$H = H_0 + H_{SOC} \tag{2.15}$$

$$H_{SOC} = \frac{\zeta}{2}\mathbf{L} \cdot \mathbf{S} = \frac{\zeta}{2}(L_x\sigma_x + L_y\sigma_y + L_z\sigma_z) \tag{2.16}$$

where $\sigma_{x,y,z}$ are the Pauli spin matrices, $\sigma_x = \left(\begin{smallmatrix} 0 & 1 \\ 1 & 0 \end{smallmatrix}\right)$, $\sigma_y = \left(\begin{smallmatrix} 0 & -i \\ i & 0 \end{smallmatrix}\right)$, $\sigma_z = \left(\begin{smallmatrix} 1 & 0 \\ 0 & -1 \end{smallmatrix}\right)$. The H_{SOC} term then becomes:

$$H_{SOC} = \frac{\zeta}{2}\begin{pmatrix} L_z & L_x - iL_y \\ L_x + iL_y & L_z \end{pmatrix} = \frac{\zeta}{2}\begin{pmatrix} L_z & L^- \\ L^+ & L_z \end{pmatrix} \tag{2.17}$$

where $L^{\pm} = L_x \pm iL_y$ and L_z are the orbital angular momentum ladder operators and z projection respectively. These operate in the following way:

$$L_z|Y_l^{\pm m}\rangle = \pm m_l|Y_l^{\pm m}\rangle \tag{2.18}$$

$$L^{\pm}|Y_l^{\pm m}\rangle = \sqrt{l(l+1) - m(m \pm 1)}|Y_l^{\pm m}\rangle. \tag{2.19}$$

where $|Y_l^{\pm m}\rangle$ is the orbital part of the wavefunction written in spherical harmonics. The angular momentum quantum number l has a range $0 \leq l \leq n$, and the magnetic quantum number m_l has a range $-l \leq m_l \leq l$. The introduction of spin-orbit coupling then doubles the effective Hamiltonian, since the spin-degeneracy is lifted, such that the original Hamiltonian in equation

2.15 can be written:

$$H = \begin{pmatrix} H_{\uparrow\uparrow} & H_{\uparrow\downarrow} \\ H_{\downarrow\uparrow} & H_{\downarrow\downarrow} \end{pmatrix} = \begin{pmatrix} H_0 + \frac{\zeta}{2}L_z & \frac{\zeta}{2}L^- \\ \frac{\zeta}{2}L^+ & H_0 - \frac{\zeta}{2}L_z \end{pmatrix} \tag{2.20}$$

where the Hamiltonian is split into quadrants for all combinations of spin-up and spin-down. Writing p-orbitals in spherical harmonics as (by way of example, since there are multiple consistent ways of writing these):

$$|p_x\rangle = -\frac{1}{\sqrt{2}}\left(|Y_1^1\rangle - |Y_1^{-1}\rangle\right) \tag{2.21}$$

$$|p_y\rangle = \frac{i}{\sqrt{2}}\left(|Y_1^1\rangle + |Y_1^{-1}\rangle\right) \tag{2.22}$$

$$|p_z\rangle = |Y_1^0\rangle. \tag{2.23}$$

it is then straightforward to calculate how spin-orbit coupling modifies the effective Hamiltonian using this prescription. With these definitions, the matrix elements in equation 2.20 then demonstrate how the spin-orbit interaction promotes a mixing of orbital character.

Until now this section has focused solely around bulk electronic structure and mentioned only a form of spin-orbit interaction derived in analogy to atomic physics. As briefly introduced in the previous chapter, in real crystals there are additional symmetry considerations that must be accounted for, as well as the surface itself having significant consequences for the electronic structure.

2.2.2 Surface states

It is worthwhile to study electronic states confined to surfaces because real crystals that we measure have a surface. States confined to the surface can have radically different properties to their bulk counterparts, introduced briefly in the previous chapter. This section will now briefly discuss key properties of surface states and provide a description of the well known Rashba effect, describing the effect of the spin-orbit interaction at crystal surfaces.

At the surface of a crystal, the perfect translational symmetry is broken (in the direction perpendicular to the surface), and the potential must then in some way go from the lattice potential to the vacuum potential. This means that now Bloch functions, which are valid solutions to the Schrödinger equation in the bulk, are no longer valid solutions exactly at the surface due to the broken symmetry. We can define the axis perpendicular to the surface as the z axis, labelling regions deep within the solid as $z \ll 0$ and the surface itself as $z = 0$.

Following Lüth [20], the solutions deep within the solid give the expected modified plane wave solutions but these must decay exponentially upon reaching the potential step into the vacuum at the surface, since they cannot exist outside the solid. The wavefunction has to be continuous at $z = 0$. Matching the plane wave onto an exponential decay is achieved by assuming the plane wave to be a superposition of the incoming Bloch function and a reflected Bloch function, i.e. having the form:

$$\psi_{\text{solid}} \sim Ae^{ik_z z} + Be^{-ik_z z}; z < 0 \tag{2.24}$$

$$\psi_{\text{vac}} \sim Ce^{-z}; z > 0. \tag{2.25}$$

The matching is achieved by forcing solutions, and their spatial derivative, evaluated at $z = 0$ to be equal:

$$\psi_{\text{solid}}|_{(z=0)} = \psi_{\text{vac}}|_{(z=0)} \tag{2.26}$$

$$\left.\frac{\partial \psi_{\text{solid}}}{\partial z}\right|_{(z=0)} = \left.\frac{\partial \psi_{\text{vac}}}{\partial z}\right|_{(z=0)}. \tag{2.27}$$

This demonstrates that solutions that exist deep within the bulk, for some real k that is a valid solution to the Schrödinger equation, extend fully up to the surface of the crystal (fig. 2.3a). This is then crucial for surface probes of bulk electronic structure, as will be discussed in the next chapter. It is worth noting that the peak in the real part of the wavefunction will never be exactly at $z = 0$, since the vacuum part of the wavefunction is an exponential decay. Its derivative therefore never goes to zero, meaning the condition in

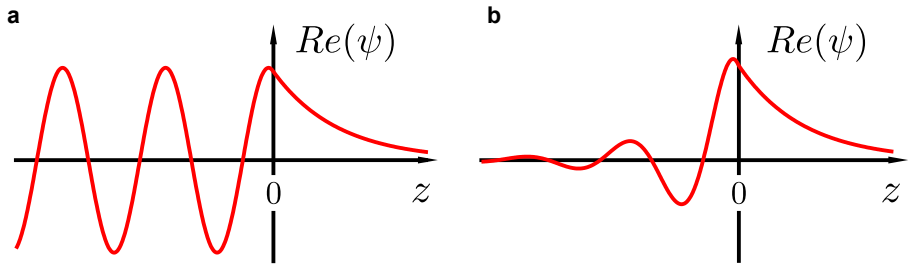

FIGURE 2.3: Real part of the bulk (a) and surface (b) wavefunctions near a crystal surface. Both can be seen to exponentially decay into the vacuum ($z > 0$), while only the surface state decays into the solid (since it cannot be degenerate with bulk solutions).

equation 2.27 would never be satisfied.

Additional states are also possible if we now allow for imaginary wave vectors for the wavefunction in the solid, which can still form valid solutions to the Schrödinger equation. This imaginary wave vector then produces an exponential decay into the bulk (from putting an imaginary wavevector into a plane wave like solution), as well as still being forced to decay into the vacuum. Having both exponential decays above and below $z = 0$ implies that the amplitude of the wavefunction goes to zero far from the surface both into the solid and the vacuum, i.e. these are localised to the surface (fig. 2.3b). It is clear then that the values of imaginary wave vector which give real values of energy (as required), correspond to energies which fall in the bulk band gap. Or equivalently, given that bulk states are solutions with real momenta, if these surface states existed at energies equal to bulk states, they could not have imaginary momenta and would not yield an exponential decay into bulk: the only place where imaginary momentum solutions can exist is where there is not already a real momentum solution, hence surface states must live in bulk band gaps.

This picture of how surface states can arise can be extended to 3D where surface states must still exist within a bulk band gap. Real crystals can have complicated band structures in 3D since bulk band energies E can disperse with in-plane momentum $\boldsymbol{k}_{||}$ and out-of-plane momentum $k_{\perp}$ (fig. 2.4a).

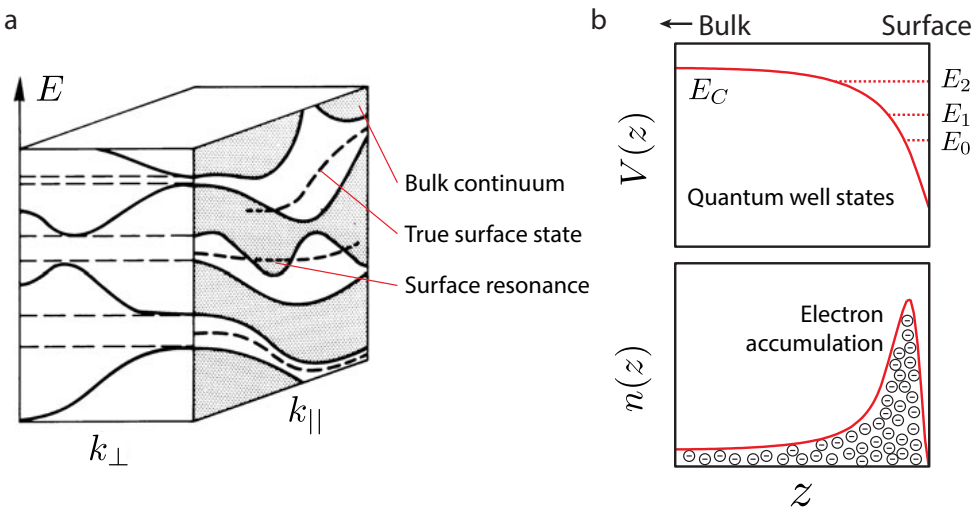

FIGURE 2.4: a) Schematic band structure with solid lines corresponding to bulk bands. The grey regions are the bulk continuum states and white corresponds to a band gap. The long dashed lines are true surface states living within a projected band gap, while the short dashed lines are degenerate with bulk states and so are described as surface resonances. b) Example band bending potential $V(z)$ for a conduction band edge E_C from an electron accumulation layer given by $n(z)$. This confines electron states into a ladder of subbands with energy E_i. a) Reproduced from [20]

Surface states can only have in-plane momentum $\boldsymbol{k}_{||}$ (dashed lines in figure 2.4a). True surface states still must exist in the projected bulk band gap, where the bulk band gap exists for all $k_\perp$. Some surface states can exist for $E(\boldsymbol{k}_{||})$ where a bulk state exists for a particular $k_\perp$, i.e. they are degenerate with the projected bulk continuum states. These are called surface resonances. They can mix with the bulk states and typically extend slightly deeper into the bulk than their true surface state counterparts.

Two main classifications of true surface states can be distinguished: Shockley surface states and Tamm states [21]. Shockley surface states typically arise from the boundary conditions being different at the surface and live in the band gap with a complex wave vector in the manner described above. The complex wavevector prevents them from being solutions in the bulk solid and they are hence localised to the surface. Tamm states can be thought of in a tight binding sense as arising from a change in the potential arising from the different atomic environment. This change in the potential amends the onsite term in the Hamiltonian and has the consequence that the bulk

states are 'split-off' from the states of the bulk solid. The fact that these only arise as a result of the different potential environment for the atoms at the surface lead to the surface localisation of these states.

Finally, as well as the potential barrier of the vacuum creating bound states in the bulk, if there is generically a change in the potential near to the surface or at an interface, there is the possibility of confining additional states (fig. 2.4b). This can happen in charge accumulation layers in semiconductors, where electronic charge is distributed in a way that screens the potential of the lattice near to the surface. A reduction from the bulk potential can stem for example from electron accumulation (if you have an n-type bulk), screening a positive ionic charge. An increase in the surface potential can arise from hole-accumulation (if you have a p-type bulk), screening negative ionic charge. An inversion layer is similar but where the surface and bulk carriers are opposite. This localised change in potential can confine states between these two potential barriers, acting as a quantum well-like potential (fig. 2.4b). The solutions are then a ladder of quantised states (fig. 2.4b). These confined states will retain information of the bulk Bloch character.

Breaking inversion symmetry at the surface of course has greater significance than the property of hosting surface states. In the previous chapter inversion symmetry breaking was stated as being a requisite for spin-splitting through the spin-orbit interaction. The following sections will go into more detail how this arises.

2.2.3 Time reversal and inversion symmetry

Until this section, the band structure in this chapter has been assumed to be spin-degenerate, i.e. there are two spins for every state $E(\boldsymbol{k})$. This is not an unreasonable assumption as this is a direct consequence of the dual constraints of time reversal symmetry and inversion symmetry, which can be shown in the following way.

The time reversal operator, $\hat{T}$, operates on a time dependent function

such that $\hat{T}f(t) = \pm f(-t)$. The time reversal operator acting on time reversal symmetric functions has an even (or positive) eigenvalue. Similarly, the parity (inversion) operator, $\hat{P}$, operates on a function such that $\hat{P}f(\boldsymbol{r}(x,y,z)) = \pm f(\boldsymbol{r}(-x,-y,-z)) = \pm f(-\boldsymbol{r})$. Inversion symmetric functions have an even parity eigenvalue. Provided these symmetries are not broken, then in energy and momentum space this means the following conditions must be satisfied for a state of $E(\boldsymbol{k})$:

$$\hat{T}E(\boldsymbol{k},\sigma) = E(-\boldsymbol{k},-\sigma) \implies E(\boldsymbol{k},\sigma) = E(-\boldsymbol{k},-\sigma) \tag{2.28}$$

$$\hat{P}E(\boldsymbol{k},\sigma) = E(-\boldsymbol{k},\sigma) \implies E(\boldsymbol{k},\sigma) = E(-\boldsymbol{k},\sigma) \tag{2.29}$$

$$\tag{2.30}$$

where $\sigma = \{\uparrow,\downarrow\}$. It is straightforward to see why momentum and spin have odd time reversal eigenvalues. Momentum has an odd parity eigenvalue as expected, while the spin has an even parity eigenvalue. This can be understood if you consider spin as having dimensions of angular momentum: a cross product of position and momentum. Both these quantities have odd parity eigenvalues, yielding a net even parity eigenvalue. The combination of these dual constraints implies a total double degeneracy of the Bloch states, termed Kramer's degeneracy.

2.2.4 The Rashba effect

The total spin degeneracy in the system can be lifted by breaking either of these symmetries. Magnetism breaks time reversal symmetry by shifting in energy the density of states of spin-up vs spin-down states depending on whether these are aligned or anti-aligned with an applied field in a Stoner-like model. With the energy of spin-up states being different to the energy of the spin-down states, it follows that this breaks time reversal symmetry (eq. 2.28), and bands acquire spin polarisation (fig. 2.5b). However, in the presence of broken inversion symmetry, even if time reversal symmetry is upheld, the degeneracy can be lifted by the Rashba effect.

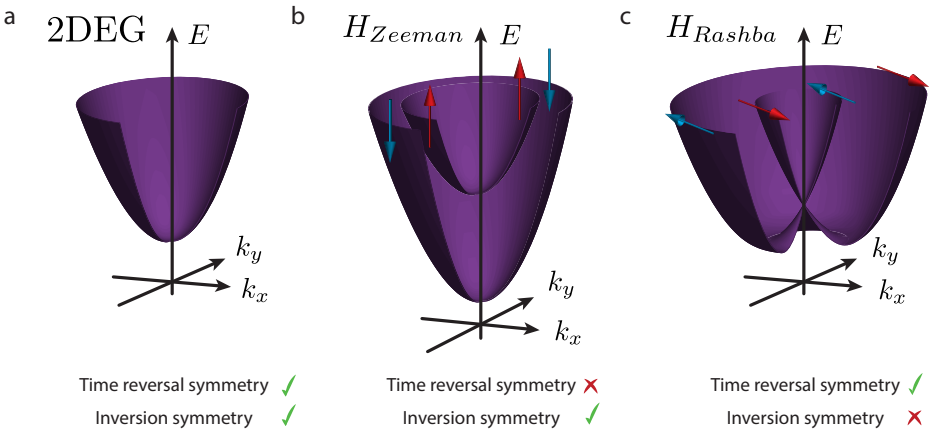

FIGURE 2.5: a) A typical two-dimensional electron gas (2DEG) dispersion in which $E \propto \boldsymbol{k}^2$. This has preserved time reversal symmetry and inversion symmetry. b) A 2DEG in an applied magnetic field (in the z direction) has broken time reversal symmetry but preserved inversion symmetry. c) A Rashba-split 2DEG (with spins in the k_x-k_y plane). Inversion symmetry is broken but time reversal symmetry is preserved.

The mechanism for how Rashba spin-splitting arises can be motivated by considering a two-dimensional electron gas (2DEG) at a material surface, formed from a gradient in the potential at the surface in the z direction (e.g. fig. 2.4b). In the case of a 2DEG, the asymmetric potential confining the electrons breaks inversion symmetry in the z direction (although, even without this asymmetric confining potential the interface between bulk crystal and vacuum, i.e. the surface, breaks inversion symmetry). Since $\boldsymbol{E} = -\frac{1}{e}\nabla \boldsymbol{V}(\boldsymbol{r})$, the gradient in the potential at the surface creates an electric field in the z direction. In a semi-classical picture, an electron moving through an electric field $\boldsymbol{E}$ with velocity $\boldsymbol{v}$ will experience this in its rest frame as an effective magnetic field $\boldsymbol{B} = -\frac{1}{c}\boldsymbol{v} \times \boldsymbol{E}$ [22]. This can couple to the spin states of the electrons through their intrinsic magnetic moment, lifting the spin-degeneracy. This naturally must have a dependence on the electron momentum through their velocity, the dependence is most easily shown from the spin-orbit Hamiltonian as a starting point.

The general form (not simply for a spherical potential) for the spin-orbit term in the Hamiltonian of equation 2.14 can be written as [23]:

$$H_{SOC} = \frac{\hbar}{4m^2c^2}\nabla \boldsymbol{V} \times \boldsymbol{p} \cdot \boldsymbol{\sigma}. \tag{2.31}$$

where m and $\boldsymbol{p}$ are the electron mass and momentum respectively, c is the speed of light, and $\boldsymbol{\sigma}$ are the Pauli matrices. Bychkov and Rashba in 1984 showed that for an electric field in the $\hat{\boldsymbol{z}}$ direction, $\boldsymbol{E} = E_z\hat{\boldsymbol{z}}$, from the potential change normal to the surface, the Hamiltonian becomes [2]:

$$H_R = \alpha_R \left(\hat{\boldsymbol{z}} \times \boldsymbol{p}\right) \cdot \boldsymbol{\sigma}. \tag{2.32}$$

where the constants and electric field strength are contained within the Rashba parameter, $\alpha_R = \frac{e\hbar^2}{4m^2c^2}E_z$. This can be expanded to give an equivalent form:

$$H_R = \alpha_R \left(k_x\sigma_y - k_y\sigma_x\right) \tag{2.33}$$

where k_i, and σ_i are components of the momentum and spin, respectively. From this we can understand that the spin-splitting is a function of momentum, and that an in-plane component of the momentum is locked to the perpendicular direction of the vectorial spin, termed spin-momentum locking. Solving the Schrödinger equation for a free particle with this additional term in the Hamiltonian, the following dispersion relation is found [2]:

$$E^{(\pm)}(\boldsymbol{k}) = \frac{\hbar^2\boldsymbol{k}^2}{2m} \pm \alpha_R\boldsymbol{k} \tag{2.34}$$

where $E^{(\pm)}$ refers to the two eigenstates given by:

$$\psi^+ = e^{i\boldsymbol{k}\boldsymbol{r}}(|\uparrow\rangle + ie^{i\theta_k}|\downarrow\rangle) \tag{2.35}$$

$$\psi^- = e^{i\boldsymbol{k}\boldsymbol{r}}(ie^{-i\theta_k}|\uparrow\rangle + |\downarrow\rangle) \tag{2.36}$$

which are superpositions of spin-up and spin-down eigenstates. This reflects the fact that with spin-orbit interactions, spin is no longer a 'good' quantum number. The phase factor includes an angle θ_k, that $\boldsymbol{k}$ makes with

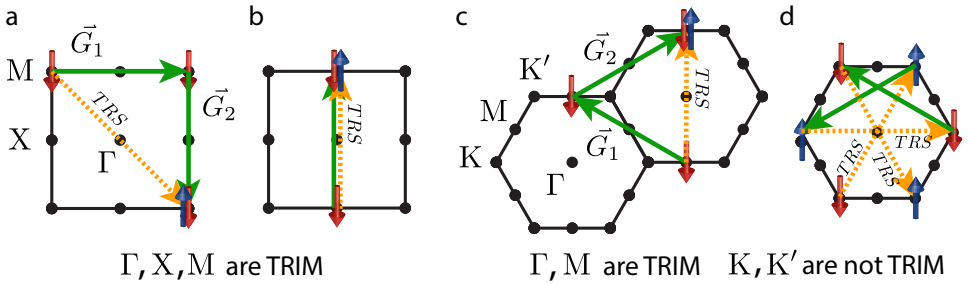

FIGURE 2.6: High symmetry points that can be translated between by both a reciprocal lattice vector and time reversal are necessarily doubly degenerate shown in these examples by following the arrows. a) The Γ, X and b) M points in the square Brillouin zone are all TRIM. c) The Γ and M points in a hexagonal Brillouin zone are TRIM. d) The K and K′ points are not TRIM. Green arrows denote reciprocal lattice vectors $\boldsymbol{G}$. The orange arrows denote the application of time reversal symmetry (eq. 2.28). High symmetry points are shown by black dots.

the x axis [24].

This derivation reveals several important aspects of Rashba spin splitting. The dispersion after Rashba splitting is then two free-electron like parabolae, with a splitting in energy that increases linearly in $\boldsymbol{k}$. They cross at exactly $\boldsymbol{k} = 0$ (the Γ point) since this is required by time reversal symmetry. This can be seen from inputting $\boldsymbol{k} = 0$ into the equation for time reversal symmetry (eq. 2.28).

This can be extended to a generic high symmetry point Λ at a momentum $\boldsymbol{k}_\Lambda$. Through application of time reversal symmetry (yellow arrows in fig. 2.6), we have $E(\boldsymbol{k}_\Lambda, \uparrow) = E(-\boldsymbol{k}_\Lambda, \downarrow)$. In addition, if the states at $\boldsymbol{k}_\Lambda$ and $-\boldsymbol{k}_\Lambda$ are separated in momentum by a reciprocal lattice vector $\boldsymbol{G}$ (green arrows in fig. 2.6), then $-\boldsymbol{k}_\Lambda + \boldsymbol{G} = \boldsymbol{k}_\Lambda$, which implies:

$$E(-\boldsymbol{k}_\Lambda + \boldsymbol{G}, \uparrow) = E(\boldsymbol{k}_\Lambda, \uparrow). \tag{2.37}$$

In this special case, with these two conditions (eq. 2.28 and eq. 2.37), the generic high symmetry point Λ must be doubly degenerate. This is shown by example in equation 2.38 and figure 2.6. A state can be translated by $\boldsymbol{G}$ onto a state with opposite momentum that is forced by time reversal to have

a state of opposite spin:

$$E(\boldsymbol{k}_\Lambda, \uparrow) = E(-\boldsymbol{k}_\Lambda, \downarrow) = E(-\boldsymbol{k}_\Lambda + \boldsymbol{G}, \downarrow) = E(\boldsymbol{k}_\Lambda, \downarrow) = E(\boldsymbol{k}_\Lambda, \uparrow) \tag{2.38}$$

This follows directly from Kramers theorem discussed earlier. These points at $\boldsymbol{k}_\Lambda = n\boldsymbol{G}/2$ are called time reversal invariant momenta (TRIM).

The second aspect that can be revealed from the Rashba Hamiltonian comes from considering the spin-polarisation. To first order, there is no σ_z component of spin (eq. 2.33), i.e. the spin is fully in the k_x-k_y plane. The model discussed is for a 2DEG and besides the broken inversion symmetry, the lattice symmetry itself has not be considered. Winkler gives a detailed description of the higher order effects of lattice symmetry in general on the spin-orbit Hamiltonian [23]. For now it will suffice to consider this 2DEG model.

Additionally, the spin and momentum components of the Rashba Hamiltonian (eq. 2.33) are perpendicular to each other, i.e. there is a perpendicular spin-momentum locking (e.g. fig. 2.5c). If this is evaluated around the k_x-k_y plane it can be shown that the spin circulates around the constant energy contours (fig. 2.5). Provided upheld TRS and broken inversion symmetry, this results in the well known counter-propagating chiral spin texture, shown in figure 2.5c.

This effect is well exemplified with its discovery by LaShell *et al.* (1996) on Au(111) [25], using angle-resolved photoemission spectroscopy (ARPES). At the surface of Au(111), there is a now well-known Shockley surface state living in the band gap, which is centred around the $\bar{\Gamma}$ point (fig. 2.7). LaShell and colleagues measured energy distribution curves (EDCs: the intensity vs energy at a single point in $\boldsymbol{k} = (k_x, k_y, k_z)$) for this state, at a series of different angles, corresponding to different in-plane momenta $\boldsymbol{k}$. In the EDC at $\boldsymbol{k}_{||} = 0$, they observe two peaks, whereas when they measure at momenta $\boldsymbol{k}_{||} \neq 0$, they measure that these peaks split in energy giving four peaks (fig. 2.7a). The peaks at higher binding energy are an artefact of the light source they use, which is an ArI doublet. The splitting of the peaks in the

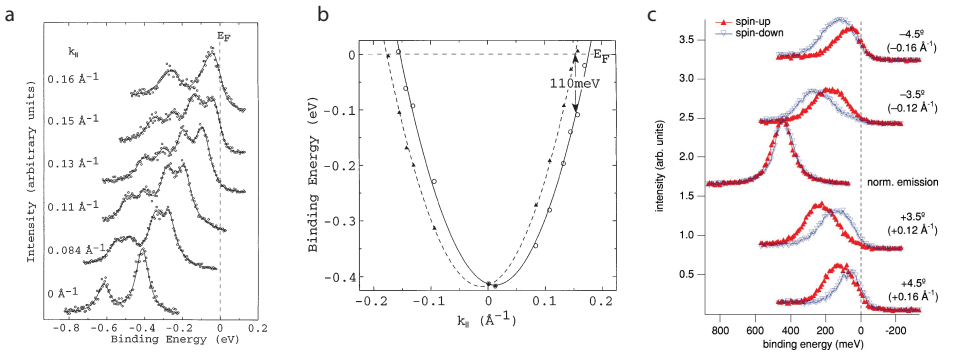

FIGURE 2.7: First measurements of the Au(111) surface state using ARPES [25] and spin-ARPES [26]. a,b) Two NFE-like parabolic bands ascribed to spin-splitting. c) Spin-resolved energy distribution curves as a function emission angle showing opposite spin-polarisation of the these bands consistent with a Rashba component of the spin.

EDCs away from the $\bar{\Gamma}$ point in momentum they attribute to the spin-orbit interaction. The fits to the peak positions gives two nearly free electron-like parabolae that are shifted in momentum, so this looks qualitatively like a Rashba splitting. However the size of the splitting that would arise from the surface potential step in the original Rashba model would typically give splittings in energy at the Fermi level of $\Delta E = 10^{-3}$ meV. They measure a splitting of $\Delta E = 110$ meV, orders of magnitude larger, so it cannot be from the electrostatic surface potential alone. They recognise that the proximity of the wavefunction to the asymmetric potential of the ion cores is important. The splitting is then additionally dependent on the atomic spin-orbit strength from the gradient in the potential near the nuclei.

This is confirmed by a tight binding model by Petersen and Hedergård (2000) [24]. They represent the asymmetry of the surface potential through allowing mixing of p_z and $p_{x,y}$ orbitals. They include intra-atomic spin-orbit coupling as described in equation 2.20 and show that without including the $p_{x,y}$ orbitals, there is no effect from spin-orbit coupling. This coupling to the $p_{x,y}$ orbitals near the surface makes the wavefunction asymmetric and inherits the full atomic spin-orbit strength. In chapter 4 we will expand on the significance of this. From this procedure, they gain more quantitative

agreement with measurements, in addition to what can be qualitatively understood from a typical Rashba model. The size of the splitting in Rashba split surface states has been an active area of research in recent years which will be discussed in a later chapter in this thesis.

Further, this Au(111) surface state was found to have a spin texture characteristic of Rashba splitting by Hoesch *et al.* (2004), as measured by spin- and angle-resolved photoemission (spin-ARPES) [26]. Measuring a similar set of characteristic EDCs as with LaShell (1996), they were able to measure directly the components of spin at different in-plane momenta and show that this had a perpendicular spin-momentum locking characteristic of the in-plane chiral spin texture arising from Rashba spin-splitting (fig. 2.7c). These techniques ARPES and spin-ARPES are clearly invaluable for probing the electronic structure of a material. These are additionally the techniques that are employed heavily throughout this thesis. In order to interpret our results it is therefore essential to have an introduction into how these techniques work and how they can be implemented.

Chapter 3

Methods

3.1 Angle-resolved photoemission spectroscopy

Angle-resolved photoemission spectroscopy (ARPES) and spin-ARPES are techniques that have been employed throughout this thesis. This chapter will walk though the key theory which allows interpretation of photoemission data, and consider typical practical set-ups of a photoemission experiment. The theoretical section will follow mainly Hüfner [21] and Damascelli (2004) [27].

3.1.1 Photoemission background

The technique relied on heavily for this thesis is angle-resolved photoemission spectroscopy (ARPES), which can be thought of as imaging directly the occupied part of the electronic band structure plus interactions. It has its roots in the photoelectric effect, discovered by Hertz in 1887 [28] and later described by Einstein in 1905 [29], for which he won his Nobel Prize. This is where light is incident on a sample, which excites an electron within the solid. Provided the photoexcited electron has enough energy to overcome the potential barrier of the surface, the photoelectron can escape the sample. Information about the binding energy and momentum of the electrons within the solid can be obtained from measuring the kinetic energy and emission angle of the outgoing photoelectrons, effectively building up a picture of the band structure of a material. The details of this process are quite involved and some simplifying assumptions will have to be made in order to understand the results.

There are two main frameworks for describing photoemission: the three-step model and the one-step model (fig. 3.1). The three-step model gives a qualitatively simpler picture to interpret, which still provides reasonable results, while the one-step model provides the basis of cutting edge photoemission calculations. The three-step model breaks the photoemission process into separate processes summarised as:

1. optical excitation of an electron into a bulk final state
2. propagation within the bulk state to the surface
3. refraction at the surface and escape into the vacuum

The one-step model treats photoexcitation and emission of an electron as a single process in which the photoelectron is excited directly into a damped inverse LEED (low-energy electron diffraction) state near the surface, which is wave matched onto a wavefunction outside the crystal (fig. 3.1). The details of this treatment are beyond the scope of this thesis but an introduction can be found in Hüfner [21]. Instead, interpreting photoemission experiments from within the framework of the three-step model will be discussed in some detail.

3.1.2 Three-Step model

For the first step within the three step model, the transition rate from an initial state Ψ_i into a final state wavefunction Ψ_f can be described by Fermi's golden rule [27]:

$$w_{fi} = \frac{2\pi}{\hbar}|\langle\Psi_f^N|H_{int}|\Psi_i^N\rangle|^2\delta(E_f^N - E_i^N - h\upsilon) \tag{3.1}$$

where E_i^N and E_f^N are the initial and final state energy of the N-particle system respectively, which must be conserved upon excitation with a photon of energy $h\upsilon$. The N-particle system consists of the $(N-1)$-particle system left behind after the emission of a particle with kinetic energy E_{kin} i.e. $(E_f^N = E_f^{N-1} + E_{kin})$. Similarly, the initial system energy can be separated

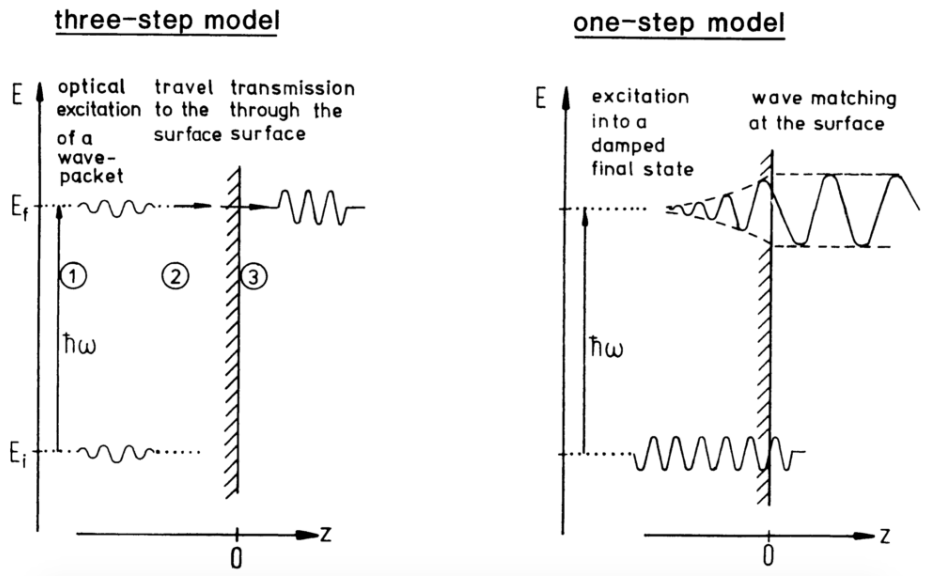

FIGURE 3.1: Schematic of the three-step model vs the one-step model. The three-step model involves 1) optical excitation, 2) travel to the surface in a bulk state 3) escape into the vacuum. The one-step model excites directly into a damped final state near the surface, which is wave matched onto a state in the vacuum. Reproduced from [21].

into the $(N-1)$-particle energy and the binding energy of an electron, E_B i.e. ($E_i^N = E_i^{N-1} - E_B$).

The electromagnetic field of the light implies that in the Hamiltonian $\boldsymbol{p} \rightarrow \boldsymbol{p} - e\boldsymbol{A}$, where $\boldsymbol{p} = i\hbar\boldsymbol{\nabla}$ is the momentum operator, and $\boldsymbol{A}$ is the electromagnetic vector potential. Therefore, the kinetic energy part of the interaction Hamiltonian becomes (neglecting the higher order $\boldsymbol{A} \cdot \boldsymbol{A}$ term):

$$H_{int} = \frac{e}{2mc}(\boldsymbol{p} \cdot \boldsymbol{A} + \boldsymbol{A} \cdot \boldsymbol{p}). \tag{3.2}$$

The commutation relation $[\boldsymbol{p}, \boldsymbol{A}] = -i\hbar(\boldsymbol{\nabla} \cdot \boldsymbol{A})$ implies then:

$$\boldsymbol{p} \cdot \boldsymbol{A} + \boldsymbol{A} \cdot \boldsymbol{p} = 2\boldsymbol{A} \cdot \boldsymbol{p} - i\hbar(\boldsymbol{\nabla} \cdot \boldsymbol{A}). \tag{3.3}$$

The dipole approximation is then invoked, since the wavelength of light is much greater than the inter-atomic distances so $\boldsymbol{A}$ is assumed to be constant

(and so the divergence of $\boldsymbol{A}$ is assumed to be zero). The interaction hamiltonian with the photon is then [21]:

$$H_{int} = \frac{e}{mc}\boldsymbol{A}\cdot\boldsymbol{p}. \tag{3.4}$$

which is the form that is typically considered in the photoemission process. It is also important to point out that vertical transitions (no in-plane momentum transfer) from an initial to final state are not possible for a free electron. Therefore the lattice potential is a strict requirement: the crystal momentum is essential for excitation into a final state in equation 3.1.

Factoring out the single electron orbital, the many-particle wavefunctions in the matrix element in equation 3.1 can be written (in the Hartree-Fock approximation) as an antisymmetric product of the photoelectron and the $(N-1)$-electron system:

$$\Psi_i^N = \mathcal{A}\phi_i^k\Psi_i^{N-1} \tag{3.5}$$

where $\mathcal{A}$ is the antisymmetry operator, and ϕ_i^k is the initial state one-electron orbital from which the electron is excited (at some k). Assuming the sudden approximation (i.e. the instantaneous creation of a photohole, with no time for the system to relax), the final N-electron ground state of the whole system can be written similarly as:

$$\Psi_f^N = \mathcal{A}\phi_f^k\Psi_f^{N-1} \tag{3.6}$$

The transition matrix element from Fermi's Golden Rule (eq. 3.1) can then be factored into:

$$\langle\Psi_f^N|H_{int}|\Psi_i^N\rangle = \langle\phi_f^k|\boldsymbol{A}\cdot\boldsymbol{p}|\phi_i^k\rangle\,\langle\Psi_s^{N-1}|\Psi_i^{N-1}\rangle \tag{3.7}$$

where the first term is the one-electron transition matrix element $M_{f,i}$. The second term $c_s = \langle\Psi_s^{N-1}|\Psi_i^{N-1}\rangle$ gives the amplitude that, after an electron is removed from the initial state $|\phi_i^k\rangle$ of the N-electron ground state, the

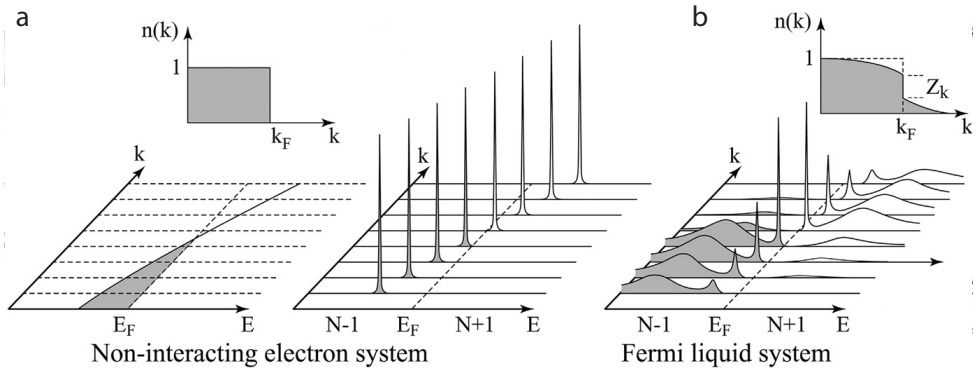

FIGURE 3.2: a) Non-interacting system with the spectrum for a band dispersing across the Fermi level. b) The same band in an interacting system with satellites corresponding to additional final states. Ground state occupation function $n(k)$ shown at zero temperature for both non-interacting (a) and interacting systems (b). Reproduced from [27].

$(N-1)$-electron system is left in a final state s. The photoemission intensity at a momentum $\boldsymbol{k}$ and energy E_{kin} is then proportional to a sum over all possible final states:

$$I(\boldsymbol{k}, E_{kin}) \sim \sum_{f,i} |M_{f,i}|^2 \sum_s |c_s|^2 \, \delta(E_{kin} + E_s^{N-1} - E_i^N - h\nu) \tag{3.8}$$

where the delta function conserves total energy. The second sum is called the spectral function $A(\boldsymbol{k}, E) = \sum_s |c_s|^2$, which contains all the information about many-body effects and interactions within the photoexcitation process in this first step.

In the non-interacting case (fig. 3.2a), there is a peak in the photoemission spectrum for a transition into a final state with a non-zero overlap between Ψ_f^{N-1} and Ψ_i^{N-1}. In the case of a weakly interacting system, the spectral function looks similar to the non-interacting case. A more strongly interacting system will have multiple final states for which there is some overlap with the same initial state. This reflects the fact that removing an electron from a system in which the interactions between electrons is strong, will result in a greater change to the local potential of the system, and correspondingly the main photoemission peak will also have satellite peaks for these additional final states [27]. How the spectral function affects the photoemission spectrum in the presence of interactions is discussed in the following

way.

Since the spectral function is dealing with the response of the system to the photoexcitation process, it is convenient to relate this to the one-electron Green's function $G(\boldsymbol{k}, E)$. The relation between the spectral function and the one-electron Green's function is given by:

$$A(\boldsymbol{k}, E) = \frac{1}{\pi}|ImG(\boldsymbol{k}, E)| \tag{3.9}$$

For a non-interacting system, the necessary Green's function is written as [21]:

$$G^0(\boldsymbol{k}, E) = \frac{1}{E - E^0(\boldsymbol{k}) - i\delta} \tag{3.10}$$

where δ is an infinitesimally small number and $E^0(\boldsymbol{k}) = \hbar^2\boldsymbol{k}^2/(2m)$ is the energy of a free electron. Therefore the spectral function in the absence of interactions, corresponds to a delta function at an energy defined by the Hartree-Fock orbital energy, or Koopmans' binding energy (e.g. fig. 3.2a).

For an interacting system (in reality this is what is measured), the change in energy and lifetime through interactions is included in the Green's function as a complex self-energy, $\Sigma(\boldsymbol{k}, E) = Re\Sigma + iIm\Sigma$, giving:

$$G(\boldsymbol{k}, E) = \frac{1}{E - E^0(\boldsymbol{k}) - \Sigma(\boldsymbol{k}, E)} \tag{3.11}$$

therefore yielding the spectral function:

$$A(\boldsymbol{k}, E) = \frac{1}{\pi}\frac{Im\Sigma}{(E - E^0(\boldsymbol{k}) - Re\Sigma)^2 + (Im\Sigma)^2)}. \tag{3.12}$$

In the presence of interactions that result in a self energy contribution (e.g. electron-electron, electron-impurity, electron-boson), a quasi-particle picture is appropriate, describing the particles as being dressed by these interactions. The energy of the quasiparticles is renormalised from the bare electron energy, and there is additional broadening from their finite lifetime away from the Fermi energy. In a weak limit of interactions such that there is little incoherent spectral weight expected, from equation 3.12 it is clear that the spectral function contribution to the photoemission intensity will be

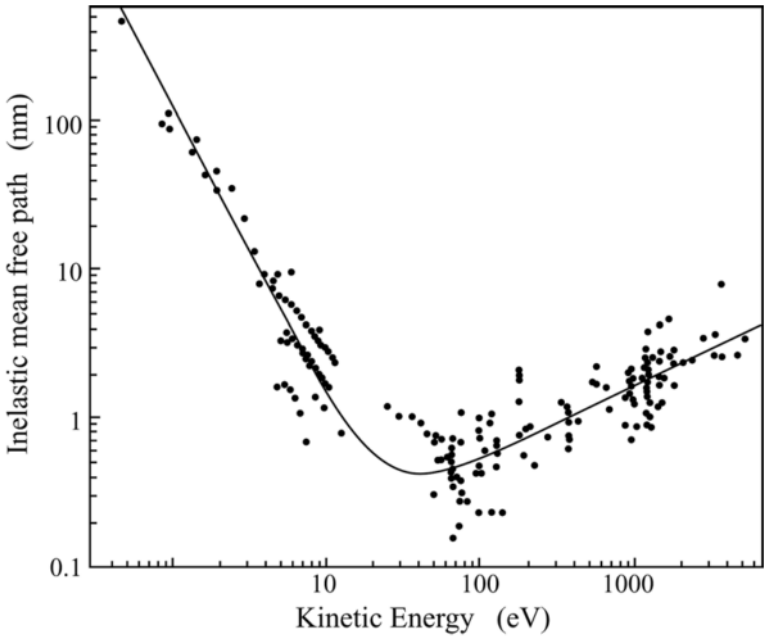

FIGURE 3.3: Universal curve for the inelastic mean free path (IMFP) of electrons in various solids. The IMFP is shown to depend solely on the kinetic energy of the electrons. Reproduced from [30].

Lorentzian. The width and position are then determined by the free-electron energy, and the complex self energy. To include that ARPES experiments probe only occupied states, the spectral function must also be multiplied with the Fermi function:

$$f(E) = \frac{1}{e^{(E-\mu)/k_b T} + 1} \tag{3.13}$$

where μ is the chemical potential of the system, k_B is the Boltzmann constant, and T is the system temperature. Both the Fermi function and spectral function must then additionally be convolved with a Gaussian to model the resolution of the experimental set-up including the detector.

In the second step within the three step model, after excitation into the bulk Bloch final state, the electron propagates to the surface of the crystal. Electrons can lose energy through inelastic scattering processes, which provides a background in the spectra that can be subtracted. The probability of an electron escaping the sample reduces exponentially into the solid at a

length scale of the inelastic mean free path, λ. This can be given by a Beer-Lambert law for photoemission as [30]:

$$I_d = I_0 e^{(-d/\lambda)} \tag{3.14}$$

where I_d is the intensity of electrons from an escape depth d, and I_0 is the intensity corresponding to electrons escaping from the sample surface. For a longer inelastic mean free path, there is a greater probability of electrons reaching the surface and so the sampling depth is greater. The mean free path of the electrons depends on their kinetic energy and follows the well-known 'Universal curve' (fig. 3.3). At low energies (below the minimum in the curve), the IMFP goes as E^2. This can be understood as greater energy allows for scattering from filled states at deeper binding energies and scattering into higher energy unfilled states. Therefore the scattering probability will increase, since increasing the kinetic energy of the electrons makes more states available for scattering (meaning the IMFP will shorten). This is the case at low energies where there is a higher density of states from the valence electrons. Once the kinetic energy surpasses the binding energy of the valence electrons, there is a greater energy separation between states. For energies above the IMFP curve minimum, this can be understood simply as a greater kinetic energy electron can travel further without scattering. The curve minimum is in the vacuum ultra violet (VUV) region of photon energies at $h\nu \sim 30$ eV, which yields a mean free path of $\lambda \sim 5$ Å. This is what makes photoemission such a surface sensitive technique. The universal curve is intended as an approximate guide for giving mean free paths in the correct range or order of magnitude (which is sufficient for the purposes of this thesis). It is clear from the figure (fig. 3.3) that there is a large degree of variation dependent on several material specific parameters (making it not so universal after all). A more sophisticated method for approximating the mean free path as a function of kinetic energy for specific electrons in specific materials (including e.g. free electron plasma energy, atomic valency, atomic density) can be found in Hüfner [21], referring to the TPP-2

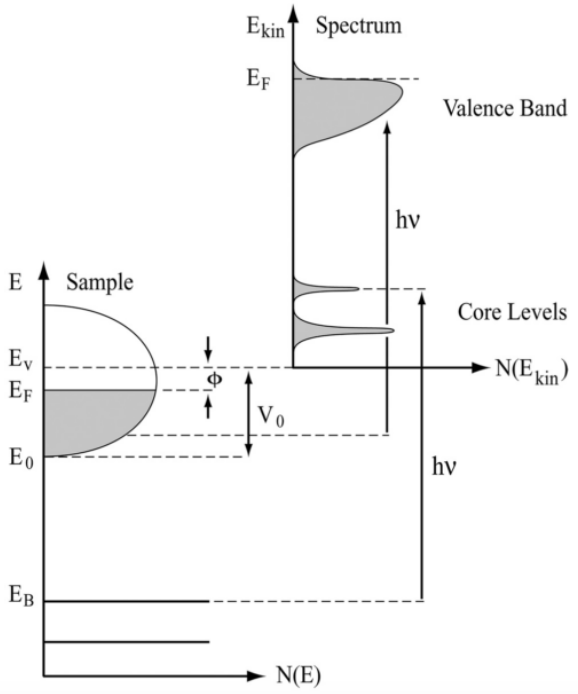

FIGURE 3.4: Energies involved in the photoemission process. The density of states produced (right) when initial states within a sample (left) are excited by a photon with enough energy. Reproduced from [21].

method.

In the third step, the electron is refracted at the surface and escapes into the vacuum provided it is excited with enough energy. In a hemispherical analyser (exclusively used in the photoemission measurements underpinning this thesis), the kinetic energy and surface emission angle are the quantities measured which should be converted into binding energy and momentum. In an intuitive description, the emission angles can be determined by use of electrostatic lenses to guide the path of the electrons into the analyser, after which the kinetic energy can be determined by the path of the electrons through the oppositely charged hemispheres of the analyser (fig. 3.5). The practicalities will be described further in a later section.

Conservation of energy dictates that the binding energy within the solid is given by:

$$E_B = h\nu - \Phi_A - E_K \tag{3.15}$$

where E_K is the measured kinetic energy, and Φ_A is the work function of the

analyser (fig. 3.4). The kinetic energy measured with respect to the vacuum level in the analyser is the important quantity here since the analyser and sample have the same ground [31]. From this equation the binding energy of the electron within the solid can be determined.

The momentum of the initial state within the solid can be determined through momentum conservation at the surface using its measured emission angle and kinetic energy. The momentum of the photon is typically not considered at the energies used in VUV-ARPES experiments (where for example at $h\nu = 20$ eV $\sim p = 0.01$ $\hbar$Å^{-1}, somewhat smaller even than typical linewidths of sharp features). The matching conditions for the wavefunction at the surface, combined with the upheld x-y translational symmetry requires that the in-plane momentum is conserved, giving:

$$\boldsymbol{k}_{||} = \frac{1}{\hbar}\sqrt{2mE_K}\sin\theta \tag{3.16}$$

where θ is the emission angle of the electron relative to the sample surface (fig. 3.5). Note that there is no reciprocal lattice vector term so this momentum is defined in the extended zone scheme, allowing ARPES measurements to probe neighbouring Brillouin zones outside the first zone, by probing photoelectrons with increasing emission angles. It is worth noting again that the lack of momentum imparted by the photon means electronic transitions can be considered as vertical so this has to be considered in a reduced zone scheme (or equivalently, that the crystal imparts the required momentum, as mentioned previously [27]).

This defines the in-plane momentum well, however the out-of-plane momentum $k_\perp$ or k_z is not a good quantum number due to the lack of translational symmetry in this direction. Additional considerations are required. A widely used model which gives reasonable results is the free-electron final state model, in which $k_\perp$ can be determined by assuming the bulk Bloch final states to be nearly-free-electron-like, giving:

$$E_f(\boldsymbol{k}) = \frac{\hbar^2(\boldsymbol{k}_{||}^2 + k_\perp^2)}{2m} - |E_0| \tag{3.17}$$

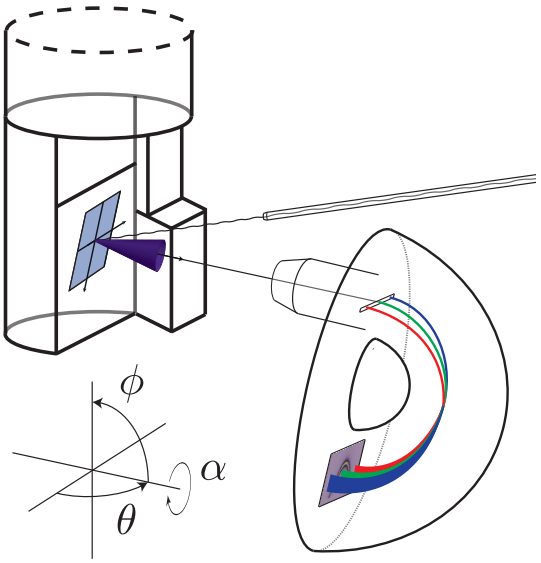

FIGURE 3.5: A schematic of a typical ARPES experiment. Light is incident on a sample emitting photoelectrons at various angles and energies. The photoelectron emission angle is accounted for in the transfer lens section and its path through the analyser, with the energy being determined in the hemisphere. A 2D spectrum can be recorded using a multichannel plate, a phosphor screen and a camera.

where E_0 is the binding energy of the bottom of the valence bands [21]. This then gives a form of the perpendicular momentum as:

$$k_z = \frac{1}{\hbar}\sqrt{2m(E_K \cos^2\theta + V_0)} \tag{3.18}$$

where $V_0 = |E_0| + \Phi_A$ is termed the inner potential. This can be understood as the bottom of the valence bands referenced to the vacuum level, and in practice is effectively a fitting parameter.

It is clear from this equation that k_z depends on the photon energy through the kinetic energy, leading to a standard method for determining the out-of-plane dispersion by varying systematically the photon energy. Until V_0 is determined, the absolute value of k_z will be somewhat arbitrary. The inner potential can be obtained in practice through attempting to match the periodicity of spectral features in dispersions along k_z to the known Brillouin zone spacing in this direction and varying V_0 in the processed data until there is good agreement. A more accurate method would additionally use

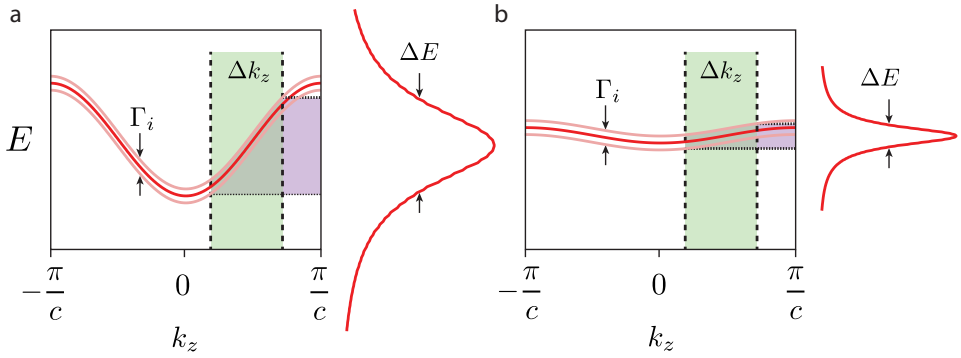

FIGURE 3.6: Example of k_z broadening for 2D and 3D states. Taking an example of $h\nu = 30$ eV, this gives $\lambda = 5$ Å giving $\Delta k_z = 0.2$ Å^{-1}. For an example $c = 10$ Å, this gives a Brillouin zone size of approximately $k_z = \pm 0.314$ Å^{-1}, so Δk_z is approximately the size of the green shaded region. a) A 3D state dispersing strongly in $E(k_z)$, with lifetime broadening Γ_i. Finite k_z integration of Δk_z, results in a large energy broadening ΔE dominated by k_z broadening. b) A quasi-2D state with little k_z dispersion (and the same Γ_i as in (a)). The resulting broadening ΔE is more lifetime dominated.

band structure calculations and V_0 varied until these agree well.

The free-electron final state model works well where the initial states are nearly-free-electron-like. It additionally works well at higher energies, where the crystal potential becomes less significant, and the final states become so close in energy that they form a continuum [27]. The free-electron final state model can even generally give reasonable results at lower photon energies.

However, at lower photon energies, k_z poses other experimental issues. Due to the finite mean free path of the electrons, the final state is damped into the solid over a distance λ. This leads to a finite probing depth. The finite probing depth along the z axis, where translational symmetry is broken, results in a finite width in momentum space, $\Delta k_z = \lambda^{-1}$. This finite width in k_z is then large for small sampling depths, given by short λ. The integration width in k_z can be narrowed by probing more of the Bloch functions in the z direction. This is never zero however from the finite probing depth, so there will always be an intrinsic width in k_z which becomes important for states which disperse strongly in the k_z direction (fig. 3.6).

For states that disperse greatly in k_z (3D states), a large Δk_z results in a large energy broadening ΔE, which usually dominates the total energy

broadening (fig. 3.6a). This is termed k_z broadening. Conversely, for states which do not disperse greatly in k_z (e.g. surface states, quasi-2D states), k_z broadening is equivalently smaller, meaning the total energy broadening will likely be more dominated by other effects such as intrinsic lifetime broadening (fig. 3.6b). At lower photon energies, with small mean free paths, k_z broadening is large, so 3D states appear within a measured spectrum as diffuse spectral weight. Conversely, if a spectral feature appears sharp, its electronic dimensionality is likely more quasi-2D.

3.1.3 Matrix elements and symmetry

An important contribution to the photoemission intensity (eq. 3.7 and eq. 3.8) is the one-electron transition matrix element $M_{f,i}$. After factoring out the $(N-1)$-electron system, the matrix element term has three parts: the one-electron final state wavefunction; the interaction Hamiltonian, which for photoemission is the dipole operator; and the one-electron wavefunction of the initial state, overall giving:

$$M_{f,i} = \langle \phi_f^k | \boldsymbol{A} \cdot \boldsymbol{p} | \phi_i^k \rangle \tag{3.19}$$

Since this term is an integral of the two wavefunctions over all space, if the integrand is an odd function (or has an odd parity eigenvalue given the definition in the previous chapter), the integral will be zero. The matrix element will therefore vanish, and hence too the photoemission intensity. This provides a powerful tool for selectively probing given initial states by measuring in a geometry which necessarily greatly reduces the intensity from initial states with a vanishing matrix element.

To illustrate this, consider the following highly idealised example (depicted in fig. 3.7). Consider photoemission from p-orbitals by linearly polarised light. The propagation vector and polarisation vector of the light are governed by the $\boldsymbol{A} \cdot \boldsymbol{p}$ term. In the geometry in this idealised example (fig. 3.7), light is incident exactly along the x-z direction, which is along the mirror plane. The polarisation vector for s-polarised light is defined as having

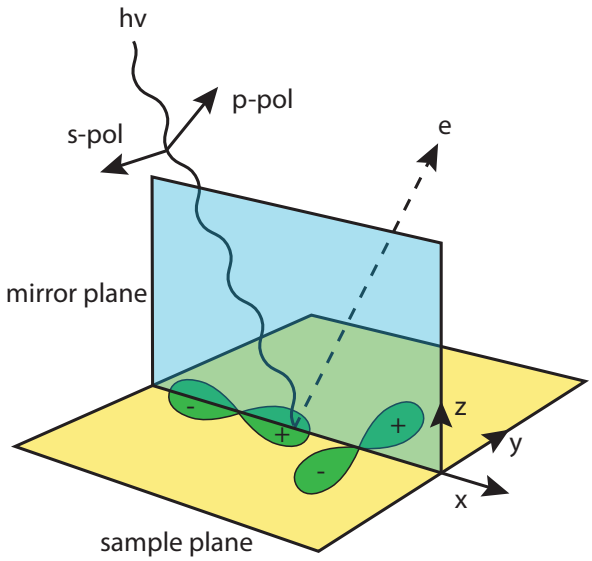

FIGURE 3.7: Simplified geometry of light polarisation and initial state orbitals to explain matrix element effects. Depending on the parity of the light polarisation and initial state orbital under reflection through the scattering plane (the mirror plane shown in the figure), the matrix element may integrate to zero.

its polarisation vector parallel to the samples surface, whereas p-polarised light is defined as having a polarisation vector perpendicular to the sample surface. An important mirror plane, the scattering plane, is defined such that p-polarised light is even under parity transformation with respect to it, and s-polarised light has an odd-parity eigenvalue.

The final state is assumed to be that of a free-electron, as previously discussed. We can further simplify this example by considering photoelectrons travelling along the mirror plane direction to an analyser which is itself in the mirror plane. Final states which have an odd parity eigenvalue will have a node in their wavefunction at zero and so the amplitude of the wavefunction at the detector will also be zero. This means that the final states must be even parity. In real experiments however this idealised situation is never practically realised but through our work on BiTeI, it will become clear that this assumption about the final state is still practically useful in many cases. The parity of the matrix element as a whole must be even since an odd integrand would integrate to exactly zero. Given the approximation of an

even parity final state, this imposes that the parity of the dipole operator (governed by the light polarisation vector) and the initial states must be the same (both even (+), or both odd (-), under parity inversion through the mirror plane) summarised as:

$$\langle \phi_f^k | \boldsymbol{A} \cdot \boldsymbol{p} | \phi_i^k \rangle = \begin{cases} \langle + | + | + \rangle \neq 0 & \text{for} \quad \mathrm{p-pol} \\ \langle + | - | - \rangle \neq 0 & \text{for} \quad \mathrm{s-pol} \end{cases}$$

where all other combinations integrate to zero. From this, p-polarised light will excite from even parity initial state orbitals, whereas s-polarised light will excite from odd parity initial state orbitals, with a non-vanishing one-electron transition matrix element.

Considering the p-orbitals (fig. 3.7), p_x and p_z orbitals are mirror symmetric in the mirror plane, lying along the x and z axes. These therefore have even parity eigenvalues and are excited in this situation solely by p-polarised light. On the other hand, p_y orbitals have a contribution from the phase of the wavefunction which is positive on one side of the mirror plane, and negative on the other. Taking this into account, p_y orbitals have odd parity eigenvalue and so are excited solely by s-polarised light, in this example.

However in reality, beyond the so far idealised example considered, these strict conditions are more relaxed. For example the propagation vector of the light is at an angle to the mirror plane, which means the light polarisation vector may not be purely p-polarised or purely s-polarised. This means the one-electron transition matrix element and therefore the photoemission intensity will not be strictly vanishing. Light which is p- or s-polarised will therefore only predominantly excite from the symmetry expected initial state orbitals, with a non-vanishing matrix element for the other orbitals. This condition can also be relaxed by the analyser being at an angle to the mirror plane / sample surface and the final state therefore no-longer being

strictly required to be even parity. Additionally, real orbitals could be modified from the hydrogen-like simplified cases through bonding / hybridisation, which then makes the symmetry argument harder to make. In all these cases, instead of leading to a strictly vanishing matrix element, it will instead lead to a quantifiable reduction in the photoemission intensity. Despite these convoluting factors, this still provides a means to study the initial state orbital composition through polarisation-dependent photoemission.

3.2 Spin-ARPES

As well as using light polarisation to selectively probe the initial state orbital composition, there are techniques available which allow probing not just of the initial state orbital but also the spin-degree of freedom. Spin measurement and control is of high interest in an age where the effect of spin-orbit interactions are being revisited and potential electronic devices taking advantage of the spin-degree of freedom are being conceived and even laboratory tested [32].

In a spin-ARPES experiment, after taking their path through the transfer lens section and analyser, a beam of electrons of known emission angle and energy are guided through a hole at the base of the analyser (fig. 3.8). The dimensions of the hole and the measurement settings used for the analyser then determine the angular and kinetic energy resolution. At this point, there are two main techniques for asymmetrically scattering spin-up and spin-down electrons to obtain spin-resolution: Mott scattering and very low-electron energy diffraction (V-LEED). The majority of the spin-ARPES results presented in this thesis were measured at the i3 beamline of the MAX III synchrotron in Sweden [33], with a Mott scattering set up. Additional measurements were performed at the APE beamline of the Elettra synchrotron, in Italy [34], with a V-LEED set up.

At i3 (Mott detector), the electrons are accelerated to 25 keV in the spin transfer lens section, and scattered off a thorium foil target. The high kinetic energies of the electrons mean relativistic effects are more significant

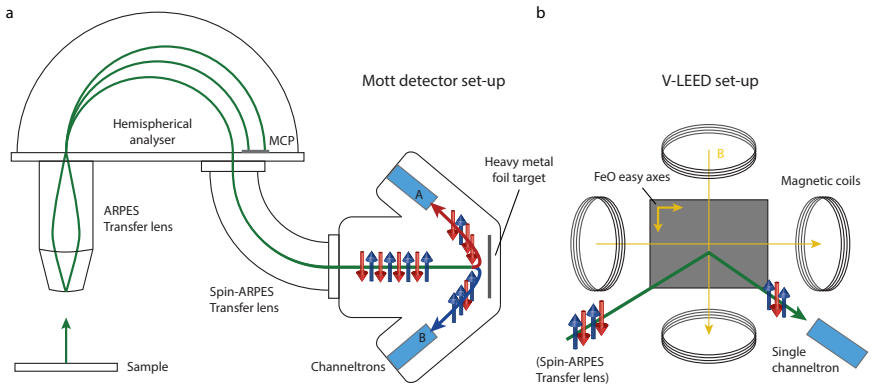

FIGURE 3.8: A schematic of typical spin-ARPES set-ups. a) Mott scattering set-up: experiment is identical to ARPES up to the MCP, where a selection of photoelectrons with known emission angle and kinetic energy are taken into the spin transfer lens. The incoming beam is scattered of a heavy metal target and the counts on symmetric pairs of channeltrons (A,B) are compared to obtain the scattered beam asymmetry. b) V-LEED set-up: electrons are scattered off a ferromagnetic target crystal. The target crystal has two 90^{o} magnetisation axes allowing for perpendicular components of spin-polarisation to be measured. The polarisation is measured by switching the magnetisation polarity, necessitating only a single detector.

(importantly, the spin-orbit interaction). The electrostatic field of the nuclei of the heavy metal target is experienced by the incoming electrons in their rest frame as a magnetic field. The effective magnetic field can then couple to the spin of the electron through the electron's intrinsic magnetic moment (similar to the spin-orbit effects described in the previous chapter). An incoming beam of spin-up and spin-down electrons scatters producing two outgoing beams that are composed of predominantly spin-up or predominantly spin-down electrons. The scattering process is not 100% efficient (even at a theoretical level), so these scattered beams will not be purely spin-up or spin-down (fig. 3.8a). The efficiency of the asymmetric scattering process increases with the atomic weight of the target $\sim Z^2$ [35]. The scattering process additionally depends on the velocity and angle of the incoming electron beam in a non-trivial and non-monotonic way that can be optimised [36]. Pairs of channeltrons can be placed to measure the asymmetry in the intensity of the scattered beams (nominally being due to the spin-polarisation of the incoming electron beam). At i3, these are placed

such that the spin component perpendicular to the sample surface plane can be measured (out-of-plane), and the component of the spin in the sample surface plane along the slit of the analyser can be measured (in-plane). The efficiency of the individual detectors can also vary, providing an artificial asymmetry in the intensity, so this must also be taken into account.

While Mott scattering makes use of relativistic spin-orbit effects of high energy electrons, V-LEED employs very low energy electrons. In a V-LEED experiment, an incoming beam of electrons is decelerated in the spin transfer lens section to low energies ($E = 6$ eV at APE). The targets used are magnetically ordered (1×1) FeO thin films grown on an MgO substrate. If these FeO surfaces are well prepared, there will be easy axes of magnetisation at 90° to each other in-plane. These can be magnetised with a short current pulse ($I = 5$ A at APE) in solenoids positioned along the in-plane axes of the sample (fig. 3.8b). At APE, there are two targets with four pairs of solenoids. These are positioned such that on one detector S_x and S_z can be measured, and on the other S_y and S_z can be measured. The scattering can take place with the remnant magnetisation of the target. The scattering process is then through exchange scattering, which couples to the incoming electrons spin directly through magnetism. In V-LEED experiments, there is then only the need for a single detector, since the magnetisation can be reversed to measure the spin-up or spin-down electrons. In principle, this removes the need for normalising spectra (as is the case in the geometrically opposed detector set up in a Mott scattering experiment).

In either case, Mott scattering or V-LEED, the polarisation is then given by:

$$P = \frac{1}{S}\frac{I_A - I_B}{I_A + I_B} \tag{3.20}$$

where $I_{A,B}$ is the intensity of a given detector (in the case of V-LEED this is of course the same detector but for opposite magnetisations of the target), and S is the Sherman function. This is simply a number used to correct for the inefficiency of the scattering process. Usually this is calibrated

against a material with known spin-polarisation, such as the Au(111) Shockley surface state (described in the previous chapter). For example, at i3, the Sherman function is $S = 0.17$ meaning an incoming beam of electrons with 100% spin-polarisation (e.g. entirely spin-up electrons) produces a scattering asymmetry of only 17%. That is to say, there will only be a 17% greater intensity on one detector than the geometrically opposed detector (once normalised), despite the fully polarised incoming beam. At APE the Sherman factor is $S \approx 0.3$. The Sherman functions are quoted without error but a quantitative analysis of the spin-polarisation of the measurements presented in this thesis is not necessary for extracting qualitatively the underlying physics.

With the polarisation calculated, the true spin-polarisation of a measured spectrum can be determined using:

$$I^{\uparrow,\downarrow} = I^{tot}(1 \pm P)/2 \tag{3.21}$$

where $I^{tot} = I_A + I_B$. This then scales the measured asymmetry such that it reflects the true spin-polarisation measured.

3.3 Practical considerations

Sections 3.1 and 3.2 cover the main working principles and theory behind ARPES and spin-ARPES measurements but have so far not explained the practicalities of taking these measurements. Since all the ARPES and spin-ARPES results presented were measured at synchrotrons (Cassiopée, SOLEIL; i05, Diamond; i3, MAX III and APE, Elettra) this will be the focus of this section.

3.3.1 Synchrotrons and beamlines

These measurements will sometimes require a dependence on light polarisation or a tuneable photon energy, which necessitates the use of synchrotron light. An accessible introduction to synchrotron radiation and some applications can be found in [37]. The following section summarises some

of the key aspects from this reference, relating to the work carried out in the thesis.

The basic physics underpinning synchrotron operation is that accelerated charged particles emit electromagnetic radiation. Synchrotrons then provide a closed loop for the electron to follow under vacuum. Partly the acceleration is a centripetal acceleration provided by bending magnets. The acceleration is given straightforwardly in this case by the Lorentz equation and the power radiation by relativistic electrons on a circular orbit is given by Schwinger's formula. Together, these provide a loss in energy within a complete orbit around the synchrotron of [37]:

$$\Delta E_e = \frac{4\pi}{3}\frac{e^2}{R}\left[\frac{E}{mc^2}\right]^4 \tag{3.22}$$

where E, m and e are the electron energy, rest mass and charge respectively, and R is the radius of the orbit (or synchrotron ring radius). This loss in energy is compensated by a radio frequency cavity which stabilises the ring energy, as well as quadrupolar magnets for stabilising the trajectory. Additionally, at the relativistic speeds of the electrons in their circular path, the emitted synchrotron light is highly collimated in the propagation direction. This is given by the so-called vertical half-opening angle (fig. 3.9a), which is $\psi = \gamma^{-1} \approx mc^2/E \approx 1/(1957 \times E[\text{in GeV}])$, which for a 3 GeV storage ring would give an angle of $\psi \approx 0.01^{\text{o}}$ [37].

The energy spectrum produced by bending magnets is very broad and not so easily tuneable and the polarisation is not so easily changed (being mostly linearly horizontal polarised). A popular way to easily tune the energy and polarisation of the light is through an undulator (or a wiggler, which is similar in principle). This is a device which is also placed in the straight sections of the storage ring. It typically consists of a periodic array of permanent or electromagnets (fig. 3.9b,c). The magnetic force experienced by the electrons cause them to follow an oscillatory path through the undulator producing highly collimated synchrotron radiation with each oscillation (fig. 3.9a). The sharper bends from the oscillations shifts the peak

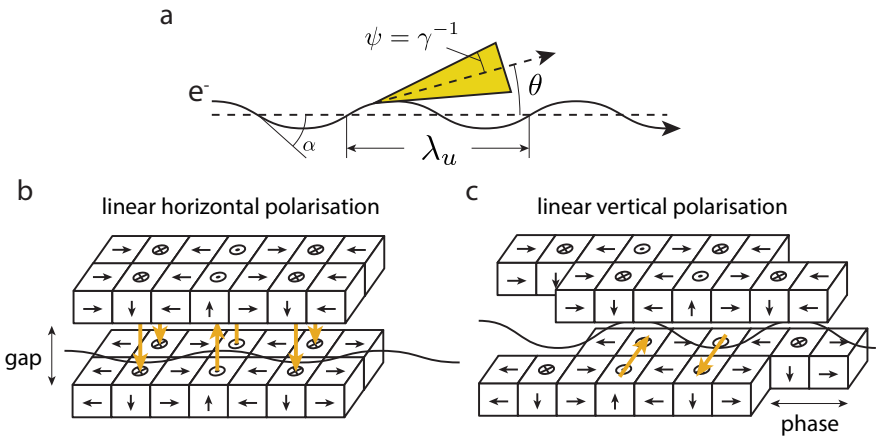

FIGURE 3.9: a) Definitions of physical quantities relating to the trajectory of electrons through the undulator. An undulator (as opposed to a wiggler), has a 'wiggling angle' $\theta \sim \gamma^{-1}$. b,c) Schematics of an APPLE II type undulator design allowing for variable polarisation of light. Alignment of poles producing a vertical field leads to horizontal oscillations and linearly horizontal polarised light (b). Phase offsetting poles forcing in-plane magnetic field lines creates vertical oscillations and therefore linearly vertical polarised light (c). a) Adapted from [37], b,c) adapted from [38].

energy of the emittance to higher energies, since these require greater acceleration. The coherent superposition of synchrotron radiation from the oscillations then provides a greater intensity of radiation (so the intensity is additionally proportional to the length of the undulator). The amplitude of the oscillations can be easily changed (in some undulators) by changing the size of the gap between the magnetic arrays (fig. 3.9b,c), therefore changing the peak in photon energy. A smaller gap, increases the magnetic force experienced by the electrons, providing greater amplitude oscillations, yielding higher energy photons. The wavelength of the light emitted by the undulator is given by the following [37]:

$$\lambda = \frac{\lambda_u}{2\gamma^2}\left(1 + \frac{K^2}{2} + \gamma^2\theta^2\right) \tag{3.23}$$

where λ_u is the period of an oscillation through the undulator given by the distance between magnetic poles (fig. 3.9b), $K = \frac{e}{2\pi mc}\lambda_u B$, for a magnetic field strength B, and θ is the angle of the emitted radiation to the undulator axis (fig. 3.9a). As well as the fundamental wavelength, higher harmonics

in energy (shorter wavelengths) are emitted with $\lambda_n = \lambda/n$.

In addition to the tuneable photon energy, the polarisation vector of the emitted light can be tuned. The polarisation vector is governed by the direction of the oscillations in the trajectory of the electrons through the undulator. The direction of the oscillations through the undulator is defined by the magnetic field set up by the periodic magnetic arrays. This can be achieved in different ways but an example of a modern design of undulator is the APPLE II type undulator shown in figure 3.9b,c. Linearly horizontal polarised light is created when the electrons oscillate in-plane (horizontally), requiring magnetic field lines out-of-plane (vertically). This is achieved by aligning poles such that out-of-plane field lines are aligned vertically across the gap (fig. 3.9b). Conversely, linearly vertical polarised light requires in-plane magnetic field lines. This is achieved by offsetting the adjacent magnetic arrays (a 'phase' shift). It is required that the out-of-plane poles are opposite across the gap, since magnetic field lines cannot cross and this then forces the magnetic field to be mostly in-plane (fig. 3.9c). Instead of shifting the magnetic arrays such that two out-of-plane magnetic poles are aligned laterally, it is possible to adjacently align an in-plane and an out-of-plane array. This creates a magnetic field which forces the electrons to follow a circular trajectory through the undulator, which is effectively a combination of linearly horizontal and vertical polarised light. The handedness of the trajectory through the undulator then defines the polarisation vector of the light to be circularly left or circularly right polarised.

3.3.2 Photoemission end station

Undulators then produce highly collimated light with a tuneable peak in photon energy, and a tuneable polarisation, however the peak still has considerable width in energy. This broad peak must then be monochromated to be practically useful in ARPES measurements. In general at beamlines this is achieved with a diffraction grating, typically with on the order of ~ 1000 lines/mm. Through Bragg's law, this will diffract the incoming light with a wavelength (or equivalently photon energy) given by the incident angle. In

practice this can then be rotated (pitched), to diffract the desired peak wavelength down the beamline. Higher orders of the light from the undulator will of course also satisfy the Bragg condition and so they are not filtered in this way. Since the diffracted light follows Bragg's law, the light resolution will naturally be better at smaller pitch angles of the grating. The monochromated light is then directed down the beamline with a Gaussian spread in intensity and resolution in wavelength away from the centre of the beam. This can be improved by refocussing mirrors, and can be additionally improved by blocking the path of the outermost part of the beam with moveable slits in the path of the beam. Since it is the monochromator which sets the photon energy, the undulator gap can simply be tuned to provide the desired intensity, which is usually desired to be maximised. However, maximising the intensity can sometimes adversely affect the resolution, through the increased density of electrons outside the solid, by electron-electron interactions (space charge effects) so this can be tuned to instead reduce the intensity if required.

Another practical consideration at this stage (light incident on the sample), which can affect the resolution of the measurement, is the temperature at the sample surface. The temperature affects the occupation of electrons, given by the Fermi function (eq. 3.13). This provides all measurements with an energy broadening given by the Fermi distribution with a width k_bT, as well as any temperature dependent interaction effects such as electron-phonon coupling. The temperature can in general be controlled by boiling cryogenic liquid (helium or nitrogen) in a cryostat in the sample manipulator. This has to be thermally connected to the sample, and thermally isolated from the rest of the manipulator and experimental chamber. Typically, the sample is thermally connected to the cryostat by a thermally conductive metal such as copper. This can be done with copper braids, which additionally allow for in-vacuum motion of the sample, which is highly desirable for ARPES measurements. These braids can remove heat from the sample stage on the manipulator to the cryostat, where the boiled exhaust gas then removes this from the system. The range of motion is at least partly governed

by the freedom of movement of the cooling braids and so greater degrees of freedom or range of motion often require a trade off in cooling power. By now there are working manipulators that can reach low temperatures $T = 5$ K as well as allowing for three rotational degrees of freedom, but the design and implementation is a formidable feat requiring great expertise.

As well as the light resolution, and the resolution governed by the temperature which can be externally controlled, the resolution can be further controlled using the analyser. This can be divided into three main parts: the electrostatic lenses in the transfer lens section, the hemispherical deflectors with entrance and exit slits, and the electron detector. The electron detector consists usually of a multichannel plate (MCP), a phosphor screen and a camera. Electrons emitted within an appropriate solid angle from the sample enter the transfer lens section of the analyser, whereby electrostatic lenses resolve their angle, guiding their trajectory into the hemispheres through an entrance slit. As well as passing through the electrostatic lenses, the electrons are additionally accelerated/decelerated in the transfer lens section to an energy called the pass energy E_{pass}, so that they can be more easily measured in the hemisphere section. This also means that only electrons within a range in energy close to the pass energy will pass all the way through the hemisphere section and make it to the detector. A smaller pass energy will therefore equate to a smaller spread of energies on the detector, which is itself a fixed size so there will be a better pixel-to-energy ratio. The resolution of a hemispherical analyser is given by [27]:

$$\Delta E = E_{\text{pass}} \left(\frac{w}{R_0} + \frac{\alpha^2}{4} \right) \tag{3.24}$$

where $R_0 = (R_1 + R_2)/2$ is the mean radius of the outer and inner hemispheres, α is the acceptance angle, and w is the width of the entrance slit.

The most commonly used ARPES entrance slits are rectangular though they can be curved or straight. Due to the electron optics, the paths of the electrons have to cross in angle at the centre of the hemispheres (e.g fig. 3.5). This means for a constant energy, electrons at the edge of the slit will have

a greater path length through the analyser than those at the centre of the slit. This has the effect that a line of constant energy will appear curved on the detector for a straight slit, due to the extra path difference of the electrons crossing at the back of the analyser. This path difference can be calculated and accounted for by the manufacturer, who can provide appropriately curved slits. For the same slit width w these will typically have a marginally worse energy resolution as the straight slit counter parts, but the curved slit will result in a line of constant energy being measured as straight on the detector. The length of the slit is the direction along which the analyser will resolve the angles of the electrons onto the detector (in ARPES lens modes). The width of the slit then defines the amount of integration in the momentum direction perpendicular to the angle resolved direction. This is additionally governed in the software by the angular lens mode, since for the same slit width, a smaller angle mode will then integrate over less perpendicular momentum. This can be an important consideration for highly dispersive features on the sample. Similar to the pass energy, a lens mode resolving a greater angular range spread over a fixed detector size will have a lower pixel-to-angle ratio.

3.3.3 Sample preparation

This covers some of the external ways the resolution of the measurement can be controlled. Concerning the sample, there is of course the intrinsic lifetime broadening, the Fermi function, as well as any interactions that contribute to the self energy. In addition however, any surface contamination will lead to incoherent scattering centres, which can further affect the angle and energy of the photoemitted electrons through elastic or inelastic scattering.

Residual gas adsorption onto the sample surface is governed by the kinetic theory of gases. The rate of adsorption of a number of gas molecules ΔN onto a surface area ΔA (in cm^2) in a time Δt is given by [21]:

$$\frac{\Delta N}{\Delta t \Delta A} = n \left(\frac{P}{\sqrt{MT}} \right) \cdot 4 \times 10^{22} \tag{3.25}$$

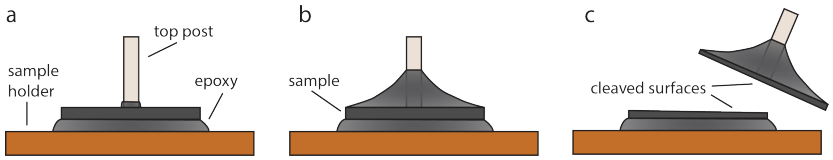

FIGURE 3.10: Cartoon demonstration of sample cleaving. a) Top posted sample bound to sample holder using cured epoxy. b) Meniscus of epoxy binding the top post firmly to the whole sample surface. c) Cleaved crystal revealing two clean surfaces along crystallographic cleavage planes.

where P is the pressure in mbar, M is the molecular weight of the gas, and T is the temperature in Kelvin. Roughly, a monolayer is $\Delta N = 6 \times 10^{14}$ particles per $\Delta A = 1$ cm^2. At a temperature $T = 300$ K and for CO gas ($M = 28$) this can be rearranged to give the total time for a monolayer to form:

$$t = \frac{3.7 \times 10^{-6}}{P \cdot S} \tag{3.26}$$

for a sticking coefficient $0 \leq S \leq 1$. Assuming all molecules stick ($S = 1$), and assuming high vacuum (HV) pressure of $P = 10^{-6}$ mbar, a monolayer will form on the order of seconds. This warrants the need for ultra high vacuum pressures in order to have the cleanest sample surfaces. This additionally improves the inelastic mean free path of the electrons out of the sample and travelling to the analyser which improves resolution.

Of course, simply having a UHV environment is not enough, samples that have been exposed to air will have large contamination layers. Samples must be prepared in situ in order to achieve and maintain clean surfaces. This can achieved in multiple ways including sputtering and annealing, in situ deposition of material or epitaxial growth techniques, or the famous Scotch tape method. However, the technique used exclusively for this thesis will be cleaving bulk crystals (fig. 3.10). This is achieved by gluing the samples to a sample holder using Ag epoxy. This is often Epotek H21D in our case, since it is electrically and thermally conductive, and has low vapour pressure so maintains UHV pressures. It also cures quickly (15 mins, at 120^o). After gluing the sample to the sample holder, we then glue on a small ceramic rod (a top post) that has a smaller diameter than the sample

surface (fig. 3.10a). We then cover the sample surface with epoxy and bind this to the top post (fig. 3.10b) such that the weakest part will be the bonds between cleavage planes of the sample (e.g. weak van der Waals bonds). This is then cleaved in UHV environment revealing a clean surface attached to the sample holder (fig. 3.10c). This works very well for layered bulk materials, which well describes the main samples for which the results are presented in the following chapters.

Chapter 4

Spin-orbital texture of the giant Rashba system BiTeI

4.1 Spin-splitting at the surface of noble metals and alloys

In the last chapters we saw why spin-orbit coupling is now attracting attention and a mechanism for how it can arise in materials with broken inversion symmetry. We began discussing the Au(111) surface state origin and in particular the size of the spin splitting. The surface potential gradient, via the original Rashba model, was shown to be too small an effect to be the sole cause of the spin-splitting. Instead, the strong spin-orbit coupling strength, caused by the large gradient in the potential near the heavy element (Au) atomic cores was found to be a significant factor. The size of the splitting in many materials is actually a combination of multiple factors, including strong spin-orbit coupling strength. Before presenting our results on BiTeI, a semiconductor known to have states that host a large spin-splitting, this chapter will summarise some of the recent advances in understanding what controls the size of spin-orbit splitting in general. Several recent reviews comprehensively discuss this [4, 39], but the salient points are covered here.

There have been studies which have shown that the spin-splitting observed does roughly follow that stronger spin-orbit coupling strengths lead to larger spin-splitting. This is shown for example by the surface states of the similar noble metal Ag(111) [40]. This is a much lighter element than Au

and the spin-splitting is therefore correspondingly smaller, by their calculations. The calculated splitting at the Fermi level, $\Delta E_F = 1.9$ meV, was too small to detect using ARPES. Further, much heavier elements should therefore have a larger spin-splitting from this interpretation. This is observed for example at Bi(111) [41] and Ir(111) [42] surfaces, which have larger spin-orbit coupling strengths than Au, and therefore have correspondingly larger spin-splittings.

Considering quantitative comparisons however, the spin-orbit coupling strength alone could not explain the observed difference in these spin-splittings. For example, the spin-orbit coupling strength of the Au p orbitals is roughly four times higher than that of Ag [40]. However, the spin-orbit splitting at the Fermi level, ΔE_F, is more than 50 times greater in Au than Ag. Making a quantitative comparison for the splitting found in Bi(111) surface states, Bi p orbitals have a spin-orbit strength of $\lambda \approx 1.5$ eV, over three times larger than that of Au. Comparing the splitting in momentum of the band maxima from the $\bar{\Gamma}$ point in both materials, k_0 (fig. 4.1), the splitting is over four times larger in the Bi(111) surface states. This again is quantitatively different from the expectation assuming spin-orbit coupling is the sole factor. Further, the surface states of Cu(111), where the spin-orbit coupling strength of Cu p is a third of that of Ag p [43], should by this naive interpretation have the smallest spin-splitting at the Fermi level. However, recent laser-ARPES measurements [44] show that this actually has a resolvable splitting in momentum at the Fermi level that is four times larger than that calculated for Ag(111). This contradicts entirely what would be expected from the simple spin-orbit coupling strength argument.

The spin-orbit coupling strength not being the sole factor was realised early on by Petersen and Hedegård [24]. In addition to the strength of SOC, they put forward in their model that the asymmetry of the wavefunction in the vicinity of the nuclei at the surface has a significant effect. In their tight binding model, the hopping integral between the in-plane $p_{x,y}$ and out-of-plane p_z orbitals is given by $\gamma = \langle p_z(\boldsymbol{R})|V|p_{x,y}(\boldsymbol{R}+\boldsymbol{x})\rangle$. This is effectively a

measure of the asymmetry of the wavefunction. In the bulk this term vanishes due to inversion symmetry of the bulk crystal structure. However, near the surface the wavefunction experiences inversion symmetry breaking. This reflects the fact that this is a surface state wavefunction and therefore has a decaying amplitude into the bulk. The effect of this is to allow for $p_{x,y}$ orbital mixing near the surface, creating an asymmetry of the surface state wavefunction in the z direction. This then results in a large spin splitting of the electronic structure, from the wavefunction being in the vicinity of the Au cores, where the gradient in the potential is largest. This is supported through experiments by adsorption of Xe on the surface of Au(111) [43, 45]. The surface states of Au(111) under exposure to a monolayer of Xe experience an increased spin-splitting at the Fermi level by $\sim 25\%$. The closed p orbital shell of the Xe means there is little charge transfer between the Xe layer and the Au(111) surface. Through Pauli repulsion, the Au(111) surface state wavefunction is then forced closer to the Au atom cores, experiencing a greater gradient in the potential, therefore increasing the spin splitting [46].

The importance of the asymmetry of the wavefunction itself is also explained using density functional theory calculations on 23 layers of Au(111) by Bihlmayer *et al.* [47]. They demonstrate that the decay of the surface state amplitude into the bulk is what provides the asymmetry, and the large gradient of the potential from the Au atoms is what governs the size of the spin-splitting. Their model also suggests an importance of l to $l \pm 1$ orbital mixing. They are able to explain the difference between the size in the Rashba splitting for the surface states of Ag(111) and Au(111) by the ratio of their d:p and p:s orbital composition. They explain that p orbitals approach the nucleus more closely than d orbitals, and correspondingly lead to a larger splitting. This is supported for example by calculations for an oxygen adsorbate layer on Gd [48]. Before adsorption, the charge density is symmetric in the z direction at the surface (from mainly d_{z^2} orbital character). After introduction of an oxide layer, the charge density is forced to be strongly asymmetric in the z direction in the vicinity of the nuclei. This

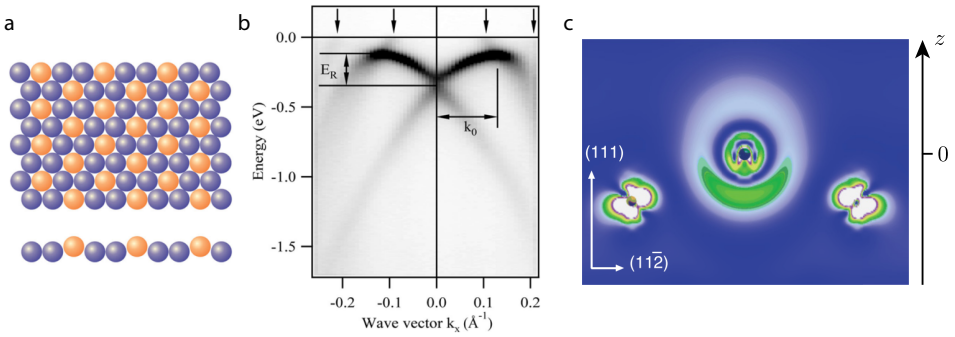

FIGURE 4.1: The crystal structure and electronic structure of the Bi/Ag(111) surface alloy. a) The Bi atoms form an ordered sublattice protruding from the Ag(111) surface. b) The nearly-free-electron-like Rashba splitting shown with double degeneracy cutting through the $\bar{\Gamma}$-point expected for SO splitting. k_0 gives the band offset measured from Γ, and E_R gives the energy offset measured from the degeneracy point. c) Calculation of the partial charge density of the surface state in Bi/Cu(111), showing the asymmetry of the wavefunction near the Bi core (and two Cu atoms). The Bi atom is at $z = 0$ and the vacuum is from $z > 0$ (i.e. in direction of arrowhead). The wavefunction is strongly asymmetric in the vicinity of the nuclei. a,b) Reproduced from [49], c) reproduced from [50].

is mediated by an admixture of p_z orbitals (which are asymmetric in the z direction, due to their phase) into the d orbital Gd surface states.

Clearly therefore, the size of the splitting is ultimately controlled by the spin-orbit strength, the asymmetry of the wavefunction, its orbital composition (particularly orbital mixing) and modifying the surface potential gradient. This can include not only a contribution from an out-of-plane potential gradient, but also an in-plane potential gradient. This is well demonstrated by a class of surface alloys, where heavy atoms (Pb/Bi) are grown with $1/3$ monolayer coverage with a $(\sqrt{3}\times\sqrt{3})R30^{\circ}$ ordering on a substrate, e.g. the (111) surfaces of Ag, Au, Cu, Si (fig. 4.1a) [49–52]. The Bi/Ag(111) band dispersion is shown in figure 4.1b, with the characteristic Rashba split bands. These are split in momentum with the band maxima at a momentum k_0, and a band crossing at the $\bar{\Gamma}$-point, typical of spin-orbit Rashba-like splitting. In Bi/Ag(111), the out-of-plane surface potential gradient and the spin-orbit strength alone could not account for the size of the splitting (fig. 4.1b). This has a sub-monolayer coverage of Bi atoms at the surface and yet

has a Rashba parameter an order of magnitude larger than for the Bi(111) surface, and the largest of any material at this point.

Two models were proposed to described the size of the spin-splitting. One proposal includes the in-plane potential gradient, caused by the hexagonal arrangement of Bi atoms on the Ag(111) surface, as higher order terms in an anisotropic Rashba model [53]. The Rashba model for an isotropic nearly free electron-like dispersion provides $\boldsymbol{k}$-linear Rashba split parabolic bands (chapter 2). Including the effect of the in-plane potential with hexagonal symmetry, they show that this introduces a strong in-plane anisotropy in which the bands deviate from parabolae at high $\boldsymbol{k}$. This in turn enhances the spin-splitting. This anisotropy drives a hexagonal warping of the nominally circular (isotropic) constant energy band contours. In addition, while the conventional Rashba model has fully in-plane spin-polarisation, the in-plane gradient in potential leads to a canting of the spin-polarisation out of the surface plane in the z direction, producing a non-zero S_z component of spin, at these higher in-plane $\boldsymbol{k}$.

In the second model, by Bihlmayer *et al.*, it is suggested that a significant $p_{x,y}$ orbital mixing with the sp_z orbital surface state wavefunction was important [54]. The surface state of Ag(111) is nominally sp_z derived which would yield a typical $\boldsymbol{k}$-linear Rashba splitting, through an out-of-plane asymmetry of the wavefunction. They find however that a relaxation of Bi atoms protruding normal to the surface, or buckling, (fig. 4.1a) induces a mixing of $p_{x,y}$ orbital contribution (consistent with providing an in-plane gradient, as with the model from Premper *et al.* [53]). This in turn drives higher order terms of Rashba splitting which dominate at higher momentum and lead to an enhanced spin-splitting.

From this discussion so far, the size of the spin-splitting is then a combination of factors. The size of the spin-orbit coupling strength is clearly significant. This is influenced by the asymmetry of the wavefunction close to the atomic cores (as in fig. 4.1c). The spin-splitting is enhanced by modifications to the surface potential which either shift the wavefunction with respect to the atomic cores, or modify the potential gradient. Modifying

the potential gradient can additionally promote orbital mixing of in-plane orbitals which drive an in-plane potential gradient. The in-plane gradient (or mixing of in-plane orbital character) in turn can drive an out-of-plane spin-polarisation accompanied by deviations from isotropic constant energy contours and non-parabolicity.

4.2 Giant Rashba splitting in the bulk

4.2.1 Crystal and electronic structure of BiTeI

Up until now, these effects have been exclusively discussed with regards to surface states, where the inversion symmetry breaking is provided by the surface of the crystal. In this section, we will see how these effects are observed in a system with bulk inversion symmetry breaking. In particular, this chapter will focus on BiTeI. A recent review on this material can be found in [55]. BiTeI is composed of heavy Bi, Te and I atoms all with strong spin-orbit coupling strengths, so spin-orbit effects are naturally expected in the presence of inversion symmetry breaking. In this material, while of course it has a surface, the dominant inversion symmetry breaking is in fact within the bulk crystal structure itself.

The bulk crystal structure is described as having covalently bonded $(BiTe)^{+}$ layers (a formal valence of $+1$), which are ionically bonded to the I^{-} layers (a formal valence of -1) [56] as shown in figure 4.2a,b. Each of these Bi, Te and I layers are hexagonal in the a-b plane and stack with an order Te-Bi-I (one unit cell) along the c-axis (fig. 4.2a). Due to the space group ($P3m1$) and the stacking order, this is non-centrosymmetric in the bulk along the c-axis. This can be seen simply by the following: take the inversion centre to be the Bi layer, applying the parity operator maps an I atom onto a Te atom and so the structure is not inversion symmetric. The opposite formal valence of these layers, leads to an effective polarisation vector (or effective electric field) along the c-axis. The effective polarisation, from alternating charged layers throughout the bulk, gives a larger energy scale of the bulk inversion symmetry breaking than the energy scale of the surface inversion

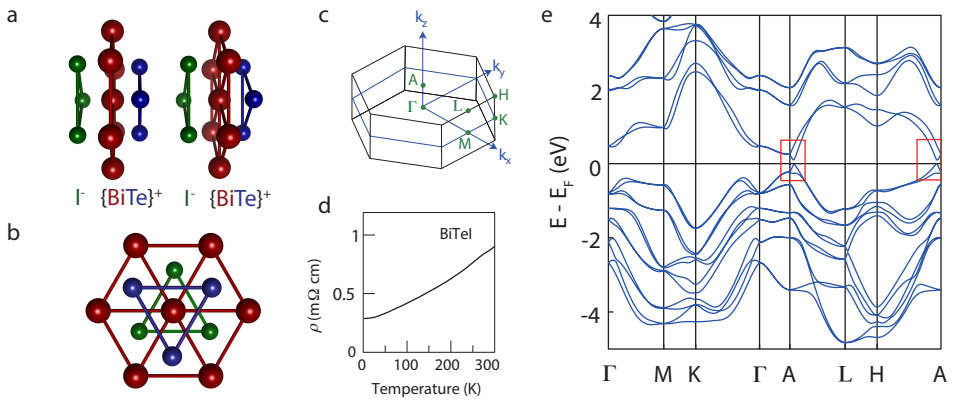

FIGURE 4.2: Atomic and electronic structure of BiTeI. a) Two unit cells of stacked layers of I-Bi-Te along the c-axis and b) triangular orientation of atoms in the a-b plane looking down the c-axis, together show the inversion symmetry breaking. c) Corresponding bulk Brillouin zone. d) Resistivity down to low temperature showing metallic behaviour. e) Fully relativistic bulk band structure of BiTeI showing it to be a narrow band gap semiconductor. The near Fermi level structure which will be the focus is highlighted in the red boxes. c,d,e) Reproduced from [57].

symmetry breaking. This material therefore has atomic species with strong spin-orbit coupling strengths, and inversion symmetry breaking, necessary for spin-splitting of the electronic structure. The crucial difference to the earlier discussion is that the inversion symmetry breaking here is in the bulk.

The bulk electronic structure is then shown in figure 4.2e [57]. This material is a semiconductor with a narrow band gap (confirmed by optical spectroscopy to be $E_G = 0.4$ eV [58]). Transport measurements have shown that BiTeI exhibits metallic resistivity down to low temperatures (e.g. fig. 4.2d), and that the dominant carriers are n-type [59, 60]. BiTeI is then best described as a degenerate n-type semiconductor. The metallic resistivity in the bulk has been described simply by deviations from stoichiometry [59].

The lowest energy band gap is located at the Brillouin zone boundary in k_z and along the A-H direction (fig. 4.2c,e) [57]. The fully relativistic bulk band structure calculation of Ishizaka *et al.* shows spin-orbit split bands near the Fermi level. In particular, looking at the bands along A-H (fig. 4.2e), there are two bands that cross at the A point and have a band minima

at a momenta away from this point. These bands, highlighted in red boxes (fig. 4.2e), will be the focus of this chapter.

The near Fermi level electronic structure, as measured by ARPES (fig. 4.3), resembles the bands from the bulk DFT calculations along the A-H direction. There are two nearly-free electron-like bands at the Fermi level (fig. 4.3). These are separated in momentum, crossing at the $\bar{\Gamma}$ point and have two concentric circular Fermi surfaces. This resembles the standard case for Rashba splitting of a 2DEG. However, the Rashba parameter is reported to be $\alpha_R = 3.8$ eVÅ, which is the largest that has been measured to date (termed a 'giant' Rashba splitting [57]). This is an order of magnitude larger than that of Au(111) and noticeably larger even than the Bi/Ag(111) surface alloy.

These bands were shown to be spin-polarised in a sense consistent with Rashba splitting (i.e. a predominantly in-plane counter-propagating spin texture). This is supported experimentally by the initial spin-ARPES measurements of Ishizaka *et al.* [57] and later spin-ARPES measurements by Landolt *et al.* [61]. This is additionally supported in BiTeI by independent spin-projected DFT calculations [57, 62]. The Rashba splitting of these bands is actually present in bulk DFT calculations, suggesting this must be arising from the bulk non-centrosymmetric crystal structure itself. This is in contrast to the previous section where the Rashba splitting is driven by a surface inversion symmetry breaking. There are then two key aspects to discuss: the size of the spin-splitting being so large, and the Rashba splitting originating from the bulk as opposed to the surface inversion symmetry breaking.

The bulk origin of the Rashba splitting has been confirmed by many independent groups through theory and experiment, as well as for the sister compounds of BiTeX (X = Br, Cl). DFT calculations require periodic boundary conditions and so the simplest way these are performed effectively models a bulk crystal. Numerous DFT calculations have confirmed the bands along A-H to be spin-orbit split in the bulk itself for BiTeI [57, 61–63] and the sister compounds [64–66]. If this was solely an effect arising from the surface, as with the previous section, this splitting should not be present in

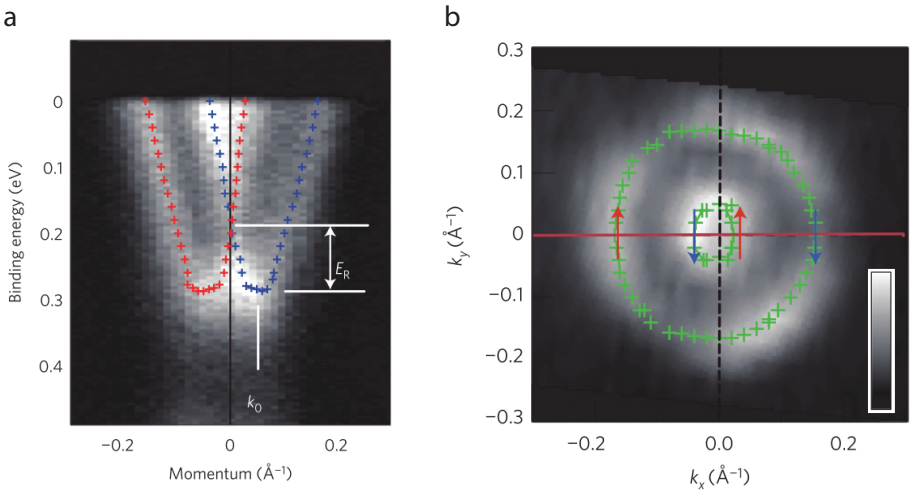

FIGURE 4.3: a) The dispersion shows two spin-split nearly-free-electron-like parabolae. b) The Fermi surface has two concentric circular contours with an in-plane counter propagating spin texture confirmed by spin-ARPES and DFT. These findings are consistent with Rashba split bands. Reproduced from [57].

the bulk calculations.

Additionally, the spin-splitting is confirmed to be a bulk effect by two soft X-ray ARPES studies (SX-ARPES) [61, 67]. As mentioned in chapter 3, often ARPES experiments are in the vacuum ultra-violet (VUV) range ($h\nu \sim 30$ eV) for the highest surface sensitivity. SX-ARPES experiments, on the other hand, exploit higher photon energies (e.g. 310-850 eV in [61]) to allow for a greater mean free path of the photoexcited electrons. These experiments are therefore slightly more bulk sensitive and integrate over less k_z. The higher photon energies also mean neighbouring Brillouin zone boundaries along k_z are more separated in $h\nu$ than VUV-ARPES. These make it better than VUV-ARPES at probing bulk (3D) dispersive bands. Both groups (Landolt *et al.* and Sakano *et al.*) were able to see a bulk dispersive feature at the Fermi level [61, 67]. This is entirely consistent with the DFT calculations showing this band along A-H to disperse in the k_z direction along Γ-A, further confirming this to be a bulk Rashba splitting.

The reason for the Rashba splitting being so large is explained in more detail by Bahramy *et al.* [68], following their initial discovery. They use $\boldsymbol{k} \cdot \boldsymbol{p}$ theory [14, 23], in which the Hamiltonian for a point $\boldsymbol{k}$ can be written as the

sum of the Hamiltonian at a nearby momentum $\boldsymbol{k}_0$ and a perturbation term in $\boldsymbol{q} = \boldsymbol{k} - \boldsymbol{k}_0$. They derive the following expression for the energy splitting through second order perturbation theory of the resulting Hamiltonian:

$$\Delta\varepsilon_m^{(2)}(\boldsymbol{k}) = \frac{\hbar}{m_0} \sum_{n \neq m} \frac{\langle u_m | H^{(2)} | u_n \rangle \langle u_n | \boldsymbol{q} \cdot \boldsymbol{p} | u_m \rangle + c.c}{\varepsilon_m - \varepsilon_n} \tag{4.1}$$

where $H^{(2)} = \frac{\hbar^2}{4m_0^2c^2}(\nabla V \times \boldsymbol{p}) \cdot \boldsymbol{\sigma}$ and is effectively the spin-orbit term arising from the atomic orbital momentum, and u_i and ε_i are the eigenstates and eigenenergies around the $\boldsymbol{k}_0$ where the expansion is valid [68]. This term (eq. 4.1) then has three independent parts, each of which contribute to the giant spin-splitting. Firstly, equation 4.1 depends on the size of the spin-orbit splitting (through the matrix elements of $H^{(2)}$), which is predominantly from the strong spin-orbit coupling strength of bismuth (they quote as $\Delta_{so} \sim 0.5$ eV). Secondly, the spin-splitting depends on the size of the band gap (though the denominator $\varepsilon_m - \varepsilon_n$), since this effect is derived from a coupling of the valence and conduction bands. It is divergent as ε_m approaches ε_n, i.e. enhanced by a smaller band gap. The spin-splitting is therefore increased by the narrow band gap of BiTeI ($E_G = 0.4$ eV [58]). Thirdly, the $5p_z$ chalcogen bands are split above the $5p_{x,y}$ bands for the valence bands, which is opposite for the Bi $6p$ conduction bands above the Fermi level (a so-called negative crystal field splitting of the chalcogen bands). This is seen schematically in figure 4.4. The negative crystal field splitting therefore gives a non-vanishing overlap of u_m and u_n in equation 4.1 since these are the same symmetry character, resulting in a larger spin-splitting.

4.2.2 Bulk Dirac point in BiTeI

This negative crystal field splitting has another consequence: the band level schematic of the bands near the Fermi level is then very similar to that of the bismuth chalcogenide topological insulators [69, 70]. Owing to their similar crystal structures, both contain hexagonal layers of alternating atomic character, however Bi_2Se_3 retains global inversion symmetry. In both Bi_2Se_3 and BiTeI, the bands nearest the Fermi level are predominantly Bi p_z

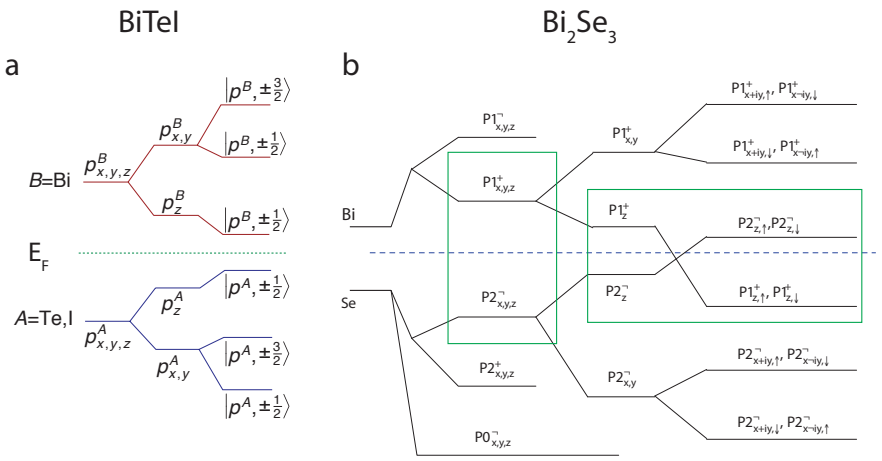

FIGURE 4.4: Band level diagram for (a) BiTeI and (b) Bi_2Se_3. The branches correspond to splittings after: (anti-)bonding, crystal field, then spin-orbit for both (a) and (b). Generically, VBs composed of chalcogen, and CBs composed of Bi. The band inversion in Bi_2Se_3 additionally induces a topological surface state. (a) Reproduced from [70], (b) from [69].

and chalcogen p_z (fig. 4.4). In Bi_2Se_3, the SOC is strong enough to drive a band inversion of opposite parity bands, and a topological surface state is well known to exist in the inverted band gap [69, 71–73].

In fact, BiTeI is close to a topological phase itself. It was predicted theoretically that applying pressure would drive a band inversion of the bismuth and chalcogen p_z bands close to the Fermi level (fig. 4.4a), driving BiTeI into a topological phase [70]. Several experiments have reported a phase transition occurring as a function of pressure [74–79], but there is significant discrepancy among the critical pressure at which this transition occurs (predicted to be between $P_c = 1.7 - 4.1$ GPa [70]). These pressures are anyway however experimentally difficult to reach using ARPES.

While it has a topological phase transition under pressure, even at ambient pressure BiTeI has a so-called π-Berry's phase. A wave undergoing a closed orbit would be expected to return to its initial parameters (amplitude and temporal phase) but Berry described that in certain cases it can acquire an additional geometrical phase [80]. In the solid state this is described as electrons making a closed path in the Brillouin zone and if it encloses a degeneracy point it acquires a Berry's phase [81] (see fig. 4.5), which is known to exist for example in graphene as observed by quantum

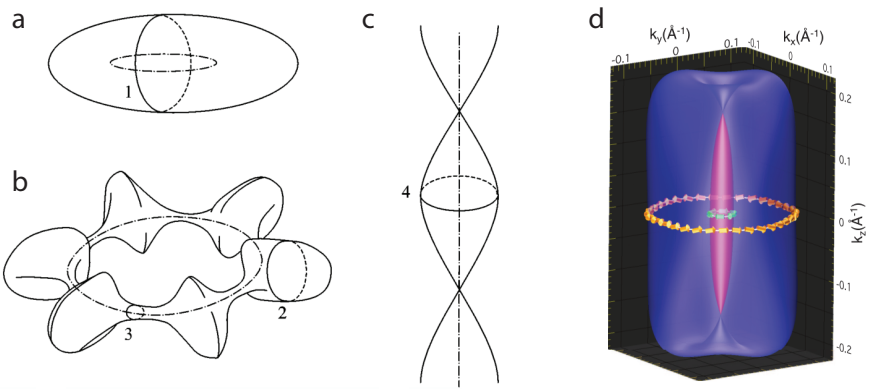

FIGURE 4.5: a,b,c) Different Fermi surface geometries and example closed loops. Loops 1 and 2 acquire a trivial Berry's phase, while 3 and 4 encircle a degeneracy point and acquire a non-trivial Berry's phase. d) Calculated Fermi surface of BiTeI. Both inner and outer Fermi surfaces, (a,b,c) Reproduced from [81]. (d) Reproduced from [70].

oscillations [69]. The surface states in topological insulators also acquire a non-trivial (π) Berry's phase, as the electron orbits the Dirac point [6, 82]. In BiTeI, a π-Berry's phase is observed for both the inner and outer Fermi surfaces as a phase shift in Shubnikov-de Haas oscillations [83]. This is indicative of the orbits enclosing a bulk Dirac point in BiTeI (fig. 4.5d), i.e. a Dirac point along k_z. This is consistent with the assignment of a bulk Rashba splitting observed in SX-ARPES and DFT calculations, corresponding to a toroidal Fermi surface (fig. 4.5d). Evidence for a bulk Dirac point in BiTeI have now been observed through quantum oscillations by several groups [84–86].

4.2.3 Surface effects in BiTeI

As discussed, the normal state of BiTeI (a topologically trivial semiconductor) is then well established to host a bulk Rashba splitting. However, ARPES is inherently a surface sensitive technique and as such there has been some controversy over the nature of the state being probed at the surface. The surface is exposed upon cleaving, with the cleavage plane lying between the greater-separated, ionically-bonded Te-I layers (figs. 4.2a or 4.6b,c). This reveals a polar surface of either tellurium (positively charged),

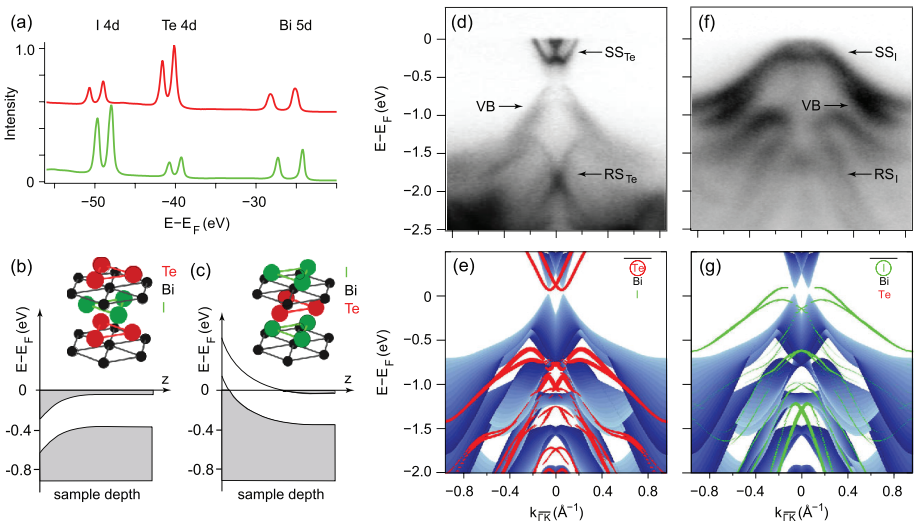

FIGURE 4.6: Surface band bending potentials in BiTeI from [63]. a) Core level shifts indicative of different surface potentials arising from tellurium (red trace) or iodine (green trace) surfaces. Schematic band bending for tellurium shown in (b), and for iodine (c). Measured (d) and calculated (e) band dispersions for tellurium surface and iodine surface (f,g). Figure taken from [63].

or iodine (negatively charged) termination. Surfaces that are not charge neutral (polar) are unstable and so undergo some reconstruction (structural or electronic) to lower their energy. The ionic charge at the polar surface induces an electric field that must be screened by the conduction electrons. This happens at a length scale on the order of the Thomas-Fermi screening length [20], given by: $r_{TF} \approx 0.5(n/a_0^3)^{-1/6}$, where n is the electron density, and a_0 is the Bohr radius. In metals, there is a large free carrier density and so the ionic charge is efficiently screened over a small length scale (on the order of Ångstroms). In the case of the degenerate n-type semiconductor, BiTeI, the screening leads to surface charge accumulation layers of several tens of Ångstroms [57, 63]. The potential at the surface experiences a gradual change from the bulk potential corresponding to the accumulation of additional charge, leading to surface band bending (fig. 4.6b,c and fig. 4.8a). The band bending raises or lowers the potential at the surface relative to the bulk potential, dependent on the termination. One result of this is that the bands observed in photoemission are shifted in energy, comparing the two terminations.

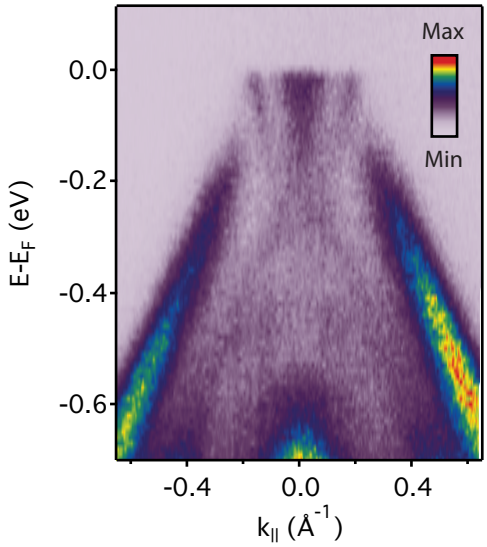

FIGURE 4.7: ARPES measurement of the near Fermi level electronic structure with the light spot illuminating a mixture of both tellurium and iodine terminated surfaces.

In the case of the tellurium termination, the reduction in the surface potential compared with the bulk potential shifts the bands to higher binding energies. This can be seen in X-Ray photoemission spectroscopy (XPS) measurements (e.g Crepaldi *et al.* fig. 4.6a,b). All the core level binding energies are shifted to lower binding energies corresponding to the downwards band bending. The tellurium core level peaks are also correspondingly more intense, due to the tellurium termination. The Rashba split electron-like conduction band is then observed at the Fermi level, corresponding to the bands shifting to higher binding energies (fig. 4.6d).

For the iodine termination, there is a negative ionic charge at the surface, which results in a hole-like inversion layer (accumulating holes at the surface, with an electron-like bulk). The surface potential is raised in energy compared with the bulk potential, shifting the bands to lower binding energies. The XPS spectra then show that the core levels are shifted to lower binding energies with respect to the tellurium surface (fig. 4.6a,c). At these surfaces, Rashba split hole-like valence bands are observed close to the Fermi level (fig. 4.6f).

Stacking faults or other defects mean that the surface exposed is often a

mixture of tellurium and iodine terminations randomly distributed with a domain size estimated from STM to be $\sim$ 100 nm [87]. This is smaller than the typical size of a conventional ARPES beam spot ($\sim$ 50-100 μm) and so often a superposition of the two is observed in the measurements (fig. 4.7). However, it is not impossible to measure on a predominantly tellurium or iodine termination. While the polar surface leading to surface band bending is now well established and generally agreed upon, there are however two proposals as to the origin of the near-Fermi level state being probed in VUV-ARPES: a quantum well state, or a true surface state.

4.2.4 Nature of the near Fermi level states at the surface of BiTeI

In the initial work of Ishizaka *et al.* [57], using a low-$h\nu$ laser, the authors observe spectral features beyond what would be expected for a single nearly free electron-like Rashba split band. For a conventional Rashba split band there would be two parabolae in the measurement, with band minima at $\pm k_0$. They see what could be described as two additional parabolae at lower binding energy (fig. 4.8a,b). These spectral features were not present in their He lamp data potentially owing to the increased $\boldsymbol{k}_{||}$ resolution of laser-ARPES.

If there was no band bending, the conduction bands measured at the surface would be at the same energy as those in the bulk. The downwards band bending pushes the conduction bands measured at the surface to higher binding energies. The downwards band bending (at a Te surface) from the bulk potential, and the step up to the vacuum potential was originally suggested by Ishizaka *et al.* to act like an asymmetric quantum well. This quantum well-like potential would then confine electron-like states and produce a ladder of quantised subband states. The lowest energy subband would then be at the zero-point energy of the quantum well-like potential. The quantum well potential given by the band bending can be difficult to treat. Ishizaka *et al.* adopt a Poisson-Schrödinger approach [88] and model the additional state from their laser-ARPES measurements as the second subband in a ladder of quantum well states. Assuming the bulk carrier concentration

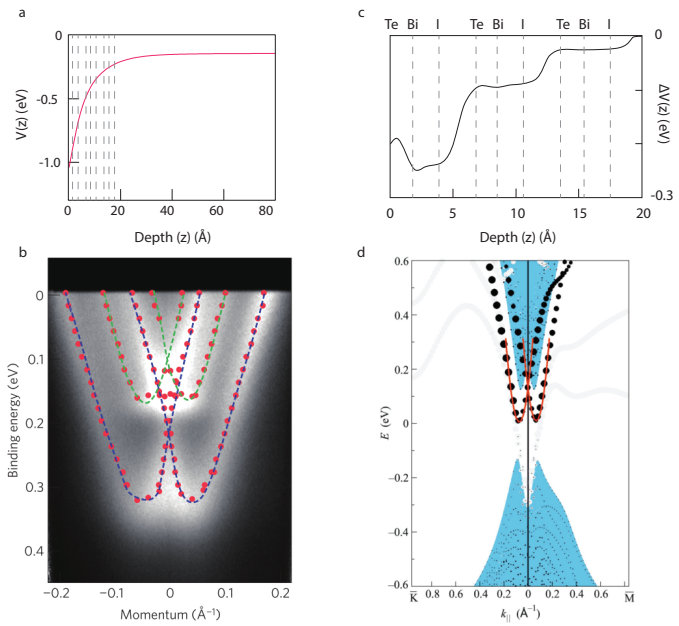

FIGURE 4.8: Two proposals for modelling the surface potential and origin of the states observed at the surface. a) Quantum well potential from surface band bending confines bulk states in ladder of QWS, observed by laser-ARPES in (b). c) Step-wise potential from strong ionicity and breaking translational symmetry splits-off and confines states to triple layer as calculated in (d). The potential is mostly unchanged from the bulk potential, in both cases, by about 20 Å from the surface. Grey dotted lines in both correspond to TLs of Te-Bi-I. (a,b) Reproduced from [57], (c,d) reproduced from [62].

from transport measurements ($n_H = 4.5 \times 10^{19}$ cm^{-3} [59, 60]) and calculating the surface carrier concentration from their observed Fermi surfaces ($n = 4 \times 10^{20}$ cm^{-3}), they get reasonable agreement between the calculated band bottoms for the first and second subbands, and the spectral features observed in their ARPES measurements. The observed surface carrier concentration is consistent with a rigid shift downwards in energy as a result of the band bending potential.

The opposing interpretation for the origin of the states observed at the surface is that these arise as a result of the surface atoms experiencing a reduced symmetry from the bulk environment (from the lack of neighbours in the z direction) and therefore also a reduced potential. Initial theoretical work lead by Chulkov [61, 62] confirm through DFT slab calculations that an additional Rashba split surface state appears at higher binding energies

(e.g. fig. 4.8c,d). This is confined to the surface layers as a result of the stepwise potential arising from the layered crystal structure along the c-axis. This produces a true surface state that is split-off from the bulk states. Since this state is a result of the change in potential of the near surface layers, and not a chemical change or reconstruction, it is still representative of the bulk electronic structure and 'inherits' the bulk Rashba splitting and spin-polarisation of the bulk states [62]. This is supported by the coexistence of a 2D state and a 3D dispersive state observed in $h\upsilon$-dependent ARPES by Landolt *et al.* [61].

Further, work from Crepaldi *et al.* shows the same 2D state as a function of photon energy. Through surface potassium dosing they artificially increase the strength of the band bending at the tellurium surface [63]. They observe the bandwidth and the Fermi momentum increase as a function of potassium dosing as a result of the increased free carriers being donated but the splitting in momentum at the Fermi level remains constant. If the splitting was a result of the asymmetric potential of the surface quantum well, the splitting would be expected to increase, confirming the splitting to ultimately originate from the bulk. They estimate the band bending to be increased by the surface dosing by $> 40\%$, but no change to Δk_{SO} within error, whereas in the conventional Rashba model, since $\alpha_R \propto E_z$, this would result in a corresponding increase in Δk_{SO}. This is in fact consistent with Ishizaka *et al.* who state that the splitting is predominantly inherited from the bulk states and is enhanced by only a small fraction from the surface quantum well [57].

Reports on the sister compounds BiTeX (X = I, Br, Cl) all show evidence of similar Rashba split states but with differences in band widths, and splittings [64–66]. In the case of BiTeBr from Sakano *et al.*, there are even three subbands of the quantised bulk state visible, which are reasonably sharp indicating their probable two-dimensional nature. The binding energies of the band bottoms agree with their PS calculations, supporting their conclusion that these are quantum well states. To the contrary, Eremeev *et al.* propose that multiple surface states can exist 'split-off' from the bulk states at the

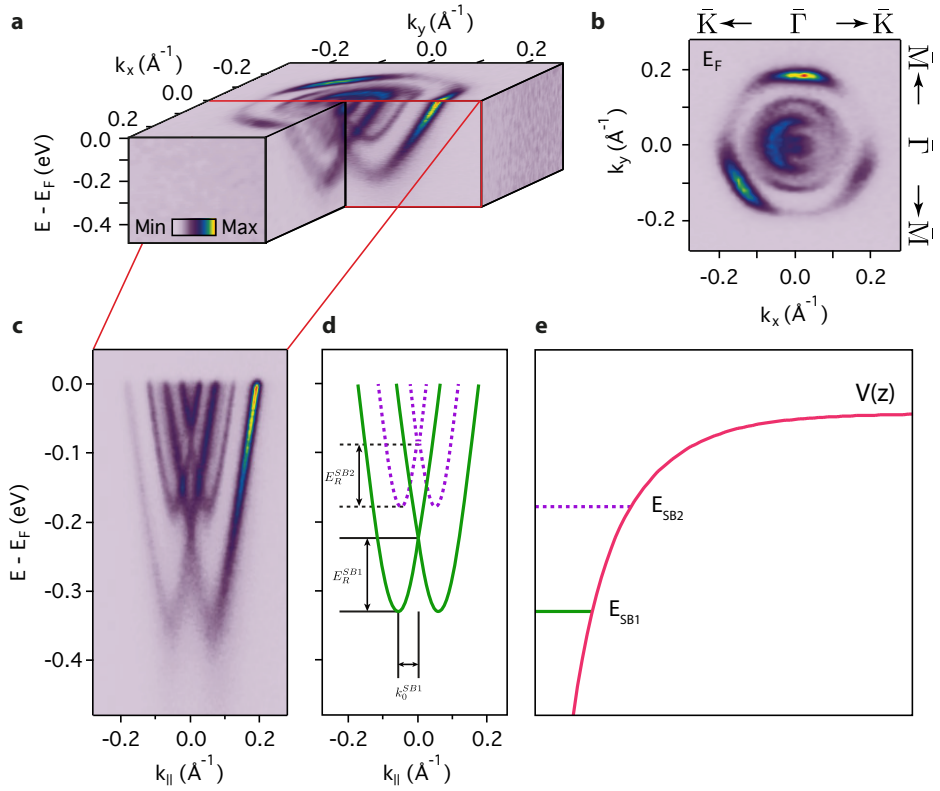

FIGURE 4.9: High resolution ARPES of near Fermi electronic structure of BiTeI on the tellurium surface measured at $h\upsilon = 52$ eV with p-polarised light. a) Dispersions along $\bar{\Gamma}$-$\bar{\mathrm{K}}$ and $\bar{\Gamma}$-$\bar{\mathrm{M}}$. b) Corresponding Fermi surface. c) High resolution dispersion along $\bar{\Gamma}$-$\bar{\mathrm{M}}$ showing multiple subband states of the quantised bulk Rashba split state. d) Guides to the eye for the subband states. Green solid lines correspond to the first subband (SB1) of Rashba split parabolae, and purple dashed lines correspond to the second subband (SB2). e) A cartoon band bending potential $V(z)$ near the surface in the z direction. The energy of SB1 and SB2 are schematically shown indicating the purple dashed lines are higher in the quantum well than the green solid lines.

different trilayers (Te-Bi-I) along the c-axis. These are bound to the surface by the barrier formed as the stepwise potential steps up to the bulk potential [65]. At certain k_z the lower binding energy (high subband) split-off states overlap the bulk states according to their calculations.

Our measurements on BiTeI provide evidence for the quantum well-like interpretation of the states observed at the surface. Our measurements have been carried out at a combination of the i05 beamline at Diamond Light Source, UK, and the Cassiopée beamline at SOLEIL, France, both allowing variable linear and circular polarisation and variable photon energy in the

VUV range. The light spot is small enough ($\sim$ 50-100 μm) in both cases that we can probe a region we determine to be predominantly a tellurium terminated surface. We initially determine this from core level shifts and reducing the contribution from the lower binding energy peak corresponding to the iodine surface. This can be confirmed from the near Fermi level electronic structure in which the downwards band bending pulls the conduction band down. This then shows electron-like states at the Fermi level. We can optimise our light spot on the sample by reducing the spectral weight from hole-like states observed at the same binding energy on the iodine terminated surface (fig. 4.7). In principle, the XPS measurements themselves, as well as showing the difference in potential between the two surface terminations, could show the difference in potential between split-off (or subband) surface states and the bulk. This effect is similar between the two theoretical interpretations and subtle compared with the magnitude of the potential difference induced by the band bending and the linewidth of the XPS spectra. Analysis of this would be challenging and interesting but is not a focus of this thesis.

Figure 4.9 shows our measurements of BiTeI of the near Fermi level states. In figure 4.9c, there are multiple dispersive features evident. For a Rashba split 2DEG, we would expect a single parabolic band split into two parabolic bands separated in momentum from the $\bar{\Gamma}$-point by k_0 (e.g. green solid lines in fig. 4.9d). These would give two concentric circular Fermi surfaces. Cutting this along a high symmetry direction e.g. $\bar{\mathrm{M}}$-$\bar{\Gamma}$-$\bar{\mathrm{M}}$, this would give four Fermi crossings (two crossings from each of the two parabolae). We have stated that the tellurium termination leads to a downwards band bending which can be treated as a quantum well potential at the surface (fig. 4.9e). This quantises the bulk Rashba split states in a ladder of subband states at different binding energies lower than the zero point energy. Each subband state will therefore contribute two concentric Fermi surfaces, and four Fermi crossings in a cut along a high symmetry direction. In our data, in figure 4.9b, we clearly see four concentric Fermi surfaces.

This is an indication that we might be probing two subband states. Measuring a dispersion along the high symmetry direction $\bar{\mathrm{M}}$-$\bar{\Gamma}$-$\bar{\mathrm{M}}$ (fig. 4.9c), we clearly see eight Fermi crossings. These can be attributed to two subband states. Tracing the outermost crossings in the data (corresponding to solid green line in fig. 4.9d), these disperse in energy down to a conduction band minimum for this Rashba split state at $E_{CBM}^{SB1} = 340 \pm 10$ meV. This is the deepest binding energy state and so corresponds to the first subband (SB1) of the quantum well. This Rashba split subband state is clearly composed of two approximately parabolic bands which are separated in momentum by $k_0^{SB1} = 0.055 \pm 0.005$ Å^{-1} from the $\bar{\Gamma}$-point, crossing at an energy $E_R^{SB1} = 120 \pm 10$ meV from the CBM, extracted from fits. There are clearly an additional set of bands at lower binding energy, with band minimum, $E^{SB2} = 175 \pm 5$ meV, corresponding to the second subband state (SB2) (dashed green line in fig. 4.9d). These are also noticeably Rashba split and through fitting we can extract a Rashba energy, $E_R^{SB2} = 85 \pm 5$ meV, and CBM splitting $k_0^{SB2} = 0.050 \pm 0.005$ Å^{-1} assuming a simple parabolic model.

From our data there is a very clear hexagonal warping of the outer Fermi surfaces, with the warping being greatest along the $\bar{\Gamma}$-$\bar{\mathrm{K}}$ direction. At higher in-plane momentum, the simplified Bychkov-Rashba model [2] becomes a less appropriate approximation and higher order terms to the Rashba Hamiltonian arising from a $\boldsymbol{k} \cdot \boldsymbol{p}$ interaction can be included subject to the symmetry constraints of the crystal structure [23]. Anisotropy of the bands leading to hexagonal warping at higher $\boldsymbol{k}_{||}$ has been seen in the related surface states for bismuth chalcogenide topological insulators (e.g. [73]) and for several other strong spin-orbit materials (e.g. [49]). For C_{3v} symmetry, this is introduced for the TI surface states by Fu [89], and by Frantzeskakis and Grioni for the spin-orbit materials with the same symmetry [90]. The C_{3v} (trigonal) crystal field has also been proposed by Ishizaka *et al.* to be the cause of the hexagonal warping of these bands, adding a term in the Hamiltonian proportional to $(3k_x^2 - k_y^2)k_y\sigma_z$ [57]. The hexagonal warping of the bands is clearly present in at least the outer most of our measured

Fermi surfaces. This can be understood since this term is cubic in $\boldsymbol{k}$ and so becomes more significant at high in-plane momentum. This appears in the Hamiltonian with the following form:

$$H(\boldsymbol{k}) = E_0(\boldsymbol{k}) + \alpha_R(k_x\sigma_y - k_y\sigma_x) + \frac{\lambda}{2}(k_+^3 + k_-^3)\sigma_z \tag{4.2}$$

where $E_0(\boldsymbol{k})$ is the free-electron kinetic energy term, the second term is the typical $\boldsymbol{k}$-linear Rashba Hamiltonian, and the third term is the $\boldsymbol{k}$-cubic term with $k_\pm = k_x \pm ik_y$. This gives the dispersion relation:

$$E_\pm(\boldsymbol{k}) = E_0(\boldsymbol{k}) \pm \sqrt{\alpha_R^2 k^2 + \lambda^2 k^6 cos^2(3\theta)} \tag{4.3}$$

where θ is the azimuthal angle the $\boldsymbol{k}$ vector makes with the x-axis ($\bar{\Gamma}$-$\bar{\mathrm{K}}$ direction), and the two eigenvalues $E_\pm$ correspond to the bands above and below the Dirac point. A consequence of this Hamiltonian now not explicitly excluding σ_z (as the Rashba-Bychkov model does), is that the S_z component of spin increases as a function of momentum. The anisotropic hexagonal warping at higher momentum is included in calculations for BiTeI in the initial work of Ishizaka *et al.* [57], and as expected from the higher order correction it drives a canting of the spin vector in the out-of-plane direction. This canting of the spin in the out-of-plane direction at high $\boldsymbol{k}$ as a result of warping is well known in topological insulators and has been measured in spin-ARPES experiments [91]. There is therefore some evidence for this warping term in BiTeI.

Additionally, from this formula for the dispersion relation (eq. 4.3), along the $\bar{\Gamma}$-$\bar{\mathrm{M}}$ direction with $\theta = 30^{\mathrm{o}}$, the contribution which is cubic in $\boldsymbol{k}$ vanishes. This then reduces to the simple parabolic 2DEG case with a linear Rashba splitting along this direction. It has been suggested that these bands have a non-parabolicity beyond a simple 2DEG model [57, 62]. In our data, there is hexagonal warping of the outer band, with the corners of the hexagon pointing along the $\bar{\Gamma}$-$\bar{\mathrm{K}}$ direction. However, the dispersion (fig. 4.9c) along $\bar{\Gamma}$-$\bar{\mathrm{M}}$ is still clearly not perfectly parabolic. Equation 4.3 does not then fully explain the non-parabolicity of these bands in BiTeI as they have

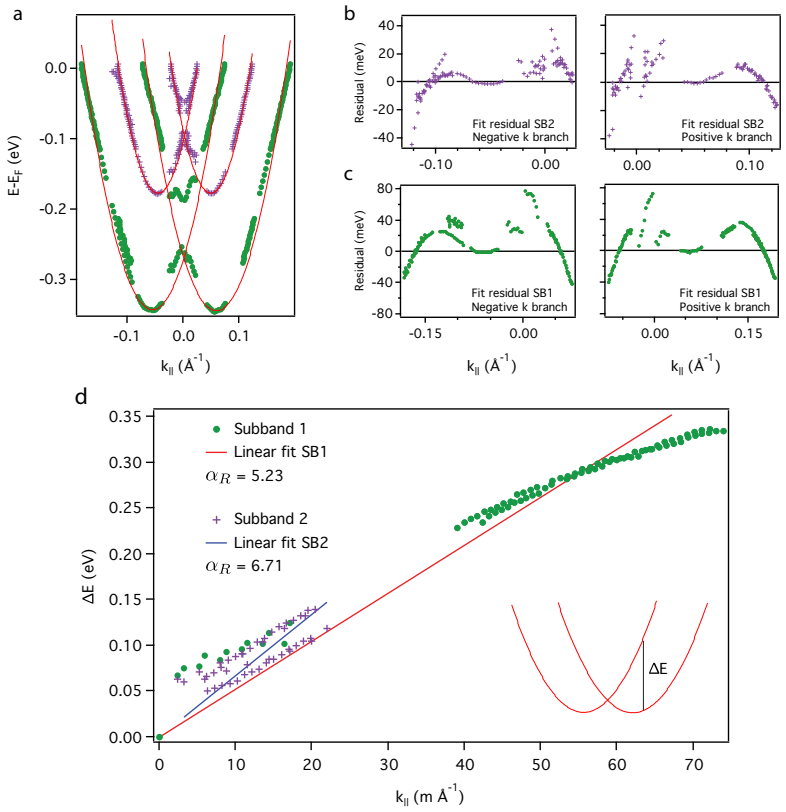

FIGURE 4.10: Conventional Rashba model fit to BiTeI quantum well subbands. a) Extracted positions of SB1 (green circles) and SB2 (purple crosses) and corresponding parabolic fits. b,c) Fit residual for each SB2 (b) and SB1 (c). d) ΔE vs $\boldsymbol{k}_{||}$ for the two subbands. In the conventional Rashba model, the gradient is a constant equal to the Rashba parameter.

done in other strong spin-orbit materials [89, 90]. We can show this simply by fitting the position of the bands in our data and assuming a parabolic 2DEG model. The results are shown in figure 4.10.

In figure 4.10a, the extracted peak positions of the dispersion in figure 4.9c are shown. These are all Lorentzian fits with the band bottoms being better fit by EDCs and the band tops being fit better by MDCs. The red lines correspond to fitting these extracting peak positions to a conventional parabolic Rashba model. These are obtained by fixing the band bottom in all cases. For both subbands, the Kramer's degenerate crossing of the bands is significantly underestimated. In addition, towards the band bottoms of all subbands and branches (positive and negative momentum offset), the dispersion peak positions are lower in binding energy. This switches towards the band top where the peak positions are higher in binding energy than the

parabolic fit. This is verified by the fit residual, defined as the difference in energy between the fit and the data. Non-random structure in a residual can be an indication that the chosen fit function is not sufficient. This has important implications for defining the strength of the Rashba interaction in this material. The Rashba parameter is typically extracted assuming a parabolic 2DEG model. This is shown in figure 4.10d. The difference in energy, ΔE, for peak positions extracted away from $\boldsymbol{k}_{||} = 0$ (as shown in the inset) is plotted for each subband, for the range of data available. In a conventional Rashba split 2DEG model, plotting ΔE vs $\boldsymbol{k}_{||}$ yields a straight line through the origin with a gradient equal to the Rashba parameter, α_R. This has a clear deviation at higher in-plane momentum, though even close to the $\bar{\Gamma}$ point this is not ideally Rashba-like. The Rashba parameters obtained are also well in excess of the value published by Ishizaka *et al.* of $\alpha_R = 3.8$ eVÅ, despite the band offset, k_0, and Rashba energy E_R being comparable [57].

This could be explained as resulting from non-parabolicity from a coupling between the valence and conduction band in a $\boldsymbol{k} \cdot \boldsymbol{p}$ formalism since this material has a narrow band gap and states near a high symmetry point [14]. This material is clearly well described within a $\boldsymbol{k} \cdot \boldsymbol{p}$ formalism since the work of Bahramy *et al.* does an excellent job at reproducing the size of the spin-splitting (eq. 4.1) [68]. The narrow band gap allows for greater coupling of upper valence bands, and lower conduction bands, and these states are located at small $\boldsymbol{k}$ around the $\bar{\Gamma}$ point, so a $\boldsymbol{k} \cdot \boldsymbol{p}$ expansion is valid. In the limit that $\Delta_{SO} \ll E_G$, this method provides a functional form that makes the dispersion more linear away from the band bottom [14, 88]. This limit is however inappropriate in the case of BiTeI and a more involved derivation from $\boldsymbol{k} \cdot \boldsymbol{p}$ theory is required [92], outside the focus of the results presented in this chapter. Additional deviations from parabolicity have recently been observed in Rashba split states of the surface quantised bulk bands in Bi_2Te_2Se [93]. There, the anisotropy was explained as further higher order corrections, which include the non-parabolicity as an extra $\boldsymbol{k}$-cubic term (following [94]), as well as an effective mass which is anisotropic in azimuthal angle. The origin of the non-parabolicity is still then not well understood

and will require more detailed theoretical treatment to uncover the full dependence of the spin-splitting in this material. The non-parabolicity does not have an effect the main conclusions of this thesis but our measurements demonstrate there is non-parabolicity of the bands beyond simply a higher order Rashba term.

Beyond the non-parabolicity and anisotropy, our data show that all eight of these Fermi crossings have small linewidths (fig. 4.9c). At these low photon energies, small linewidths can be an indication of the two-dimensional nature of the underlying states (discussed in Chapter 3). To further confirm the 2D nature of all eight of these crossing we have performed photon energy dependent ARPES.

Figure 4.11 shows an MDC measured at the Fermi level for the QWS at the tellurium terminated surface of BiTeI for $h\nu = 30 - 70$ eV (1 eV steps) using p-polarised light. From figure 4.9 it is clear there should be eight peaks in the Fermi level MDC, all of which we see clearly in figure 4.11, across a range of photon energies (prominently, for example at $h\nu = 52$ eV). These peaks are well fit by Lorentzian profiles and resolvable for a wide range of photon energies. For all eight peaks, the peak position does not change significantly with photon energy, as might be expected from the bulk band calculations along the direction Γ-A. This indicates negligible out-of-plane dispersion for all eight crossings. The c-axis lattice parameter is $c = 6.854$ Å [56], giving an approximate Brillouin zone spacing of $k_z = 2\pi/c \approx 0.917$ Å^{-1}. At $\boldsymbol{k}_{||} = 0$, assuming an inner potential as given by Landolt *et al.* [61], this gives a range of $k_z \approx 2.5 - 4.1$ Å^{-1} for our photon energy range $h\nu = 30 - 70$ eV, so these states are dispersionless for a full Brillouin zone in k_z, indicating their 2D nature. The peaks are clearly resolvable for (at least) a full Brillouin zone with minimal diffuse intensity corresponding to bulk states observable (i.e. dispersive features).

The additional fully vertical (flat features in $\boldsymbol{k}_{||}$ at a given $h\nu$) stripes in intensity correspond to higher harmonics of the selected photon energy directly exciting a core level. The monochromator filters wavelengths of light according to Bragg's Law and so multiples of wavelengths (photon

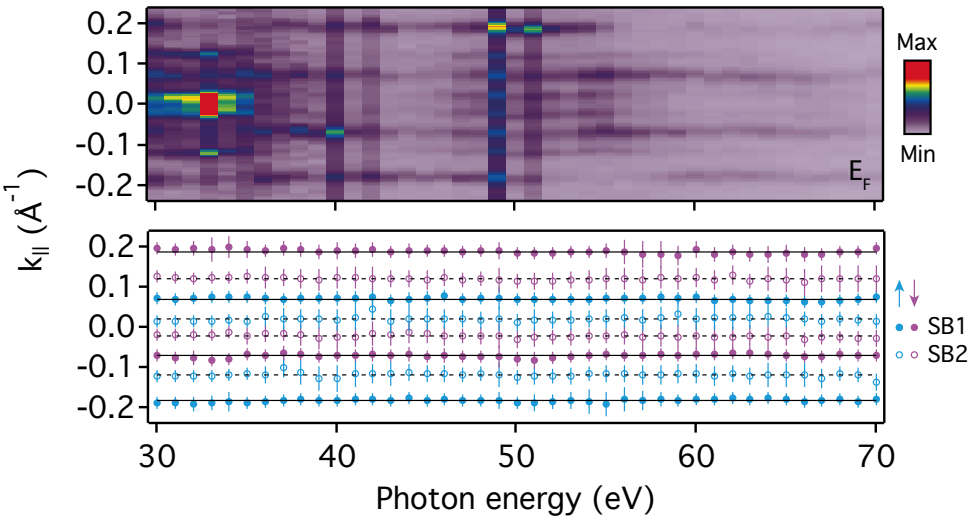

FIGURE 4.11: a) Photon energy dependent measurements of an MDC at the Fermi level of the QWS in BiTeI in the range $h\nu = 30 - 70$ eV using p-polarised light. b) The eight crossings corresponding to the two Rashba split subbands can be fit for a wide range of the data and their position is mostly constant over this range. The two pairs of vertical stripes correspond to higher harmonics exciting core levels directly.

energies) corresponding to higher orders are also incident on the sample (chapter 3). These typically only contribute diffuse background since there are usually no sharp, dispersive spectral features deep in binding energy. At some photon energies, these higher orders of light can excite directly a core level: the ejected core electron will have a kinetic energy coincident with a valence state electron excited by the lower order light, giving a flat (non-dispersive) spectral feature at the same kinetic energy as the valence states.

4.2.5 Resonant enhancements for atomic specificity

Further to providing information about the dimensionality, the photon energy dependent spectral weight can provide information about the atomic character of the underlying states, through resonant enhancements of spectral weight. Conventional ultraviolet photoemission spectroscopy (UPS) excites a system from a ground state (fig. 4.12ai) into a final state with a valence hole and a photoexcited valence electron (fig. 4.12aii). If an electron is

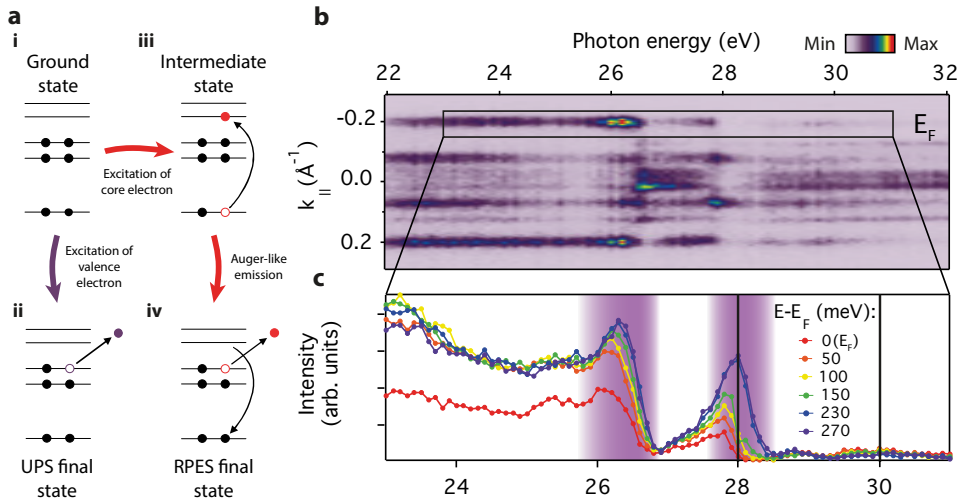

FIGURE 4.12: a) Schematic of two paths (ai-aii or ai-aiii-aiv) to the same final state via conventional UPS or resonant enhancements through Auger-like processes. b) Photon energy dependent measurements of an MDC at the Fermi level ($\pm 15\ meV$) of BiTeI in the range $h\nu = 22 - 32$ eV using p-polarised light along the $\bar{\Gamma}$-$\bar{\mathrm{M}}$-direction showing pronounced spectral weight variation. c) Intensity of the peak indicated by the box as a function of photon energy (corresponding to the outer band). The multiple traces show the binding energy dependent peaks in the spectral weight enhanced at the bismuth O-edge indicating a resonant enhancement. The two peaks correspond to the splitting of the Bi $5d$ spin-orbit doublet. Cartoon adapted from [95].

photoemitted from the Fermi level, $E_B = 0$, then the equation for the conservation of energy in the photoemission process (eq. 3.15) can be written as $E_k = h\nu - \phi$. Therefore the photoemitted electron at the Fermi level has a continuously tuneable energy, provided $h\nu > \phi$.

The photon energy can be tuned such that it coincides with the energy of a so-called absorption edge in the material, with an absorption threshold energy, E_0. This is defined as the energy at which core holes can be created within a particular electron shell (and so is closely related to the binding energy of that core shell). If the photon energy is tuned such that it coincides with the absorption threshold energy of a deeper lying core electron shell, a core electron can be excited to an unoccupied valence state, with energy E_m near the Fermi level (fig. 4.12aiii). In this case, the photon must supply an energy $h\nu = E_0 + E_m$.

Core hole lifetimes are short (by the uncertainty principle, due to their

larger energy than states near the Fermi level). The system will then relax back to the ground state which it can do in a vast number ways involving inelastic scattering of the electron, or emission of a photon or electron. The relaxation process which is relevant for resonant photoemission is that in which the excited electron can decay back into the core hole directly, simultaneously ejecting a valence electron in an Auger-like process (fig. 4.12aiii) [96]. This process leaves the system in a one-hole final state with an ejected valence electron, which is the same final state as with conventional UPS. The simultaneously emitted valence electron in this process receives the full energy of the excited electron in the relaxation back to the core hole. It therefore has an energy $E_k = E_m + E_0 - \phi = h\nu - \phi$, identical to the direct photoemission case. This process can result in a resonant enhancement of the photoemission intensity, through interference of these two final states (through direct and Auger-assisted photoemission). In particular, since this process involves bringing the photon energy into resonance with a core shell absorption energy, this resonant enhancement depends on the atomic species, providing element specific resonant enhancements. We exploit this in our measurements to gain atomic specificity. First we will approach how this occurs.

Including the resonance process, the photoemission intensity can be written as a sum of the direct photoemission pathway, with additional terms corresponding to the resonant pathway [96]:

$$I(E) = 2\pi \sum_f \left| \langle \Psi_f | V_r | \Psi_i \rangle + \sum_m \frac{\langle \Psi_f | V_A | \Psi_m \rangle \langle \Psi_m | V_r | \Psi_i \rangle}{E_i - E_m + i\Gamma_m/2} \right|^2 \delta(E_f - E_i) \quad (4.4)$$

where $|\Psi_i\rangle$, $|\Psi_m\rangle$, $|\Psi_f\rangle$ are the initial, intermediate and final states respectively with energies $E_{i,m,f}$. V_r denotes the radiative interaction, and V_A denotes the Auger decay interaction strength. The lifetime of the core-excited state $|\Psi_m\rangle$ provides a linewidth Γ_m.

Of these two pathways (the direct ionising pathway and the resonant Auger-assisted autoionising pathway), the direct pathway changes more slowly with photon energy than the resonant channel, which changes rapidly

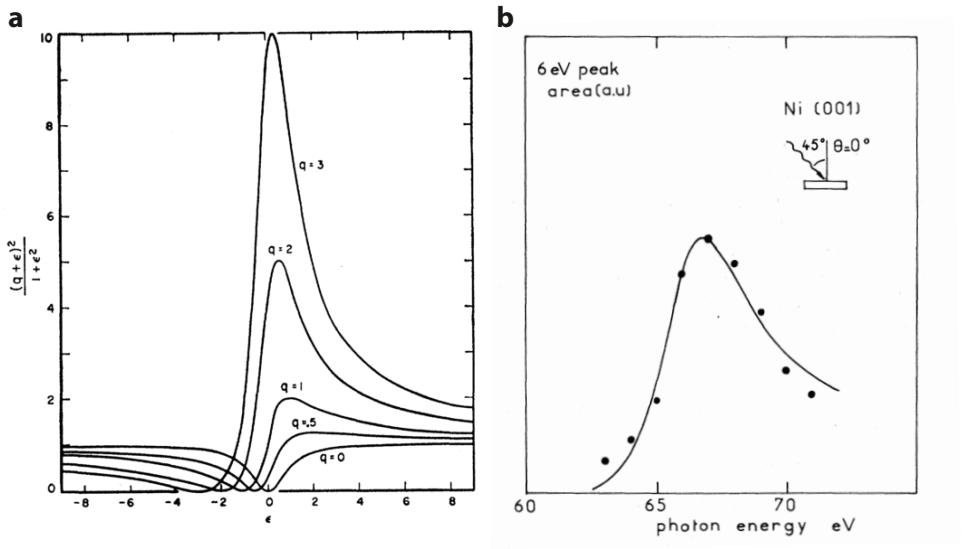

FIGURE 4.13: a) The Fano lineshape for various values of the asymmetry parameter, q. b) Early photoemission measurements showing a Fano resonance in nickel. (a) Reproduced from [97], (b) reproduced from [98].

as the photon energy is tuned through the resonance. The contributions to the photoemission intensity from the amplitudes of the transition matrix elements (eq. 4.4) for the different pathways interfere with different phases above and below the resonant energy. This constructive and destructive interference gives a characteristic asymmetric lineshape for the resonant enhancement in intensity. Asymmetric lineshapes of this nature were described by Fano in 1961, having the form [97]:

$$I = \frac{(q+\varepsilon)^2}{1+\varepsilon^2} \tag{4.5}$$

where ε is a reduced energy which is zero at the resonance energy, and q is a factor governing the asymmetry, proportional to the ratio of transition probabilities resulting from the two pathways [96]. The larger q value, the greater the effect of the resonance, and the sign of q indicates the phase of the resonance (i.e. being constructive or destructive, above or below the resonance energy) [99–101].

Figure 4.13a shows calculated Fano lineshapes for various strength asymmetries given by the value of q. Fano interference or resonant enhancements in intensity were first observed in photoemission for the metallic Ni(001)

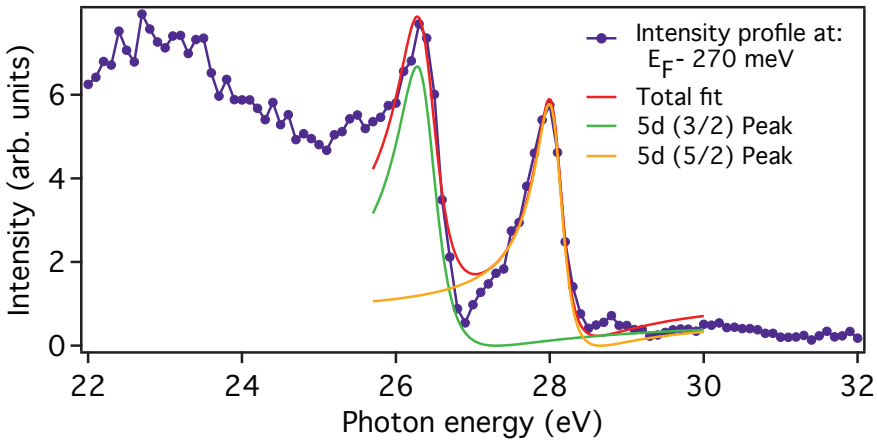

FIGURE 4.14: Example Fano fit to our resonant photoemission measurements on BiTeI. The trace shown is the lowest binding energy intensity profile over the range given in figure 4.12, for the negative $\boldsymbol{k}_{||}$ outer band. The two components arise from the spin-orbit doublet from the Bi $5d$ core level.

surface for a satellite peak in the photoemission spectra [98]. The intensity of this satellite feature as a function of photon energy was found to follow a Fano lineshape (fig. 4.13b) at photon energies corresponding to transitions from deeper lying $3p$ states to unoccupied near-Fermi level $3d$ states. In the case of the nickel surface, the two interfering pathways are:

$$3p^6 3d^9 4s + h\nu \rightarrow 3p^5 3d^{10} 4s \tag{4.6}$$

$$3p^5 3d^{10} 4s \leftrightarrow 3p^6 3d^8 4s + e^- \tag{4.7}$$

and

$$3p^6 3d^9 4s + h\nu \rightarrow 3p^6 3d^8 4s + e^- \tag{4.8}$$

where the first expression describes absorption of a photon producing the given intermediate state (eq. 4.6), and the second expression shows the Auger-assisted autoionisation process of an electron decaying back into the $3p$ level and ejecting a $3d$ electron (eq. 4.7). The final state given by equation 4.7 can be produced also through direct UPS, given in the third expression (eq. 4.8).

In our case, it is clear from figure 4.12 and figure 4.14 that we also observe

asymmetric peaks in intensity as a function of photon energy. These features occur around energies corresponding to the bismuth O-edge, comparable with the binding energy of the Bi $5d$ core level. We can then attribute these features to be a resonant enhancement of the bismuth derived states at this energy. Considering only the bismuth states, the two relevant interfering pathways are arising from:

$$5d^{10}6p^3 + h\nu \rightarrow 5d^9 6p^4 \tag{4.9}$$

$$5d^9 6p^4 \leftrightarrow 5d^{10}6p^2 + e^- \tag{4.10}$$

and

$$5d^{10}6p^3 + h\nu \rightarrow 5d^{10}6p^2 + e^-. \tag{4.11}$$

Further evidence for this is given by the fact that this effect increases approaching the band bottom, which is known to be more bismuth dominated, since there is less mixing of tellurium atomic character at the band bottom [70]. The extracted intensity profile has two peaks which are associated with the spin-orbit splitting of the $5d$ core level, so the $m_j = \frac{5}{2}$ peak is less deeply bound than the $m_j = \frac{3}{2}$ peak. We can fit the two peaks to Fano lineshapes and extract asymmetry parameters (shown for the deepest binding energy trace in figure 4.14) and in the region corresponding to the resonant enhancement this reproduces the measured intensity profile reasonably well. The total fit is a summation of the two Fano lineshapes with a global intensity scaling factor (a constant scaling factor used for both peaks). The dip in intensity is potentially then a result of the destructive interference from the Fano-like resonance.

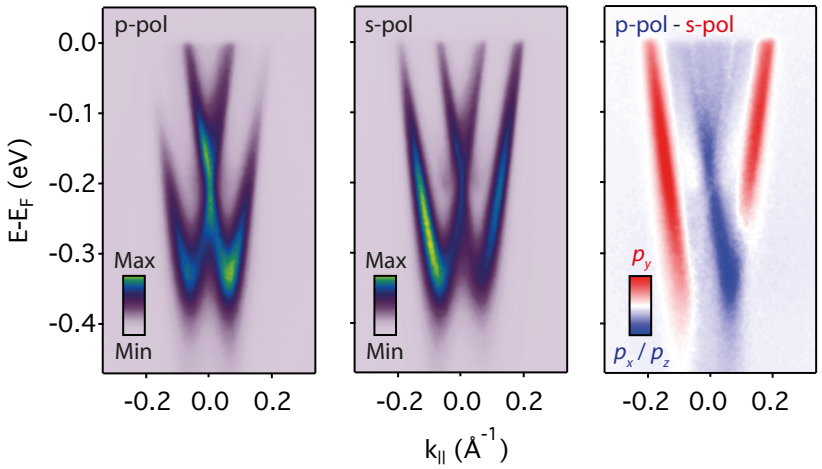

FIGURE 4.15: Polarisation-dependent ARPES of near-Fermi level states in BiTeI taken on resonance ($h\nu = 28$ eV). Differences in the spectral weight are predominantly due to the symmetry of the underlying orbital character.

4.3 Probing the orbital texture

4.3.1 Probing the orbital texture: Dispersion measurements

In this way we have shown we can control our measured spectral weight to resonantly enhance the bismuth derived character, gaining atomic specificity. The incoming light can not only be tuned to give us atomic sensitivity but also atomic-orbital sensitivity. This can be achieved through polarisation-dependent ARPES (described in Chapter 3). It was shown that the one-electron transition matrix element is non-vanishing when the parity eigenvalue of the light and of the initial state orbitals are the same. For linearly polarised light, and for p-orbitals (which make up the near-Fermi level states in BiTeI), p-polarised (s-polarised) light predominantly probes $p_{x,z}$ (p_y) orbitals (given the assumptions discussed in chapter 3).

Figure 4.15 shows three spectra of the conduction band states measured 'on resonance' with both linear polarisations, and the difference spectra. From now on, we define 'on resonance' as having $h\nu = 28$ eV, which coincides with the Bi O-edge, equivalently corresponding to the Bi $5d$ core-levels. Measurements taken in both linear light polarisations show the two Rashba split parabolae and there are hints of the second subband state (e.g.

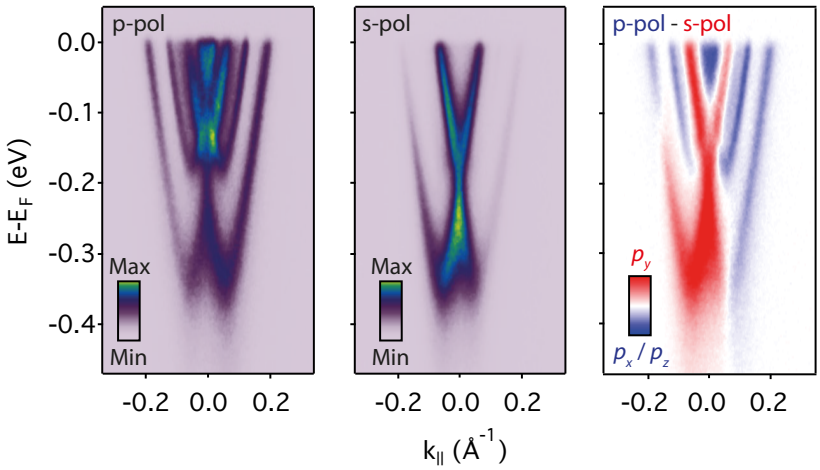

FIGURE 4.16: Linear polarisation-dependent ARPES of near-Fermi level states in BiTeI measured 'off resonance' ($h\nu = 30$ eV).

the band bottom $E_B \approx 200$ meV, similar to that extracted from our previous measurement).

The most striking difference is in the outer band. This has strong intensity towards the band bottom when probing with p-polarised light (fig. 4.15), which we can understand given the lowest energy states should be predominantly Bi p_z from band structure calculations and crystal field considerations [70]. The spectral weight of the outer band diminishes towards higher in-plane momentum, which corresponds also to lower binding energy (towards the Fermi level). This part of the outer band is much stronger when probing with s-polarised light, which is consistent with a greater mixing of the Bi in-plane p-orbitals (in this case highlighting the p_y component). This can be seen more clearly in the difference spectra.

Tuning the photon energy off resonance (see fig. 4.16), there is no longer a predominance of spectral weight from bismuth atomic character. At these low photon energies, the kinetic energy associated with a conduction band electron leads to a mean free path of $\lambda \sim 5$ Å, compared with a Te-Bi distance of 3.826 Å and Bi-I of 5.532 Å [59]. The exponential attenuation of the photoemission intensity into the bulk therefore gives us a generically greater sensitivity to tellurium atomic character at the tellurium terminated surface. By the Beer-Lambert law for photoemission, close to normal

emission, this reduces the photoemission intensity from bismuth atoms by $\sim e^{-d/\lambda} = 0.46I_0$ and for iodine by $0.15I_0$. In addition, the photoionisation cross-section for tellurium compared with bismuth at these energies is $\sigma_{Te}/\sigma_{Bi} = \frac{1.369}{0.8964} = 1.538$ [102]. These effects should give a stronger contribution from tellurium derived states, but the strong spin-orbit coupling makes the wavefunction a mixture of contributions from all the relevant atomic orbitals, which in this case is predominantly Te $5p$ and Bi $6p$ [70].

This can partly be seen in the off resonance dispersion measurements (fig. 4.16). The spectral weight distribution for both p- and s-polarisation is very different to the on-resonance equivalents. For the dispersion measured with p-polarised light, the spectral weight is shifted away from the band bottom and is shifted additionally to the inner band. Measuring using s-polarised light, the spectral weight is shifted almost completely from the outer band to the inner band. This implies there is a greater contribution from p_y orbitals of the inner band to the spectral weight at this energy. By the arguments above, and given that now the condition for resonance is not satisfied, this could be attributed to a contribution from the tellurium atomic orbital character (but further analysis to come will strengthen this assignment).

4.3.2 Probing the orbital texture: Constant energy contour measurements

The orbital composition of the bands can be determined perhaps most clearly from constant energy surface (CES) showing the full in-plane momentum dispersion (k_x-k_y) of the conduction band states. The dispersions were measured in a geometry where the analyser slit is defined as being along k_y (fig. 4.17c). Figure 4.17 shows constant energy surfaces at various points in binding energy for the conduction band states. These have been measured with the photon energy tuned on resonance ($h\nu = 28$ eV) and using s-polarised light, so spectral weight can be considered predominantly Bi p_y derived. For simplicity we define a variable α which is the azimuthal angle measured clockwise from the positive k_y direction as in figure 4.17.

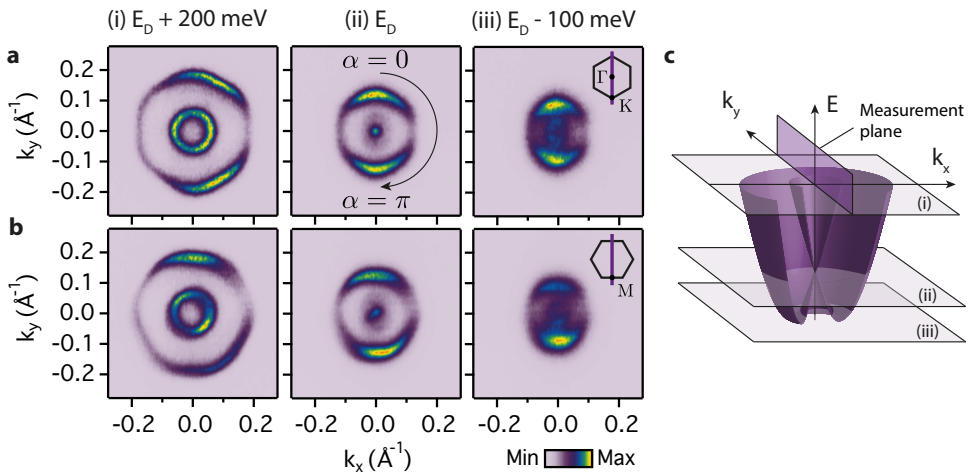

FIGURE 4.17: Constant energy surfaces measured using s-polarised light, on resonance ($h\nu = 28$ eV), for the conduction band states in BiTeI. Measured along (a) $\bar{\Gamma}$-$\bar{\mathrm{K}}$, and (b) $\bar{\Gamma}$-$\bar{\mathrm{M}}$, at binding energies corresponding to (i) the Fermi level, (ii) the Dirac point, and (iii) close to the band bottom, as in the schematic (c).

Focussing first on the outer band, there is a clear peak in the spectral weight at positive and negative k_y for $k_x = 0$ (i.e. $\alpha = 0,\ \pi$) of this contour. This peak is seen most clearly for the CES measured along $\bar{\Gamma}$-$\bar{\mathrm{K}}$ at the Dirac point (fig. 4.17aii), but a similar spectral weight distribution can be seen for the outer band for all CESs in figure 4.17. When measuring using s-polarised light, the spectral weight in this case should predominantly be derived from p_y orbitals. Peaks in the spectral weight therefore indicate a greater p_y orbital character, under these conditions. The azimuthal distribution of the spectral weight for the outer band in figure 4.17a suggests p_y orbital character at the 'top' and the 'bottom' of the band (or $\alpha = 0, \pi$). They are therefore radially aligned to the constant energy contour (fig. 4.18b). In addition, the suppression of spectral weight at positive and negative k_x for $k_y = 0$ (i.e $\alpha = \pi/2,\ 3\pi/2$) for the outer band could suggest a lack of p_y orbital character at this point.

There could be other geometrical, interference or final state matrix element contributions which could explain this, without requiring a suppression of p_y orbital character. One test is to rotate the sample azimuthally. If the spectral weight is unchanged then it suggests an ordering of the orbitals to the band contours which is rotationally symmetric in the lab frame. We

rotate our sample azimuthally such that the measurement plane (along the lab k_y direction) lies along the $\bar{\Gamma}$-$\bar{\mathrm{M}}$ crystallographic direction (fig. 4.17b). The spectral weight distribution is qualitatively unchanged, with peaks in the spectral weight on the outer band at the top and the bottom or $\alpha = 0,\ \pi$ (fig. 4.17b). If this state was predominantly derived from p_y orbital character and the spectral weight suppression was purely a geometrical effect, then rotating the sample will have changed the azimuthal distribution of the spectral weight. Clearly this is not the case. Leaving the spectral weight unchanged could be an indication that the suppression in spectral weight is coming from a predominantly p_x derived orbital character at the 'left' and 'right' of the outer band or $\alpha = \pi/2,\ 3\pi/2$ (fig. 4.18c). This kind of ordering of the orbitals around the contour would then be unchanged under rotation. There is then an ordering of the orbitals with the momentum directions, in a similar sense to spin-momentum locking. This is most evident closer to the Dirac point for contours with smaller in-plane momentum but there are apparent deviations from the simplest picture as the in-plane momentum of the contour is increased and the spectral weight distribution is correspondingly more complicated. Potential reasons for this will be discussed in this chapter but for now we will discuss the simplest underlying principle of the orbital ordering and later discuss reasons for departures and possible avenues for further understanding.

Focussing now on the inner band, at the Fermi level (fig. 4.17ai), the azimuthal spectral weight distribution is switched compared with the outer band. Here the spectral weight has peaks at $\alpha = \pi/2,\ 3\pi/2$ of the inner band, and is suppressed towards $\alpha = 0,\ \pi$. Probing with s-polarised light, peaks in the spectral weight should therefore indicate a predominance of p_y orbital character. There should therefore be a tangential alignment of p_y orbitals to the inner band at the Fermi level (fig. 4.18b,c). We can get a qualitative understanding of how this evolves by comparing against the other constant energy contours (fig. 4.17a). Precisely at the Dirac point, the inner band collapses to a point in k_x-k_y with no azimuthal dependence to the spectral weight by definition. Consider below the Dirac point, deeper in binding

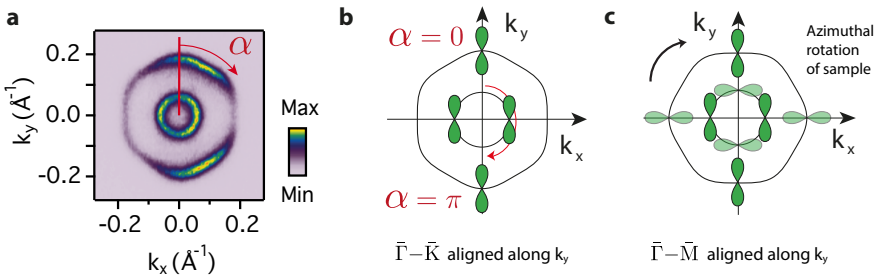

FIGURE 4.18: a) Fermi surface measured using s-polarised light, on resonance ($h\nu = 28$ eV), analyser slit aligned along $\bar{\Gamma}$-$\bar{K}$ (from fig. 4.17). b) Schematic of p_y orbital orientation and distribution, for the Fermi surface measurement shown. This azimuthal distribution of spectral weight indicates a radial orientation of p_y orbitals on the outer band, and a tangential orientation on the inner band. c) Rotating the sample crystallographic axes to the lab frame. Unchanged azimuthal distribution of spectral weight under azimuthal rotation is evidence for this ordering of the orbitals with respect to the band contour.

energy, towards the band bottom (fig. 4.17aiii). The inner band is visible inside the outer band as expected, and a suppression of the spectral weight is observed at $\alpha = \pi/2,\ 3\pi/2$ of the band, both for the inner and outer band. Together this suggests that the Bi p orbitals are aligned tangentially to the inner band above the Dirac point, and radially, below the Dirac point. The orbital alignment is also continuous at the band bottom, evolving smoothly from the inner to outer band. Again, this is so far assuming the simplest possible scenario: clearly there are some deviations from the simple picture that the spectral weight is distributed symmetrically at the top and bottom or left and right of a contour, especially further away from the Dirac point.

This orbital polarisation is reminiscent of recent work performed on topological insulator surface states [103] (fig. 4.19). Linearly polarised light and spectral weight analysis has been used to map the orbital part of the wavefunction in Bi_2Se_3, where the orbital texture was found to be radial (tangential) below (above) the Dirac point [103, 104] (fig. 4.19), consistent with our findings for BiTeI. In Bi_2Se_3, the orbital polarisation was initially described as potentially arising due to the topological physics [104]. Our work is the first confirmation that this effect exists in a completely different material, with none of the topological physics convoluting the interpretation. Here,

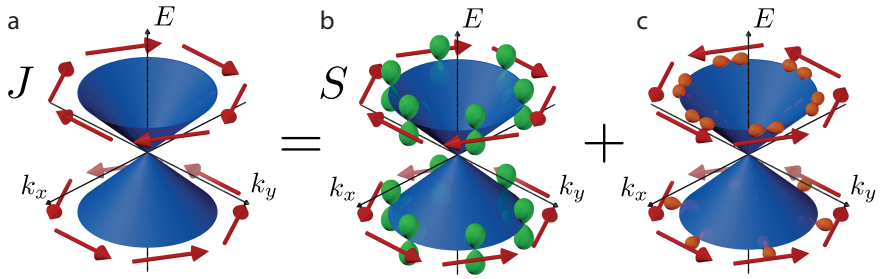

FIGURE 4.19: Orbital polarisation and associated spin texture in Bi_2Se_3. a) Total angular momentum $\boldsymbol{J} = \boldsymbol{L} + \boldsymbol{S}$, driving a chiral spin texture switching through the Dirac point. b) Isotropically distributed p_z derived orbitals. These drive a chiral spin texture $\boldsymbol{S}$ that switches at the Dirac point. c) In-plane $p_{x,y}$ orbitals showing tangential orbital texture above and radial orbital texture below the Dirac point. These should drive a spin texture that does not switch through the Dirac point, showing a complex coupled spin-orbital texture in Bi_2Se_3. Adapted from [103].

since BiTeI is a material with strong spin-orbit coupling and is a topologically trivial analogue to Bi_2Se_3, we demonstrate through our work that orbital polarisation is a generic consequence of the spin-orbit interaction alone.

Our experimental results presented so far have focussed primarily on the Bi p_y orbital character, however the bands are derived from a mixture of bismuth and chalcogen orbitals, as well as each component of p orbitals, $p_{x,y,z}$. In fact it was found that each orbital component, $p_{x,y,z}$, drives a particular spin component through spin-orbit coupling. The momentum-dependent orbital texture then drives a momentum-dependent spin texture resulting in a coupled spin-orbital texture (which will be discussed in detail for this material later). In Bi_2Se_3, this leads to a spin texture that not only switches about the Dirac point, but additionally depending on the atomic species and orbital character probed, i.e. an atomic orbital dependent spin texture (fig. 4.19). Later in this chapter, we will discuss the relevant work in detail, and show through calculations and spin-ARPES how this arises in BiTeI.

For the off resonance k_x-k_y CESs in BiTeI, the spectral weight now has peaks at the top and the bottom of the band ($\alpha = 0,\ \pi$) for both the outer and inner bands at the Fermi level, above the Dirac point (fig. 4.20). The spectral weight is strongest for the inner band, which is consistent with the dispersions in figure 4.16 (note again that the analyser slit is aligned along

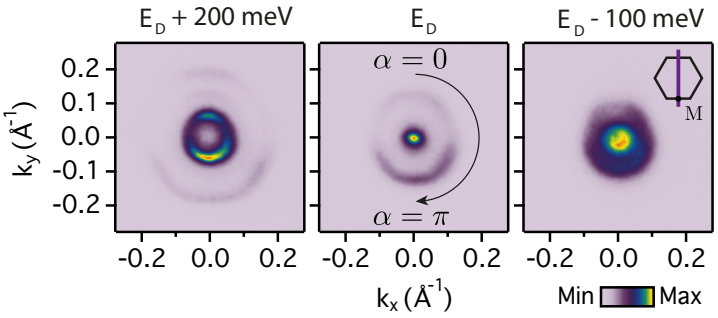

FIGURE 4.20: Constant energy surfaces measured using s-polarised light, off resonance ($h\nu = 30$ eV), for conduction band states in BiTeI. Measured along $\bar{\Gamma} - \bar{\mathrm{M}}$ at binding energies corresponding to (i) the Fermi level, (ii) the Dirac point, and (iii) close to the band bottom.

the k_y direction). With the resonance condition relaxed, the spectral weight contains contributions from the total wavefunction, potentially favouring tellurium atomic orbitals by the arguments outlined previously. This would suggest a complete anti-alignment of the tellurium orbital texture with the bismuth orbital texture from our measurements.

In Bi_2Se_3, calculations suggest the orbital texture to be intricately linked to a given layer within its quintuple layer unit cell (in turn corresponding to a particular atomic character), suggesting a layer-entanglement of the wavefunction [105] (this and other convoluting factors will be discussed later this chapter). Our conclusions from the off resonance k_x-k_y maps are the first experimental evidence this layer-entangled coupled spin-orbital texture exists, supported by DFT calculations to follow. In addition, our work is proof that this physics is purely a consequence of spin-orbit coupling and exists beyond topological materials.

The procedure for quantifying the degree of orbital polarisation, and its evolution through the Dirac point, is summarised in figure 4.21. The k_x-k_y maps can be 'unwrapped' by taking a series of azimuthal line profiles and plotting the spectral weight as a function of azimuth (fig. 4.21). The red line in fig. 4.21a corresponds to $\alpha = 0$, and positive α rotates clockwise. The intensity and the position of the peaks can then be easily extracted. The normalised intensity is shown as a function of azimuthal angle for a series of binding energies over the full bandwidth of the inner band, from the Fermi

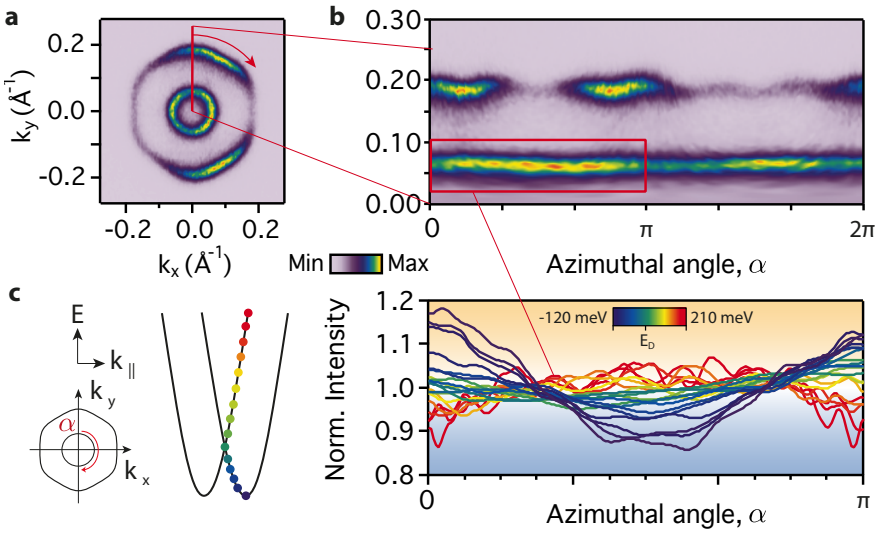

FIGURE 4.21: Extracting the spectral weight around the inner band on resonance. a) Example k_x-k_y map (at E_F) showing direction of azimuthal profiles. b) Azimuthal profile for the map in (a) plotted linearly. c) Normalised intensity extracted for the full bandwidth of the inner band as a function of azimuth. The intensity curvature changes sign through the Dirac point.

level (red), to the CBM (violet). Above (below) the Dirac point for the inner band, the spectral weight is peaked at $\alpha = \pi/2$ ($\alpha = 0,\ \pi$) consistent with our assignment of radially (tangentially) aligned orbitals.

We can extract an angular distribution factor (ADF), $\lambda(\omega)$, from the traces as a function of binding energy defined in the following way:

$$\lambda(\omega) = \frac{I_{\alpha=\pi/2}(\omega) - I_{\alpha=0,\ \pi}(\omega)}{I_{\alpha=\pi/2}(\omega) + I_{\alpha=0,\ \pi}(\omega)} \tag{4.12}$$

where $I_\alpha(w)$ is the spectral weight at azimuthal angle α and energy ω. This factor is the experimental equivalent of the 'orbital polarisation ratio' determined from the first principles calculations in Cao *et al.* [104]. In their OPR, since this is obtained from first principles calculations, they are able to consider individual azimuthal cuts at $\alpha = 0,\ \pi/2,\ \pi$ and the OPR is robust. Our ADF however is obtained from experimental measurements and the spectral weight variations are less smooth, and are sensitive to noise. To compensate we integrate around the values $\alpha = 0,\ \pi/2,\ \pi$ with a width of $\sim 0.03\pi$. The obtained ADF was reasonably robust to greater integration windows. The

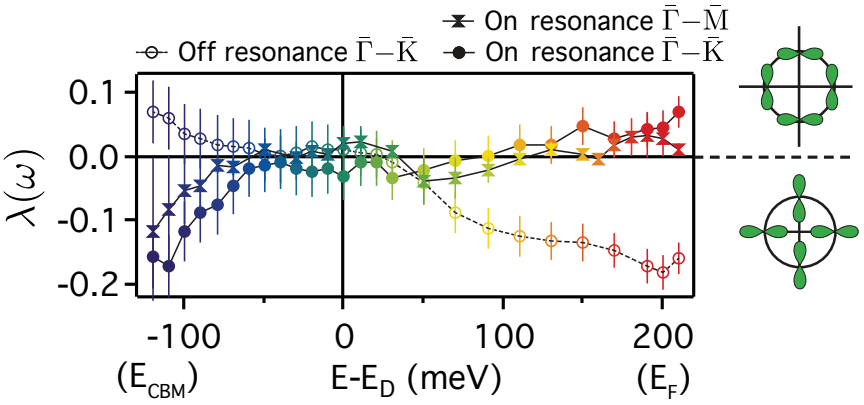

FIGURE 4.22: The angular distribution factor $\lambda(w)$ (eq. 4.12) plotted for the inner band on and off resonance (for a k_x-k_y measurement with the analyser slit aligned along $\bar{\Gamma}$-$\bar{K}$), and on resonance (for a k_x-k_y measurement with the analyser slit aligned along $\bar{\Gamma}$-$\bar{M}$). Positive $\lambda(w)$ indicates tangentially aligned orbitals, negative indicates radially aligned orbitals.

results are shown in figure 4.22. The ADF is defined such that a positive $\lambda(\omega)$ (top half of fig. 4.22) corresponds to tangentially aligned orbitals, and a negative (bottom half of fig. 4.22) corresponds to radial alignment. The results are consistent with our assignment for both $\bar{\Gamma}$-$\bar{K}$ and $\bar{\Gamma}$-$\bar{M}$ alignment on resonance, with an ADF which goes through zero at the Dirac point and is broadly negative at the band bottom. Qualitatively this agrees with what is seen for the topological insulator surface states [104].

Calculating the ADF for the inner band off resonance the trend is completely reversed, but still switches precisely at the Dirac point. This is further evidence that not only is the orbital polarisation tied to a particular eigenstate of the system, switching precisely at the Dirac point, but that this is also intricately linked to the atomic character, changing sign as we probe off resonance.

4.3.3 Confirming the orbital texture: DFT calculations

The spectral weight from ARPES measurements is clearly a reasonable indicator of the orbital character but we are of course not directly looking

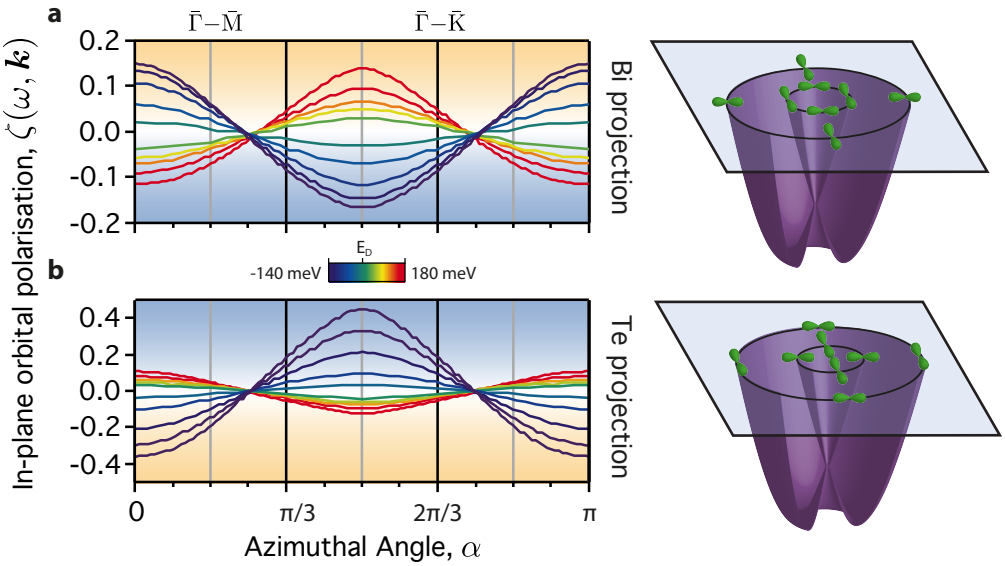

FIGURE 4.23: In-plane orbital polarisation ratio $\zeta(\omega, \boldsymbol{k})$ of the inner band extracted for (a) Bi and (b) Te atoms. Positive (negative) ζ denotes greater density of p_y (p_x) orbital character showing opposite alignment of orbitals between Bi and Te (shown in the cartoons).

at initial state orbitals. We can compare our measurements to density functional theory (DFT) calculations which represent the initial state atomic orbital character. DFT calculations have been performed by our collaborator Choong H. Kim at Cornell University for this compound. Full details of the calculations can be found in our paper underpinning this chapter [106]. The calculations include the spin-orbit interaction and consider 60 atomic layers plus 20 Å of vacuum to model a Te-terminated surface to compare with our measurements. We were provided with the magnitude of the complex coefficients (atomic orbital weights) for all components of: p-orbital weight, OAM and vectorial spin; projected onto the first six layers (two Te-Bi-I trilayers), as a function of energy and in-plane momentum.

To compare most directly to our measurements, we can calculate an in-plane orbital polarisation ratio:

$$\zeta(\omega, \boldsymbol{k}) = \frac{I_{p_y}(\omega, \boldsymbol{k}) - I_{p_x}(\omega, \boldsymbol{k})}{I_{p_x}(\omega, \boldsymbol{k}) + I_{p_y}(\omega, \boldsymbol{k})} \tag{4.13}$$

where $I_{p_x,y}(\omega, \boldsymbol{k})$ is the weight of a particular orbital component at energy and in-plane momentum $(\omega, \boldsymbol{k})$. Positive (negative) values of ζ therefore

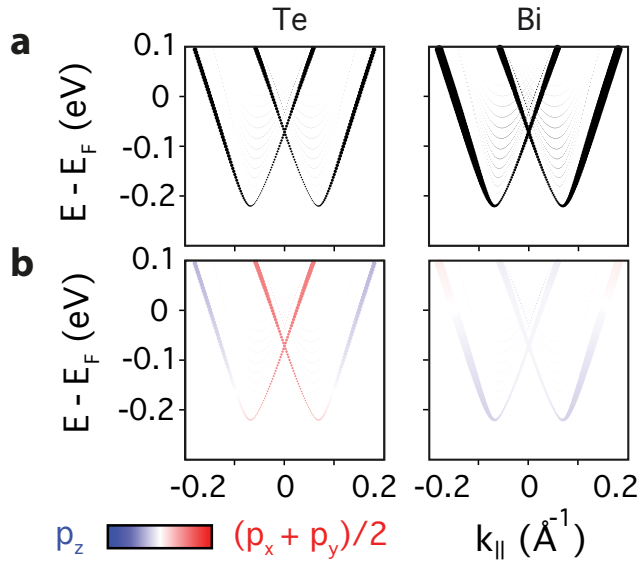

FIGURE 4.24: a) Total atomic orbital weight distribution for the conduction band state in BiTeI projected onto Te and Bi. b) The in-plane vs out-of-plane orbital contribution to the conduction band state in BiTeI for Te and Bi. The CBM is slightly more Bi p_z dominated. The inner band at the Fermi level has a greater contribution from in-plane p orbitals.

denote a greater weight of p_y (p_x) orbital character. We compute this value for the inner band for the Bi projections and Te projections. The results are shown in figure 4.23 for values of $\alpha = 0$-π in direct analogy to our extracted spectral weight (fig. 4.21c). For the Bi projection, the OPR matches well with our spectral weight extraction performed on resonance.

There is a clear peak in the spectral weight at the Fermi level for the inner band at $\alpha = \pi/2$ and this smoothly evolves to the band bottom, confirming our assignment of tangential (radial) above (below) the Dirac point for bismuth, increasing in strength away from the Dirac point. This assignment was the more robust from experiments, since we employed resonance enhancements to gain additional sensitivity to bismuth atomic orbital character.

Intriguingly, the tellurium atomic orbital character projected from DFT is exactly the opposite alignment to the bismuth character. This supports our conclusion from the ADF extracted for the inner band off resonance (fig. 4.22). This is additionally supported by the relative weight of in-plane orbitals to out-of-plane orbitals for the tellurium layer, showing a greater

weight of in-plane orbitals for the inner band (fig. 4.24b). For the bismuth layer, there is a slight increase in p_z orbital character towards the band bottom but at the Fermi level there is an otherwise roughly equal admixture of in- and out-of-plane (fig. 4.24b). This provides some explanation as to why in our off resonance k_x-k_y map (fig. 4.20b), the inner band spectral weight appears to reflect the tellurium orbital character, whereas the outer band appears more bismuth-like.

4.4 Revealing the coupled spin-orbital texture

4.4.1 DFT calculations

The spin-orbit interaction in BiTeI is shown to result in a complex orbital texture with contributions from the different atomic layers within the compound, beyond what is expected from the Rashba Hamiltonian. We can in fact show from our calculations and ARPES measurements that these orbital textures drive a hierarchy of coupled spin-orbital textures tied to a particular layer and atomic orbital.

A typical Rashba spin-split state would exhibit an in-plane chiral spin texture, counter propagating for the two Fermi surfaces as discussed. The vectorial spin arising from the out-of-plane Bi p_z orbitals shows predominantly the typical in-plane Rashba-like spin texture. This is reinforced to some extent on the outer-band by the tellurium atomic character, which shows the same Rashba-like spin texture but with a weak contribution to the inner band (fig. 4.25c,d).

Considering the spin texture arising from the in-plane p-orbitals, there are clearly significant departures from Rashba-like spin-splitting, with spin textures that are not circulatory for the in-plane spin projection. The schematics (fig. 4.25d) depict the contributions from each Fermi surface to the in-plane spin texture, accounting for the strength of the contribution of a particular in-plane orbital component at a given $\boldsymbol{k}$. This is in analogy to the schematic in figure 4.19. In BiTeI, the Bi p_x orbital weight on the outer band is strongest at the left and right of the band (i.e. at $\boldsymbol{k}_{||} = (\pm k_x, 0)$, or $\alpha = 0, \pi$),

as discussed from our ARPES measurements and DFT calculations. The spin-projection from Bi p_x orbitals at these $\boldsymbol{k}$-points is tangential and clockwise, i.e mostly $\pm S_y$ for $(\mp k_x, 0)$ (fig. 4.25a). Conversely, the top and bottom of the outer band is more predominantly p_y orbital character, however this also drives a clockwise vectorial spin (fig. 4.25b). This is summarised in figure 4.25d, which for the Bi in-plane spin is then clockwise on the outer band. For the inner band, we have shown that the orbital polarisation is switched compared with the outer band. This means the Bi p_x orbital weight on the inner band is strongest at the top and bottom (i.e. $\boldsymbol{k}_{||} = (\pm k_x, 0)$), and more p_y orbital character dominated at the left and right of the inner band ($\boldsymbol{k}_{||} = (0, \pm k_y)$). The corresponding spin texture driven by this tangential alignment of in-plane orbitals is then also clockwise, meaning both the inner and outer band have the same chirality spin texture projected from in-plane orbitals (fig. 4.25d). Applying similar arguments we can obtain a schematic for the inner and outer band for Bi and Te character, for the in-plane spin arising from both in-plane and out-of-plane orbitals. The in-plane spin texture arising from $p_{x,y}$ and p_z orbitals is then fully summarised for clarity in the respective schematics in figure 4.25d.

For the in-plane spin arising from the out-of-plane orbitals, both Bi and Te p_z orbitals drive a counter-propagating in-plane spin texture, typical for the Rashba model. The in-plane spin arising from in-plane orbitals however, for both Bi and Te, is not counter-propagating, which seems to be a departure from the typical Rashba model. The total spin in this system will be a combination of all contributions from in-plane orbitals and out-of-plane orbitals of each of the constituent atoms however, which overall reduces to that expected from a conventional Rashba model. Our measurements and calculations however reveal that this overall conventional Rashba spin texture is a complex hierarchy of the spin texture driven by a particular orbital component, for each of the present atomic species. Additionally, since these spin textures are driven by a particular orbital component, these non-Rashba-like spin textures are a result purely of the orbital polarisation within the system. Therefore the orbital polarisation vanishing

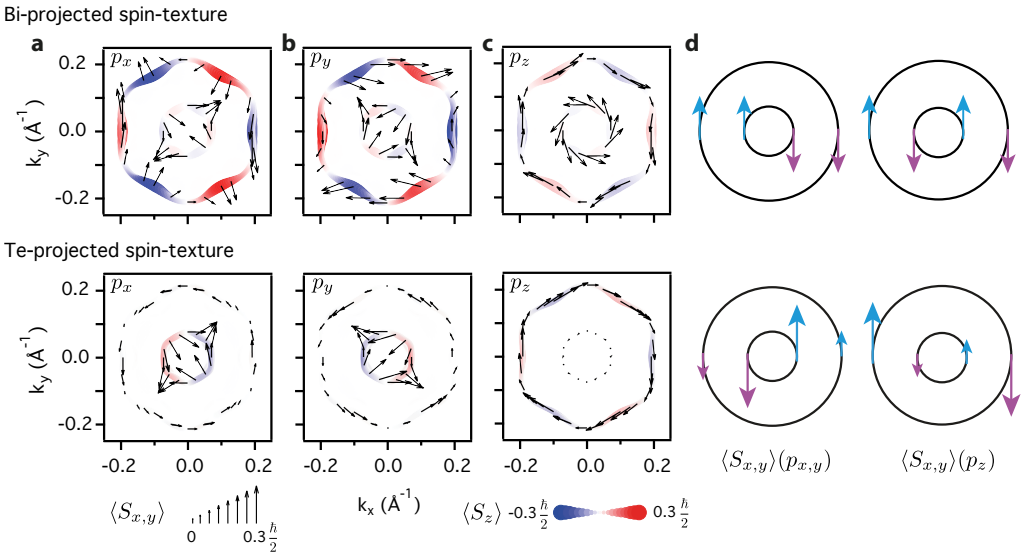

FIGURE 4.25: DFT projected coupled spin-orbital texture for Bi and Te arising from (a) p_x, (b) p_y and (c) p_z orbitals. The black arrows denote the in-plane spin texture, while the colour denotes the out-of-plane spin texture. The in-plane spin texture arising from in-plane vs out-of-plane orbitals is shown schematically in (d). There are clearly signs of a non-Rashba-like in-plane spin texture arising from the in-plane orbitals, as well as a canting of the spin out of the surface plane.

at the Kramer's degenerate point follows simply from the requirement that the spin must be degenerate at this point, required by time-reversal symmetry.

These in-plane coupled spin-orbital textures are well in accordance with the calculated orbitally-projected spin textures in topological insulator surface states [105, 107]. Similarly for the TI surface state (TSS), a chiral in-plane spin texture is expected, but the spin-projection from the different orbital components shows a departure from a simple tangential alignment to the constant energy contours.

4.4.2 Spin-ARPES

This effect is actually measurable through polarisation-dependent spin-ARPES. Several groups now have measured, for the TSS in Bi_2Se_3, the tangential component of the in-plane spin to completely reverse when probing with s- vs p-polarised light [103, 108–110], attributed to the orbital-selectivity of linearly-polarised light. This orbital-selective spin reversal was

not seen for the Rashba-split surface state of Au(111) by Jozwiak *et al.*, despite it presumably being present, which they attribute to the reduced spin-orbit strength of this material [108].

Significantly, in 2016, following our polarisation dependent study of BiTeI, a polarisation-dependent spin-ARPES study by Maaß *et al.* measured the spin texture of the Rashba split bands in BiTeI using a $h\nu = 6$ eV laser and spin-filter [111]. They show that the measured spin indeed switches sign when probing with s- vs p-polarised light from their spin-resolved k_x-k_y maps [111]. They attribute this to the orbitally-resolved spin texture which they confirm with calculations, in good agreement with the coupled-spin-orbital texture picture presented in our work.

We have performed similar spin-ARPES measurements ourselves, this time at a synchrotron where the photon energy can be changed in addition to the polarisation. This allows us to tune the photon energy on resonance and measure the spin polarisation with s- and p-polarised light. The results are shown in figure 4.26. The magenta traces in the spin-polarisation EDCs (fig. 4.26b) denote the in-plane component of the spin (along the analyser slit direction) which at this point in the Brillouin zone should be non-zero for a Rashba spin-split band. For s-polarised light, the in-plane polarisation is broadly positive below the Dirac point and negative above the Dirac point, producing the counter-propagating spin texture expected for the Rashba model. The high noise above the Fermi level is caused by the normalisation process since these are very small absolute values above the Fermi level. The spin-polarisation when probing with p-polarised light is then qualitatively opposite to that obtained with s-polarised light (fig. 4.26b,c). This is also evident from the true-spin EDCs (accounting for efficiency of spin-detection, eq. 3.21). The highest binding energy peak when probing with p-polarised light is opposite sign to the highest binding energy peak when probing with s-polarised light (fig. 4.26c). This is can be explained by the orbital selectivity of the light polarisation coupling to the in-plane spin texture of the $p_{x,z}$ or p_y orbitals for p- or s-polarised light respectively, which is experimentally verified by Maaß *et al.* [111]. Our measurements are not completely

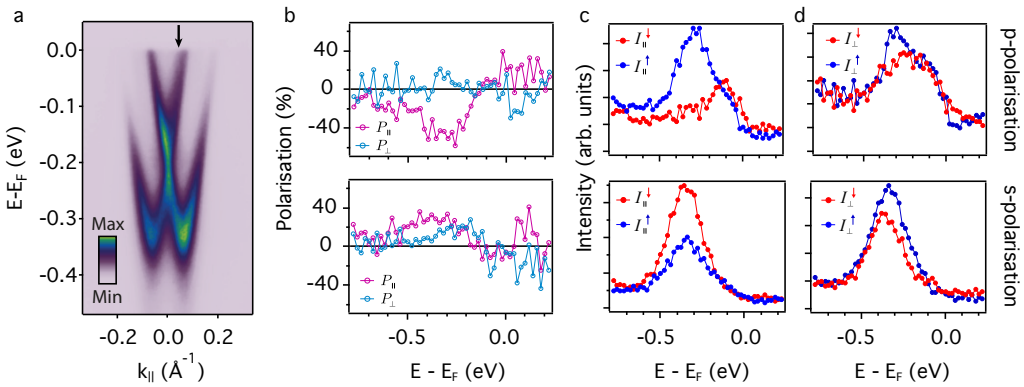

FIGURE 4.26: Spin-resolved ARPES measurements using s- and p- polarised light measured on resonance ($h\nu = 28$ eV). The analyser slit was approximately aligned along $\bar{\Gamma}$-$\bar{K}$ and the spin-EDC was measured at an in-plane momentum corresponding to the arrow in the example dispersion (a). b) Spin-polarisation EDCs and true spin EDCs are shown for the s- and p-polarised light, for c) the in-plane (along the analyser slit) and d) the out-of-plane components of spin.

independently convincing, but taken with our the conventional ARPES, our DFT and the spin-ARPES of Maaß *et al.*, they provide at least some further support that the orbital polarisation is the likely underlying principle.

We measure also a non-negligible out-of-plane component of the spin, evident in the spin-polarisation measured with s-polarised light (fig. 4.26b) and the true spin EDC (fig. 4.26d). When probing with p-polarised light the out-of-plane spin-polarisation is mostly zero, however there is a small peak when probing with s-polarised light. There is additionally a peak in the true-spin, which is not degenerate for the red and blue traces, when probing with s-polarised light. We can rule out this being an artefact of the geometry of the experimental set up, and we know s-polarised light should couple to p_y orbitals, which our DFT shows can drive an out-of-plane spin-polarisation along this direction. This measurement provides experimental evidence then for a small out-of-plane spin-canting, where the in-plane chiral spin texture is modulated additionally by a non-zero S_z component. This would need further experiments to fully map and understand this canting however.

The canting of the spin out of the surface plane (a non-zero S_z component) is known to exist, by calculations and by direct S_z measurements using

spin-ARPES, in this compound [57, 111] and topological insulator surface states [91, 107, 112, 113]. This is seen clearly in our calculations (fig. 4.25) and has a similar dependence on the relative atomic orbital weight as with the in-plane spin. The out-of-plane spin arises most strongly from the in-plane atomic orbitals, evident from our Bi-projected spin texture. This is supported for example by the lack of out-of-plane spin component arising from the tellurium atoms on the outer band (fig. 4.25).

4.4.3 Circular dirchroism

While spin-ARPES provides a more direct probe of the spin-resolved band structure, the process itself is inherently inefficient, particularly also since the data typically obtained is 1D. This is because spin-ARPES requires first angle and energy resolving the electrons, before then resolving the spin-up and spin-down electrons. The process can be made significantly more efficient if any information even indirectly could be obtained from the 2D detector. Efforts towards this have been made in understanding the difference spectra between photoemission measurements obtained using circularly left and circularly right polarised light. This is termed circular dichroism (CD).

Circularly polarised light carries an angular momentum, and it has been shown to be sensitive to an unquenched orbital angular momentum (OAM) within the electronic structure, a generic consequence of inversion symmetry breaking [114, 115]. It is also shown that in materials with strong spin-orbit interactions, the orbital angular momentum (OAM) tends to anti-align itself with the spin-angular momentum (SAM), providing an indirect route to probing the underlying spin texture. CD measurements often seem to show modulations of the CD sign around a band that are consistent with modulations in the calculated 3D spin texture [116, 117]. In particular, CD has been shown to be an effective probe of the out-of-plane component of OAM, which appears as a sign change in the CD between time reversal points (equivalently, a 3-fold rotational symmetry around a band in k_x-k_y) consistent with the calculated out-of-plane spin-canting [113, 116, 117]. At lower binding energies, or equivalently smaller in-plane momentum away

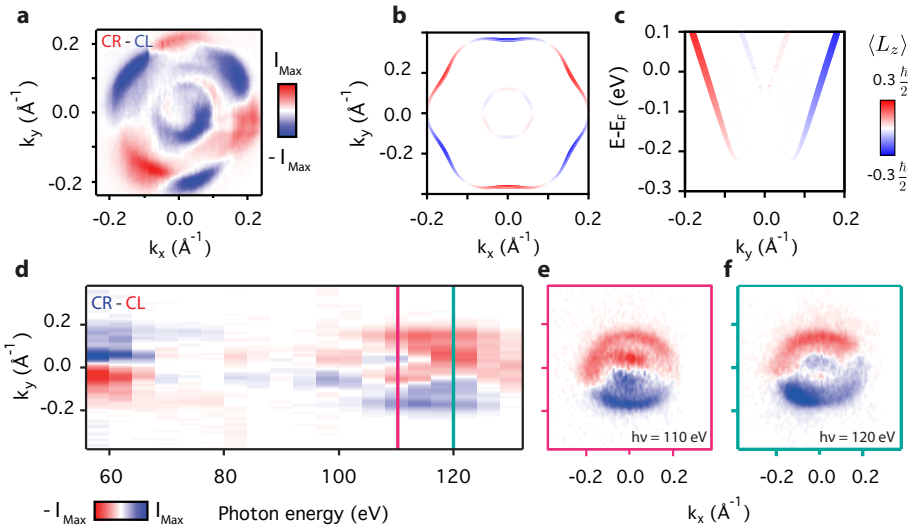

FIGURE 4.27: a) CD at E_F measured on resonance ($hv = 28$ eV). b) L_z projection onto the Bi layer at $E = 0.1$ eV. c) L_z projection onto the Bi layer for the band dispersion. L_z goes to zero as in-plane momentum decreases. d) CD as a function of photon energy showing multiple switches of sign which can be seen clearly from the k_x-k_y maps at (e) $hv = 110$ eV and (f) $hv = 120$ eV

from the Γ point, instead of a $\sin(3\alpha)$ modulation of the intensity around the band, a $\sin(\alpha)$ modulation is expected [113, 116, 117].

Figure 4.27 details some of our CD measurements on BiTeI. There is a clear 3-fold modulation of the CD signal (fig. 4.27a) consistent with previous results on TI surface states, explainable by the pronounced hexagonal warping. At this higher warping, the spin is canted out of the surface plane and so the OAM, which is directly opposite in these strong spin-orbit materials, also cants out of the surface plane, inducing additional modulation of the CD signal (beyond $\sin(\alpha)$). Figure 4.27a was measured on resonance ($hv = 28$ eV) and so this should be predominantly sensitive to the Bi character. Our DFT calculations show a pronounced out-of-plane canting of the vectorial spin at higher in-plane momentum (corresponding to a greater hexagonal warping) for the spin-projection onto the Bi layer, as discussed. This is additionally supported by projecting the L_z OAM component onto the Bi layer for the bands at constant energy (fig. 4.27b) and projecting the Bi L_z onto the band dispersion (fig. 4.27c). Here, the L_z component goes to zero with decreasing in-plane momentum, indicating a fully in-plane $\boldsymbol{L}$

here (since as L_z is zero, $\boldsymbol{L} = \{L_x, L_y, 0\}$). From our CD k_x-k_y measurement at the Fermi level (fig. 4.27a) that shows significant warping at higher in-plane momentum, the CD signal has a 3-fold modulation for the outer band. This is again consistent with our assignment of a significant L_z component, giving an out-of-plane canting of OAM. For the inner band, the additional modulation of the CD signal has vanished, which is seen to correspond to a vanishing L_z from our calculations, giving a predominantly in-plane OAM.

This changes significantly measuring off resonance. Figure 4.27d shows the CD for an MDC along the k_y direction at the Fermi level for a wide range of photon energies. Most notably there are several changes in sign of the dichroism for a given k_y for example comparing: $h\nu = 60, 100, 110, 120$ eV. The corresponding Fermi surfaces for $h\nu = 110, 120$ eV are shown in figure 4.27e,f. Both Fermi surfaces show an approximately $\sin(\alpha)$ modulation to the CD signal, consistent with the Fermi momentum being smaller. A small Fermi momentum then implies a less significant L_z at the Fermi level. This could therefore be representative of the in-plane SAM (through anti-alignment of a mostly in-plane OAM). Clearly this assignment has problems since the in-plane spin should overall be Rashba-like (counter-propagating on the two Fermi surfaces) but in figure 4.27e this would lead to spin textures propagating in the same direction on both bands. This is fully consistent with measurements by Crepaldi *et al.*, who measure a sign change in the CD at $h\nu \approx 100$ eV for the outer band in BiTeI, as well as multiple sign changes for a range of photon energies for the BiTeX family [118] (note only a single sign change in BiTeI for the outer band, still consistent with our measurements).

The sign changing CD signal has been seen also in topological insulator surface states [119, 120]. Scholz *et al.* state that since the initial states cannot change with photon energy, the changing sign of the dichroism signal must be a final state effect [120]. Through one-step calculations they suggest that when a transition into a d-orbital final state is possible there is a significant change in dichroism observed, given the p-like nature of the electronic states for TSSs. This effect is also seen in one-step calculations on Au(111) [121],

where the relative phase of different orbital character final states causes the sign change.

Another explanation for similar photon energy dependent spectral weight changes has been put forward by Zhu *et al.* for layered materials (in their case Bi_2Se_3) [105]. They describe the total wavefunction of the topological surface state in Bi_2Se_3 as a combination of layer dependent eigenstates $\Psi_{\mathrm{TSS}} = \sum_{i,\sigma} \alpha_i \psi^{\sigma}_{i,\boldsymbol{k}_{||}}$ (as we have done for BiTeI), and factor out a complex phase from the final state:

$$I \propto \sum_{\sigma} \Big| \sum_{i} e^{-ik_z z_i} \langle e^{i\boldsymbol{k}_{||}\cdot\boldsymbol{r}_{||}} | \boldsymbol{A}\cdot\boldsymbol{p} | \alpha_i \psi^{\sigma}_{i,\boldsymbol{k}_{||}} \rangle \Big|^2 \tag{4.14}$$

where z_i is the depth of the i^{th} layer. This phase factor $e^{-ik_z z_i}$ then depends on the path length resulting from the layer difference. The photoemission intensity variations can then be explained as interference effects from layers with different orbital textures [105], another possible cause for the sign changing CD in BiTeI.

4.5 Conclusions

Coupled spin-orbital textures are now seen to be a generic consequence of spin-orbit coupling in solids but determining the precise origin of all the effects observed will still need considerable theoretical work. Notably, after publishing our work, in addition to the spin-resolved ARPES study on BiTeI showing the orbitally-resolved spin texture [111], similar effects have also now been shown in the surface alloy states Bi/Ag(111) and Bi/Cu(111) [122]. Whereas in BiTeI, coupled spin-orbital textures are a result of the global inversion symmetry breaking, the same effects being observed in the surface alloys confirms this to arise even from the local inversion symmetry breaking. This has been supported by calculations where it was shown that orbital textures arise regardless whether the inversion symmetry breaking is global or local [123, 124], which will be central to the discussion in the following chapter and developing understanding of spin-orbit physics in general.

Chapter 5

Spin-valley locking in 2H-$NbSe_2$

5.1 From Graphene to Transition-metal Dichalcogenides

In the previous chapter, global inversion symmetry breaking led to a giant bulk spin-splitting of the conduction bands. This was accompanied by a previously unexpected momentum-space orbital polarisation. In this chapter we will see how related symmetry considerations again lead to a hidden kind of order: an unexpected spin-polarisation of the electronic structure in a centrosymmetric crystal. In this case it arises from breaking local inversion symmetry in the crystal structure of the transition metal dichalcogenide class of materials. To understand how this all fits together, we will first briefly discuss the familiar material graphene and consider symmetry breaking here.

5.1.1 Graphene

There is a great deal of material available on the electronic structure of graphene (e.g. [125–127]), the earliest tight binding models dating back to 1947 [128]. This introduction will follow the chapter by E. McCann in [125]. Graphene is a well known allotrope of carbon, basically equivalent to a single layer of graphite. The atomic structure of graphene is a honeycomb structure since there are two atoms in the primitive unit cell that can be translated to the adjacent sites of the underlying hexagonal Bravais lattice

by the lattice vectors $\boldsymbol{a}_1$ and $\boldsymbol{a}_2$:

$$\boldsymbol{a}_1 = \left(\frac{a}{2}, \frac{\sqrt{3}a}{2}\right), \boldsymbol{a}_2 = \left(\frac{a}{2}, -\frac{\sqrt{3}a}{2}\right) \tag{5.1}$$

where $a = |\boldsymbol{a}_{1,2}|$ is the lattice constant (fig. 5.1a). These have the corresponding reciprocal lattice vectors (fig. 5.1b):

$$\boldsymbol{b}_1 = \left(\frac{2\pi}{a}, \frac{2\pi}{\sqrt{3}a}\right), \boldsymbol{b}_2 = \left(\frac{2\pi}{a}, -\frac{2\pi}{\sqrt{3}a}\right). \tag{5.2}$$

resulting in a hexagonal Brillouin zone.

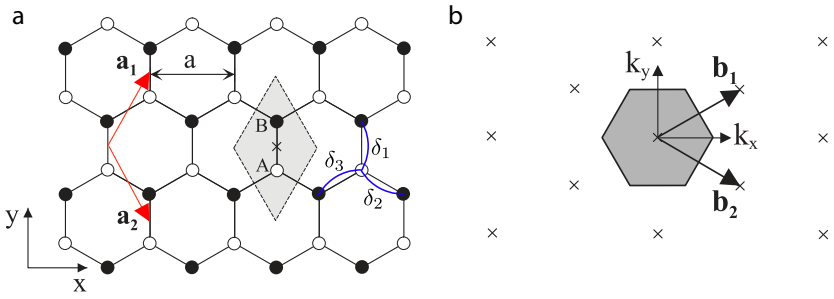

FIGURE 5.1: Real space and reciprocal space lattice of graphene. Adapted from [125]

The Hamiltonian can be constructed in the generic way described in chapter 2: diagonal terms describe the on-site energies, while off-diagonal terms describe hopping between orbitals. The dominant contribution to conduction comes from the p_z orbitals so it is sufficient to consider only these [128]. In the Slater-Koster scheme described in chapter 2 the interaction between the p_z orbitals extruding perpendicular to the graphene lattice forms π bonds (so the bands formed from these are called the π bands of graphene). If the orbitals are not strictly orthogonal the overlap should be taken into account (shown in [125]) but we will neglect it for simplicity. There is then a p_z orbital from the atom on the A and the B sublattice (fig. 5.1) forming a 2×2 Hamiltonian to describe the bonding (π) and antibonding (π^*) states:

$$H = \begin{pmatrix} \varepsilon_A & -tf(\boldsymbol{k}) \\ -tf^*(\boldsymbol{k}) & \varepsilon_B \end{pmatrix} \tag{5.3}$$

where t is the hopping parameter, $\varepsilon_{A,B}$ is the on-site energy for the A or B site, and $f(\boldsymbol{k})$ contains the momentum dependence of the hopping arising from the hopping vectors. There are three hopping vectors, considering only nearest-neighbours, given by:

$$\boldsymbol{\delta}_1 = \left(0, \quad \frac{a}{\sqrt{3}}\right), \quad \boldsymbol{\delta}_2 = \left(\frac{a}{2}, -\frac{a}{2\sqrt{3}}\right), \quad \boldsymbol{\delta}_3 = \left(-\frac{a}{2}, -\frac{a}{2\sqrt{3}}\right) \tag{5.4}$$

where $\boldsymbol{\delta}_{1,2,3}$ is the hopping vector from an A site to the nearest B site or vice versa (fig. 5.1a). The momentum dependence of the hopping is then given by:

$$f(\boldsymbol{k}) = \sum_i e^{i(\boldsymbol{k}\cdot\boldsymbol{\delta}_i)} = e^{ik_y a/\sqrt{3}} + 2e^{-ik_y a/2\sqrt{3}} cos(k_x a/2). \tag{5.5}$$

The Hamiltonian can then be diagonalised, having solutions of the form:

$$E_\pm = \frac{\varepsilon_A + \varepsilon_B}{2} \pm \frac{\sqrt{(\varepsilon_A - \varepsilon_B)^2 + 4t^2|f(\boldsymbol{k})|^2}}{2} \tag{5.6}$$

where $E_-(E_+)$ denotes the bonding π (antibonding π^*) band respectively.

In graphene the two sites forming the A and B sublattices both contain a carbon atom. Applying the parity operator to the lattice, the lattice is transformed such that an A site maps to a B site and vice versa. Since these are both carbon atoms, the ideal honeycomb lattice of graphene possess inversion symmetry. In this simple case, the on-site energies are equivalent to the on-site energy of the carbon $2p_z$ orbital $\varepsilon_A = \varepsilon_B = \varepsilon_{p_z}$. This reduces the eigenvalues to:

$$E_\pm = \varepsilon_{p_z} \pm t|f(\boldsymbol{k})|. \tag{5.7}$$

which gives a dispersion for the π bands as shown in figure 5.2. A consequence of this dispersion is that for non-zero nearest-neighbour hopping t, wherever the value of $f(\boldsymbol{k}) = 0$ the two eigenvalues are exactly equivalent (since then $E_\pm = \varepsilon_{p_z}$). This enforces a degeneracy at exactly the points where $f(\boldsymbol{k}) = 0$, whereas for $\varepsilon_A \neq \varepsilon_B$ in equation 5.6 there would always be a splitting between the eigenvalues (a band gap) of $(\varepsilon_A - \varepsilon_B)/2$.

The degeneracy of the π bands occurs at the K points (the Brillouin zone

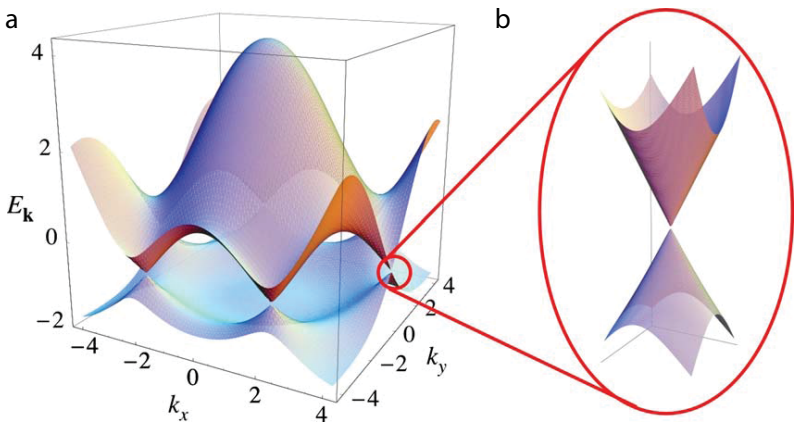

FIGURE 5.2: a) Electronic structure of the π-bands of graphene. b) Near Fermi-level dispersion around the K point showing the linear dispersion of the Dirac cone states. Reproduced from [126]

corners) given by $(\boldsymbol{b}_1+\boldsymbol{b}_2)/3 = \xi(\frac{4\pi}{3a}, 0)$ or equivalent combinations of reciprocal lattice vectors (fig. 5.1b), where $\xi = \pm 1$. This parameter is called the 'valley index', denoting the fact that the important band extrema (valleys) occur at these points. It has two values $\xi = \pm 1$, which in real space denotes the localisation of the electron density being either on an A sublattice (e.g. $\xi = +1$) or a B sublattice (e.g. $\xi = -1$). In momentum space, it distinguishes between the two inequivalent Brillouin zone corners that cannot be translated between by a reciprocal lattice vector: K and -K (-K is often called K'). This distinguishing property has significant consequences for physical properties that are sensitive to the valley index.

The enforced degeneracies (points where $f(\boldsymbol{k}) = 0$), occur for both values of the valley index so at both K and K'. This is only true exactly at the K_ξ points so we can evaluate this for a small momentum away from the K_ξ points $\boldsymbol{p} = \hbar\boldsymbol{k} - \hbar K_\xi$, which gives the hopping function:

$$f(\boldsymbol{k}) = e^{ip_y a/\sqrt{3}\hbar} + 2e^{-ip_y a/2\sqrt{3}\hbar} cos(\frac{2\pi\xi}{3} + \frac{p_x a}{2\hbar}) \tag{5.8}$$

$$\approx (1 + \frac{ip_y a}{\sqrt{3}\hbar}) + 2(1 - \frac{-ip_y a/2}{\sqrt{3}\hbar})(-\frac{1}{2} - \frac{\xi\sqrt{3}p_x a}{4\hbar}) \tag{5.9}$$

$$\approx -\frac{\sqrt{3}a}{2\hbar}(\xi p_x - ip_y) \tag{5.10}$$

after expansion and neglecting higher orders in momentum. This allows us

to write down the low energy effective Hamiltonian for the states close to the K_ξ points as:

$$H_{K_\xi} = v \begin{pmatrix} 0 & \xi p_x - i p_y \\ \xi p_x + i p_y & 0 \end{pmatrix} \tag{5.11}$$

where $v = \sqrt{3}at/2\hbar$ is the particle velocity. This can be diagonalised to give the following two eigenvalues and eigenstates:

$$E_\pm = \pm vp, \qquad \psi_\pm = \frac{1}{\sqrt{2}} \begin{pmatrix} 1 \\ \pm\xi e^{i\xi\phi} \end{pmatrix} e^{i\boldsymbol{p}\cdot\boldsymbol{r}/\hbar}. \tag{5.12}$$

where $\boldsymbol{p} = (p_x, p_y) = p(cos\phi, sin\phi)$. The dispersion relation is then linear close to the K point, so the electronic states here are described as Dirac fermions, with a velocity v. The two component wavefunction points to there being a spin-like quantity. This is not related to the intrinsic spin of the electrons but is a pseudospin that relates to the electron or hole density being localised to either the A or B sublattices. Since this is a spin-like quantity the effective Hamiltonian can be recast in terms of the Pauli matrices to give:

$$H = v(\xi\sigma_x p_x + \sigma_y p_y), \tag{5.13}$$

where σ_i refers to a Pauli matrix for the i^{th} component of the pseudospin.

Graphene has remarkable properties, owing to the fact that close to the K_ξ points the states are described by a Dirac-like effective Hamiltonian, such as an extraordinarily high mobility of carriers [126]. Its discovery drove a rise in interest in 2D materials and how to control and utilise this Dirac physics in the realm of condensed matter. However, the degeneracy at the K_ξ points make graphene less suitable for transistor-based device applications since the lack of band gap means that conduction cannot be easily tuned on or off. Originally this was part of the renewed interest in studying a related class of materials: transition-metal dichalcogenides.

5.2 Electronic properties of TMDs

Transition metal dichalcogenides (TMDs) are another class of 2D material, with the chemical composition MX_2, where M is a transition metal, and X is a chalcogen. A monolayer of a TMD is composed of hexagonal layers (for each of the constituent atoms) with the metal atom layer situated between two chalcogen atom layers in the order X-M-X (fig. 5.3b-e). For some TMDs, the monolayer crystal structure viewed along the c-axis (i.e. the in-plane crystal structure) resembles a graphene-like honeycomb structure (fig. 5.3a), with an M atom on a different sublattice to the X atoms. This describes the crystal structure we consider here.

In graphene, with the sublattice symmetry upheld, any nodes in $f(\boldsymbol{k})$ will provide a degeneracy in the band structure. In TMDs the sublattice symmetry is broken (fig. 5.3a), so there will always be a finite energy difference between the two eigenvalues in equation 5.6. There is therefore a band gap at the two valleys, which depends on the difference in on-site energies between the A and B sublattices. In analogy to equation 5.13, the effective Hamiltonian for TMDs near the K points (for now neglecting spin-orbit interactions) can then be written as [129]:

$$H = at(\xi\sigma_x p_x + \sigma_y p_y) + \frac{\Delta}{2}\sigma_z \tag{5.14}$$

where the a is the lattice parameter, and t is the hopping parameter, and Δ is the energy gap opened from the sublattice symmetry breaking. The additional term enforces the presence of a band gap by the means described above.

In addition to breaking the sublattice symmetry, TMDs allow mixing of a range of orbitals beyond the carbon $2s$ and $2p$. The band structure close to the Fermi level of TMDs is typically considered to contain contributions from the transition metal d-orbitals as well as the p-orbitals of the chalcogens [130, 131]. The stacking along the c-axis has several varieties, the most common being 1T, 2H and 3R (fig. 5.3). The number defines the number of

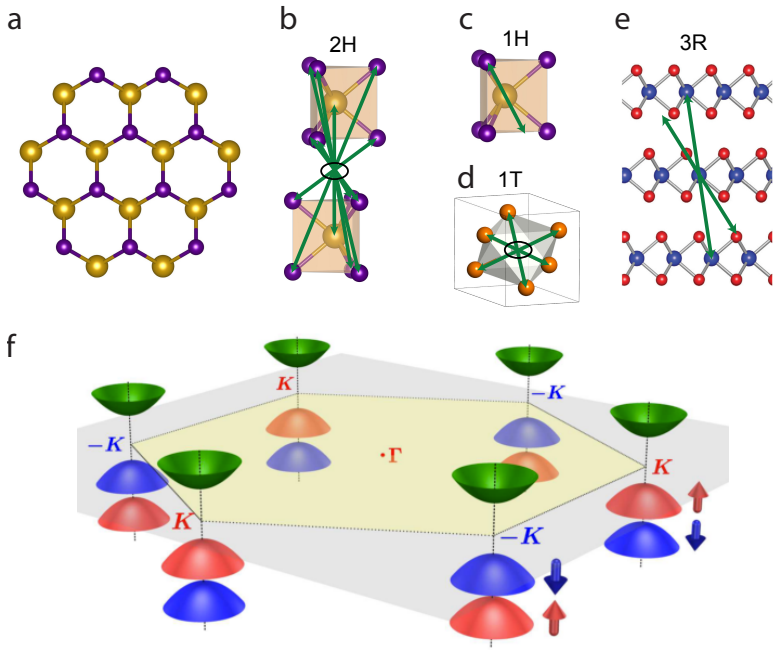

FIGURE 5.3: a) Honeycomb lattice of a monolayer TMD (of the 2H or 3R variety) viewed along the c-axis. The stacking along the c-axis is shown for the b) 2H, c) 1H, d) 1T and e) 3R polymorphs. Green arrows represent the application of the inversion (parity) operator. f) Low energy electronic structure of a monolayer TMD near the zone corners. f) Reproduced from [129]

MX_2 layers within a unit cell and the letter defines the symmetry (tetrahedral, hexagonal, or rhombohedral). The stacking order and symmetry also dictate whether or not the crystal structure possess inversion symmetry. The 1T and 2H structures possess an inversion centre, while the 1H and 3R structures are inversion asymmetric (fig. 5.3). The green arrows in figure 5.3b-e show the application of the inversion (parity) operator. In cases where the atoms map back onto each other, this shows the presence of inversion symmetry.

5.2.1 Spin-valley locking in TMDs

Transition metals and chalcogens, unlike carbon, can have strong spin-orbit coupling strengths which can further split bands, in the presence of broken inversion symmetry. The direction of the spin-orbit field ($\boldsymbol{B}_{so} \propto \nabla \boldsymbol{V} \times \boldsymbol{k}$) is determined from the momentum of the electrons and the crystal

field, which is forced to lie in-plane, from the mirror symmetry about the transition metal plane. The effective Hamiltonian close to the K points, including intra-atomic spin-orbit for a monolayer TMD, can then be written as [129]:

$$H = at(\xi\sigma_x p_x + \sigma_y p_y) + \frac{\Delta}{2}\sigma_z - \lambda\xi\frac{\sigma_z - 1}{2}s_z \tag{5.15}$$

where the last term couples to the s_z component of the electron's spin, with a spin-orbit strength λ. The first two terms are the same effective Hamiltonian as before (eq. 5.15) and this last term provides a spin-orbit splitting. This applies an on-site energy shift to the bands, further splitting the bands at the K points. It can also be seen from this term that the sign of the splitting depends on both the valley index ξ and the out-of-plane spin component s_z, i.e. the sign of the energy splitting for a given s_z is governed by the valley index ξ. This gives rise to a so called 'spin-valley coupling' in monolayers of these materials shown schematically in figure 5.3. For example, the upper valence band at a K point (positive ξ) possesses a spin-up s_z, while at the K' point (negative ξ), the upper valence band possesses a spin-down s_z. Since this is a spin-orbit driven effect, and the spin-orbit Hamiltonian is time-reversal symmetric, the observed spin-polarisation is itself also time-reversal symmetric (the K and K' points are also linked by the time reversal symmetry operator). In principle, this effect exists only in monolayer TMDs where inversion symmetry is explicitly broken (i.e. for the 1H or 1R polymorphs, fig. 5.3c).

Spin-valley coupling in these materials permits the study of the interplay between the pseudospin and spin degrees of freedom (for which there is a recent review article from 2014 [132]). There was a surge in interest in demonstrating control over spin-valley coupling in TMDs. In 2012, several groups independently showed experimental evidence for the existence of spin-valley coupling in semiconducting monolayer MoS_2 through polarised photoluminescence (PL) [133–135]. The experiment involved exciting excitonic transitions in this material between the filled valence bands and unfilled conduction bands, using circularly polarised light. The relaxation of

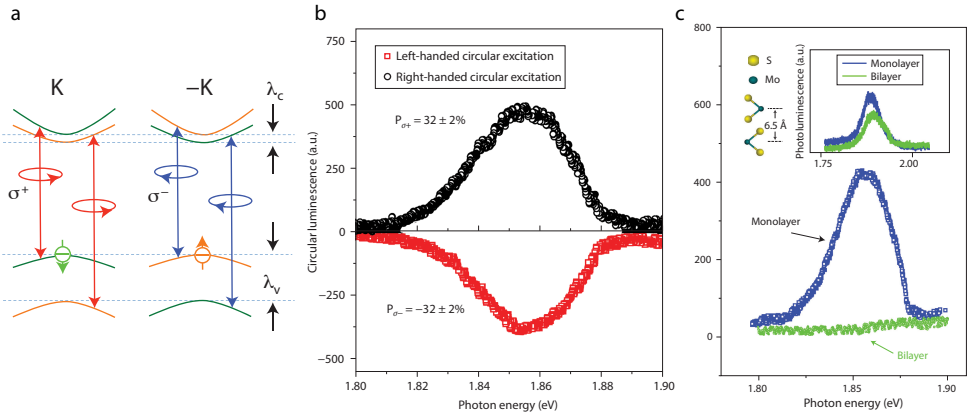

FIGURE 5.4: Polarised photoluminescence measurements on MoS_2. a) Illustration of valley-selective circularly polarised excitations. For an appropriate energy, through spin-valley locking, valley selectivity corresponds to spin selectivity. b) Measured circular polarisation upon exciting with circularly polarised light. Non-zero measured circular luminescence indicates spin-valley coupling. c) Measured circular luminescence on mono- and bilayer MoS_2. Absence of luminescence interpreted by preserved inversion symmetry (inset shows this is not a yield dependent effect). a) Adapted from [132]. b,c) Reproduced from [133]

the excited electron back into the valence band occurs through emission of a photon. With strong spin-valley coupling close to the K points, the excited electron is most likely to relax through the same channel as it was excited, since intervalley scattering requires a spin flip and (potentially) a large in-plane momentum, which are energetically less favourable, leading to robust valley coherence [132]. There is a strong photoluminescence yield if the excitation energy coincides with an allowed excitonic transition. The use of circularly polarised light for an appropriate energy (exciting from for example the upper valence band only) allows excitation of predominantly spin-up or spin-down electrons, due to the valley selection rules (fig. 5.4a).

Figure 5.4 demonstrates the results of Zeng *et al.* [133]. They excite with an energy corresponding to excitonic transitions from the upper valence band (UVB) to the appropriate exciton binding energy using circularly polarised light. In monolayers, from the calculations, these should have spin-valley coupling ensuring that the upper valence band spin state is set by the valley index (fig. 5.4a). The results show that the helicity of the observed light is predominantly the same as the helicity of the excitation (fig.

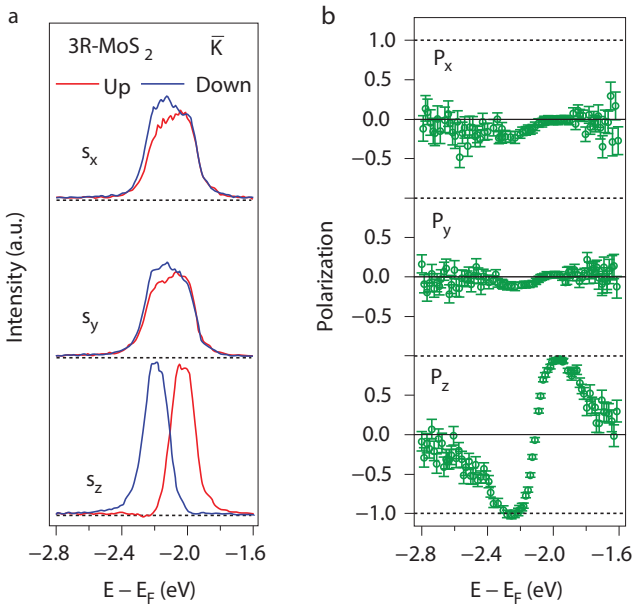

FIGURE 5.5: a) Spin-ARPES EDCs at the $\bar{K}$ point of 3R-MoS_2 for the full vectorial spin showing large s_z component, and no in-plane component. b) Corresponding spin-polarisation EDCs. Reproduced from [136]

5.4b), expected from the spin-valley locking of the monolayers, given that the monolayer 1H structure lacks inversion symmetry (fig. 5.3c). For the bilayer samples, the 2H structure then restores inversion symmetry. This is due to the two layers being 180^o rotated around the c-axis from one another. There is an inversion centre then between the two layers, whereby every atom from one monolayer can be mapped exactly onto an equivalent atom in the layer below by inverting the coordinate frame (fig. 5.3b). The polarisation of the measured PL signal is close to zero for the bilayer samples which they attribute to the dual constraints of inversion and time reversal symmetry, ensuring total spin-degeneracy of the electronic states. With no spin-valley coupling the excited states can relax into either spin-state with no luminescence helicity retention. The total photoluminescence yield is similar for mono- and bilayer samples so this is not an effect caused by a diminished total yield.

Spin-valley coupling has also been probed using spin-ARPES. Suzuki *et al.* perform spin-ARPES on 3R-MoS_2 [136]. The 1R monolayer structure is

identical to the 1H monolayer structure but subsequent layers are not rotated with respect to each other and have a staggered stacking sequence (fig. 5.3e). The 3R structure therefore breaks inversion symmetry while it is preserved in the 2H structure (fig. 5.3e). They measure spin-resolved EDCs at the $\bar{\mathrm{K}}$ point of 3R-MoS_2 for the s_z component of spin. By the symmetry arguments, and by equation 5.15, this should be the component of spin which couples to the valley degree of freedom (in monolayers). They measure a striking asymmetry in intensity of the red (spin-up) and blue (spin-down) traces corresponding to the upper and lower valence bands for the s_z component (fig. 5.5a). There is also far less spin-polarisation for the in-plane spin components (fig. 5.5), as expected from the theory (eq. 5.15). This is direct experimental evidence for spin-valley locking in bulk compounds. Additionally, Sugawara *et al.* probe monolayers of WSe_2 on bilayer graphene using spin-ARPES and see the expected strong out-of-plane spin-polarisation [137]. This is entirely consistent with theoretical predictions at this point.

5.2.2 From semiconducting to metallic TMDs

So far this discussion has introduced spin-valley coupling in semiconducting compounds but the electronic properties of transition metal dichalcogenides can vary significantly across the transition metal family. These properties are strongly affected by both the band filling and the point group symmetry of the transition metal ion, which governs the crystal field splitting [130]. A simple interpretation of the crystal field splitting, bonding and band filling is put forward by Wilson and Yoffe (1969) [138], which is summarised here. A 1T crystal structure has D_{3d} point group symmetry which puts the transition metal ion in an octahedral (sometimes called trigonal antiprismatic) coordination. A 1H (or also 1R) crystal structure has D_{3h} point group symmetry which puts the transition metal ion in a trigonal prismatic coordination (sometimes just called 'trigonal'). Focussing on the trigonal coordination, this splits the d orbital manifold into: $[\{d_{z^2}\}, \{d_{x^2-y^2,xy}\}, \{d_{xz,yz}\}]$. The d orbital manifold is energetically within the gap between bonding and

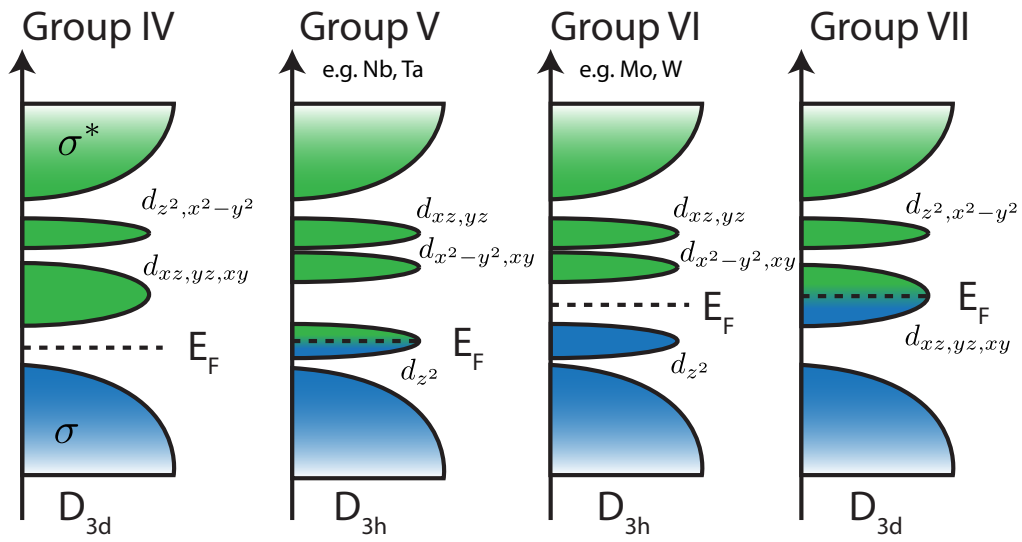

FIGURE 5.6: Idealised crystal field splitting of monolayer transition metal dichalcogenides as a function of transition metal group. This demonstrates schematically the band levels after CFS but ignores SOC which promotes significant orbital mixing and provides additional shifts in energy. Adapted from [139]

antibonding M-X σ bonds and the Fermi level will lie somewhere in these bands dependent on filling (fig. 5.6). In the trigonal prism, the bonding orbitals are the d_{xz} and d_{yz} orbitals, which offer the best distribution of charge for bonding. There are then a total of six d states which can be filled from the non-bonding bands.

From an ionic viewpoint, the oxidation states of the metal atom and the chalcogen atoms are +4 and -2 respectively [139]. The metal ion in the complex can then be considered as d^0 for Group IV transition metals, where all four of the valence electrons (e.g. $3d^2 4s^2$ for Ti) fill the two bonding orbitals. By extension then, this gives d^1 for Group V (e.g. Nb, Ta), d^2 for Group VI (e.g. Mo, W) and so on, for a maximum of six electrons, completely filling the available d states by Group X. From this it then follows that based on the filling and the coordination, some TMDs will be semiconducting and some will be metallic. Group V and VI TMDs most favourably form D_{3h} structures. This explains the semiconducting nature of WSe_2 as the d^2 electrons fully filling the lowest d_{z^2} band, whereas with one less electron, this band is nominally half filled in $NbSe_2$, a d^1 TMD, making it metallic. This

simple picture provides a neat interpretation of the electronic properties but neglects deviations from ionicity through covalent bonding, as well as ignoring the significant band splitting and orbital mixing from spin-orbit coupling. This also brings us on to the focus material of this chapter, 2H-$NbSe_2$.

5.3 Electronic structure of $NbSe_2$

5.3.1 Current understanding of collective phases

2H-$NbSe_2$ (now to be referred to as $NbSe_2$) is well-known to be a metallic TMD with instabilities to collective phases present upon cooling. These are a charge density wave phase (CDW) $T_{CDW} \approx 33$ K and a superconducting phase (SC) $T_{SC} \approx 7$ K [140–143]. Even though the presence of these phases has been known for decades, the precise origin of these phases is still debated now. It crystallises into the space group $P6_3/mmc$, which has global inversion symmetry, so these phases are currently thought to be derived from a fully spin-degenerate Fermi surface. To discuss the current interpretations and origins of these phases, it will first be necessary to introduce briefly charge density waves in general, before describing how they arise in $NbSe_2$.

In the conventional interpretation, an electronic system is able to reduce its total energy by undergoing lattice distortions, which modulates the charge density. These modulations of the electronic charge in real space have a periodicity associated with the Fermi wavevector, k_F, and so are described as a charge density 'wave'. The total energy of the system being lowered by a charge density wave (CDW) is well illustrated in 1D by a Peierls distortion [144], which is understood as follows.

Consider a 1D chain of equally spaced atoms with an inter-atom separation distance a, with a single electron per atom (fig. 5.7a). This produces a 1D electronic band with Brillouin zone boundaries at $k = \pm\frac{\pi}{a}$, which is filled up to $k_F < \pm\frac{\pi}{a}$ (fig. 5.7a). Displacing every other atom even a small amount, such that the 1D chain can now be viewed as being constructed

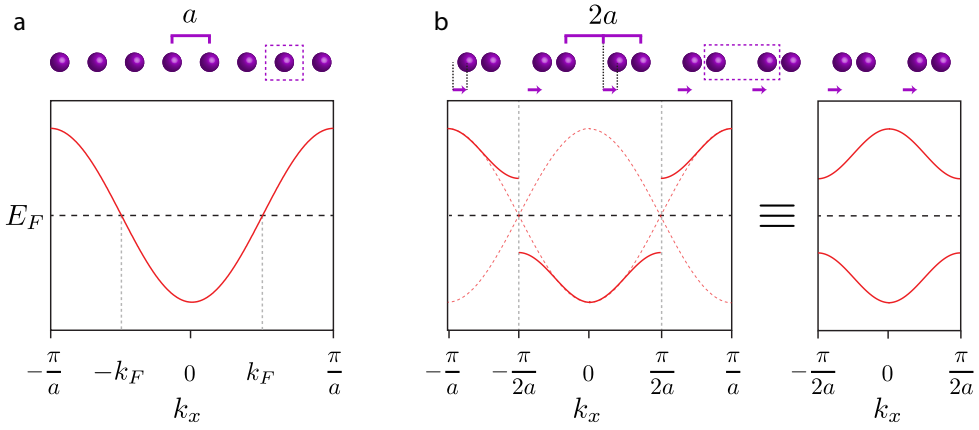

FIGURE 5.7: Schematic of a Peierls instability in a 1D chain causing a gap in the Fermi surface. a) 1D chain of atoms equally spaced by a unit cell length a. With one electron per atom the tight binding band shown is half filled up to k_F. b) Peierls instability displaces (for example) every second atom such that the 1D chain can be viewed as a chain of dimers with a doubled unit cell length. This modulation leads reduces the system energy through energy gaps at the Fermi wavevector as shown.

from pairs of atoms, effectively doubles both the unit cell size, and the number of atoms per unit cell (fig. 5.7b). In 1D this corresponds directly to a halving of the Brillouin zone size and a doubling of the number of bands (or 'backfolding' the original bands, from copies of the original bands with the new periodicity). This is achieved by an electronic gap forming at k_F, since electrons here can be moved with the least energy (fig. 5.7b). Since this only requires a small perturbation (so called 'weak coupling') away from exactly equally spaced atoms in the 1D chain, this system is highly susceptible to modulating the charge density in this way, producing gaps in the electronic spectrum.

Since this is defined as a response to the periodic modulation of atoms, it can be described by the static susceptibility at a wavevector $\boldsymbol{q}$ [145]:

$$\chi(\boldsymbol{q}) = \sum_{k} \frac{f_{\boldsymbol{k}+\boldsymbol{q}} - f_{\boldsymbol{k}}}{\varepsilon_{\boldsymbol{k}} - \varepsilon_{\boldsymbol{k}+\boldsymbol{q}}} \tag{5.16}$$

where $f_{\boldsymbol{k}}$ is the Fermi function, and $\varepsilon_{\boldsymbol{k}}$ is the electronic dispersion. In 1D for a free electron dispersion relation and at zero temperature (so f is a step

function at the Fermi momentum) this straightforwardly gives:

$$\chi_{1D} \propto \frac{1}{q} \ln \left(\frac{|q + 2k_F|}{|q - 2k_F|} \right). \tag{5.17}$$

This diverges at $q = 2k_F$ meaning the system is highly susceptible (unstable) to perturbations at this wavevector. This is analogous to the previous argument in which gaps in the electronic dispersion had to form at the Fermi wavevector in response to any small perturbation such as grouping the atoms in the chain.

In 1D this energy gap formation is also perfectly well understood from so-called Fermi surface nesting. Any large parallel sections of the Fermi surface that can be connected through scattering by a vector q are said to be nested and will produce similar sharp, large peaks in the susceptibility. In 1D, the Fermi surface is just two points at $k = \pm k_F$ and is perfectly nested, giving the previously mentioned sharp divergence at $q = 2k_F$. The nesting vector $q = 2k_F$ can then open a gap for the entire Fermi surface through modulation of the charge (a CDW) with a periodicity $\lambda_{CDW} = 2\pi/q$. For a weak coupling driven instability in higher dimensions, strong nesting is typically a requirement.

The divergence in the susceptibility is additionally understood as arising from a reduction in the ability of the conduction electrons to effectively screen the ions of the lattice. This shows up in the phonon dispersion as a singularity at these wavevectors: a Kohn anomaly, where $\partial\omega/\partial\boldsymbol{q} = \infty$ [146]. The gradient of the phonon dispersion becoming much steeper for the phonons which correspond to a lattice distortion is achieved by a reduction in their energy (a mode softening). In the case that the mode is softened to zero energy (or equivalently frequency), a static lattice distortion sets in.

The signature of the CDW phase in $NbSe_2$ is observed from transport measurements as a 'hump' in the resistivity [141, 143], and additionally as a sharp sign change in the hall coefficient [140], in both cases confirming the conduction electrons play a role. From neutron diffraction data, the CDW

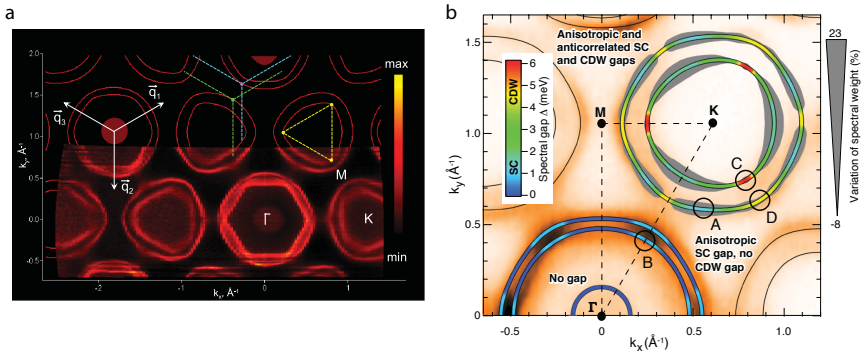

FIGURE 5.8: a) Fermi surface of $NbSe_2$ with CDW 3Q vectors overlaid. The coloured (green, blue, yellow) overlaid lines indicate CDW vectors linking proposed nested sections of FS. None of the connected sections shown have strong nesting. b) Fermi surface of $NbSe_2$ at $T = 1$ K showing the momentum space distribution of the CDW and SC gaps. a) Adapted from [148], b) Adapted from [149].

wavevector was established to be $\boldsymbol{q}_\delta = (1-\delta)\boldsymbol{a}^*/3$ along the $\bar{\Gamma}$-$\bar{\mathrm{M}}$ direction, where $a^*/3 = (4\pi/\sqrt{3}a)$ and a is the in-plane lattice parameter [142, 147]. This has a 3Q structure (meaning three equivalent $\boldsymbol{q}$ vectors 120^o rotated). The non-zero δ is indicative of the incommensurate nature of the CDW, which was shown to vary with temperature below T_{CDW}. While for $TaSe_2$ this incommensurate phase eventually locks in upon further reducing temperature ($\delta = 0$), this is not the case for $NbSe_2$ [147]. Even down to below the SC transition, δ continues to decrease.

Fermi surface nesting has previously been suggested to be at least partly a possible origin for the CDW in $NbSe_2$ [141, 148, 150–153] (though as we will discuss, this is most likely not the driving force). The Fermi surface is composed of an approximately hexagonal sheet and a further warped hexagonal sheet centred on $\bar{\Gamma}$, and two trigonally warped barrels centred on the $\bar{\mathrm{K}}$ points (fig. 5.8). These bands are known to be quasi-two-dimensional and predominantly derived from Nb $4d$ orbitals. An additional highly three dimensional 'pancake' Fermi surface is visible from the diffuse spectral weight centred at the $\bar{\Gamma}$ point. This highly three-dimensional pocket is predominantly derived from Se $4p_z$ orbital character with additional mixing from Nb $4d_{z^2}$ orbitals.

The 2D $\bar{\Gamma}$ sheets have been suggested to be well nested (due to their

hexagonal nature having large parallel portions) [151], as well as the outer $\bar{\mathrm{K}}$ barrels, where Kiss *et al.* measure the greatest CDW gaps [154]. However, it was later pointed out after more high resolution FS measurements that the $\boldsymbol{q}$ vector obtained from neutron diffraction does not fit well [148] (fig. 5.8a). Another early theoretical proposal points to the saddle point at $E_B \approx 50$ meV to be the cause, due to the small velocity and large density of states at this point [155] but this has not since been extended and deeper lying states cannot easily lower the total energy of the system. Multiple studies have suggested the inner $\bar{\mathrm{K}}$ barrel to have the appropriate size for nesting [148, 152, 153]. This is also consistent with the most precise momentum-space measurements of the CDW gap measured by ARPES at $T \approx 1$ K [149] (fig. 5.8b). In this ARPES study, the gap size was found to be a maximum of $\Delta_{CDW} = 6$ meV at the points along the $\bar{\mathrm{K}}$-$\bar{\mathrm{M}}$-$\bar{\mathrm{K}}'$ direction of the inner $\bar{\mathrm{K}}$ barrel. Consistent with some previous assertions, the nesting vectors were found to still not perfectly fit the inner $\bar{\mathrm{K}}$ sheet [148, 149, 152, 153], with the k_z-dispersion of this sheet given as a possible cause for the lack of strong nesting [153]. From these experiments, Fermi surface nesting has been suggested to provide a weak contribution at most, or no contribution at all, to the formation of the CDW. The general consensus of these studies is that electron-phonon coupling must play the more dominant role.

In phonon dispersions, the signatures of a CDW would be phonon mode softening at the onset of the CDW, for phonons corresponding to the $\boldsymbol{q}_{CDW}$, accompanied by sharp peaks in the susceptibility at these vectors. Strong electron-phonon interactions have been suggested by multiple studies as the main driving factor of the CDW in $NbSe_2$ [150, 156–159]. Through calculations of $\mathcal{I}m\chi(\boldsymbol{q})$, it has been shown that there are no sharply divergent peaks which would correspond to strong nesting [157, 158] effectively ruling this out as the main driving mechanism. Inelastic X-ray scattering measurements of the phonon modes corresponding to the $\boldsymbol{q}_{CDW}$ vector show that there is a mode softening to zero frequency at the CDW onset temperature [156, 159]. Sharp phonon mode softening is a signature simply of a structural transition. Crucially however, they measure a phonon mode softening

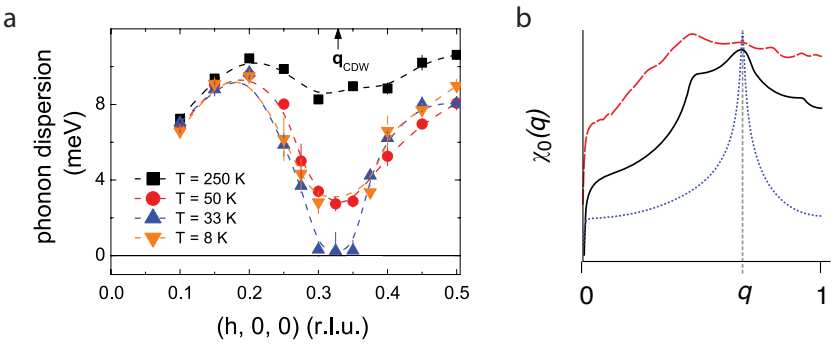

FIGURE 5.9: Phonon mode softening and susceptibility calculation for $NbSe_2$. a) Inelastic X-ray scattering measurements showing the relevant phonon mode softening to zero frequency for a broad range centred at $\boldsymbol{q}_{CDW}$. b) Static susceptibility measurements for orbital independent (red) and orbital dependent (black) electron-phonon coupling showing orbital dependent matrix elements are necessary to produce a peaked susceptibility. a) Reproduced from [156], b) Reproduced from [157]

over a broad range of momentum transfer around the main $\boldsymbol{q}_{CDW}$ vector (fig. 5.9a). This confirms nesting to not be the driving factor, but instead a $\boldsymbol{q}$-dependent electron-phonon coupling driven CDW phase. Through ARPES measurements it is already known that the electron-phonon coupling strength, λ_{el} is highly $\boldsymbol{k}$ dependent [149]. Recently, Flicker and van Wezel show that without including a momentum and orbital dependent coupling factor into the susceptibility calculation, the static susceptibility is effectively flat, and still only broadly peaked when calculating the susceptibility of just the inner K band [157] (fig. 5.9b). Detailed knowledge of the underlying Fermi surface including the orbital character is therefore essential to understanding the driving mechanism for the CDW in $NbSe_2$.

Further cooling drives the system into the superconducting phase where additional gaps in the Fermi surface open. The superconducting gap has been found to be both band dependent and anisotropic through recent ARPES measurements [149, 154, 160] (fig. 5.8b). This is likely due to the relative electron-phonon coupling strengths of the different bands. The CDW and SC phases can coexist, however they compete for the Fermi surface [149]. The CDW gap was shown not to increase below the SC transition and multiple additional SC gaps open up on the $\bar{\Gamma}$ and $\bar{K}$ barrels (fig. 5.8b). The SC gap

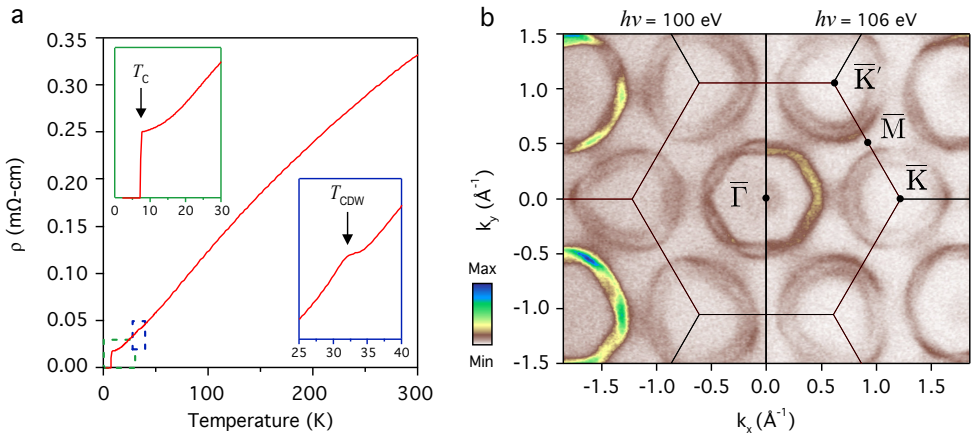

FIGURE 5.10: a) Resistivity as a function of temperature for 2H-$NbSe_2$ clearly showing transitions both to a charge-density wave $T_{CDW} \approx 33$ K and a superconducting phase $T_{SC} \approx 7$ K. b) Normal state (measured at $T = 50$ K) Fermi surface ($E_F \pm 20$ meV) of $NbSe_2$ measured by ARPES at $h\nu = 100$ eV (LHS) and $h\nu = 106$ eV (RHS).

reaches a maximum of $\Delta_{SC} \approx 2.5$ meV on the barrels around the $\bar{\text{K}}$ points. This momentum and band dependent gap size suggests that anisotropic multiband superconductivity best describes $NbSe_2$. This is supported by techniques besides ARPES including magnetisation measurements [161], scanning tunnelling microscopy [162], specific heat [163], thermal conductivity [164], and magnetic penetration depth [165].

In these studies of the CDW and the SC phases, the spin-degree of freedom is not considered to play a significant role. This is because the 2H-$NbSe_2$ crystal structure preserves global inversion symmetry as discussed, and by the dual constraints of this and time reversal symmetry, it should have a fully spin-degenerate band structure. On the contrary, we demonstrate through our ARPES and spin-ARPES studies that the normal state Fermi surface has a rich spin texture completely unexpected from the conventional symmetry constraints, which may provide an alternative route to understanding the collective phases present in this material.

5.3.2 Demonstrating spin-valley locking through ARPES and spin-ARPES

Our samples of 2H-$NbSe_2$ were grown at the University of Warwick by Prof. G. Balakrishnan. We have characterised multiple batches of samples by measuring their resistivity to low temperature (fig. 5.10a). Consistent with previous measurements [143], we observe a characteristic hump at $T_{CDW} \approx 33$ K and reduction to zero resistivity at $T_{SC} \approx 7$ K signifying the onset of the charge density wave and superconducting phases respectively. The batch of samples chosen for spin-ARPES investigation were selected based on the strength of the transition to the CDW phase, i.e. the samples with the greatest hump (fig. 5.10a). The vast majority of our measurements will be taking place understanding the normal state Fermi surface from which these phases arise. A characteristic measured Fermi surface is shown in figure 5.10b with the two quasi-2D hexagonally warped sheets centred around the $\bar{\Gamma}$ points (mostly Nb $4d$ derived), the two quasi-2D trigonally warped sheets around the $\bar{\mathrm{K}}$ points (mostly Nb $4d$ derived), and the diffuse spectral weight centred at the $\bar{\Gamma}$ points corresponding to the 3D pancake-like Fermi surface (mostly Se $4p_z$ derived).

We show the Fermi surface measured at two photon energies (fig. 5.10b). Since changing photon energy changes the value of k_z we probe in ARPES, some of the differences between the two k_x-k_y plots show up the 3D and quasi-2D nature of the bands. The pancake-like Fermi surface has most strong weight in the image measured at $h\nu = 106$ eV, while it is less visible in the $h\nu = 100$ eV measurement, indicating $h\nu = 106$ eV is closer to the bulk Γ point in k_z, where this Fermi surface is centred. The sharper $\bar{\Gamma}$-centred quasi-2D sheets are also seen to have some small k_z dispersion between these energies. The bands centred around $\bar{\mathrm{K}}$ points do not noticeably disperse between these two photon energies and so are likely more 2D (this will be clarified with measurements later this chapter).

Figure 5.11a shows the normal state ($T = 50$ K) electronic structure along the high symmetry directions $\bar{\mathrm{M}}$-$\bar{\Gamma}$-$\bar{\mathrm{K}}$ as measured by ARPES at $h\nu = 22$ eV at Diamond Light Source. At this much lower photon energy, the inelastic

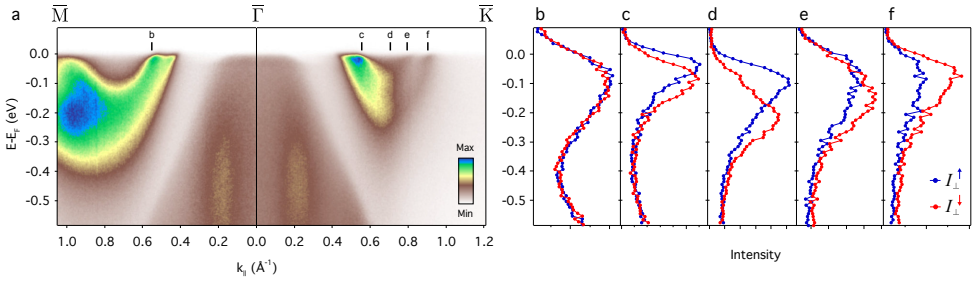

FIGURE 5.11: Spin-resolved bulk electronic structure showing spin-polarised bands. a) Dispersion measured by ARPES at $h\nu = 22$ eV along the $\bar{\text{M}}$-$\bar{\Gamma}$-$\bar{\text{K}}$ directions. b-f) Spin-ARPES EDCs measured at the marked momenta. Differences between spin-up (blue) and spin-down (red) traces reveal a strong spin-polarisation of these bands.

mean free path, λ, of an excited electron is now much shorter. Integrating over a smaller real space distance gives us a correspondingly larger width in k_z. An approximation of a lorentzian peak with a width Δk_z given by the inverse mean free path indicates that we are integrating over roughly two thirds of the Brillouin zone. The bands making up the highly dispersive pancake-like Fermi surface can therefore be seen as broad diffuse spectral weight centred at $\bar{\Gamma}$ for a wide range of binding energies corresponding to the dispersion in $E(k_z)$. Along $\bar{\text{M}}$-$\bar{\Gamma}$ there are two sharper peaks in the spectral weight which are seen to disperse to higher binding energies. These make up the hole-like hexagonally warped $\bar{\Gamma}$-centred Fermi surfaces.

Along the $\bar{\Gamma}$-$\bar{\text{K}}$ direction there are four Fermi crossings. The two closest to $\bar{\Gamma}$ compose the $\bar{\Gamma}$-centred Fermi surface, while the final two make up the trigonally warped hole-like bands. In the semiconducting TMDs of the same symmetry group, the valence band maxima are typically located at the $\bar{\Gamma}$-point and at the $\bar{\text{K}}$-point with a band minimum between these points along this direction, and a Fermi level in the gap. By comparison, this metallic compound has a Fermi level which has the valence band maxima at $\bar{\Gamma}$ and $\bar{\text{K}}$ above the Fermi level, leaving just the bands which connect up the $\bar{\Gamma}$ and $\bar{\text{K}}$ barrels below the Fermi surface. These Fermi crossings are reasonably sharp indicating their quasi-2D nature. Our measurements are consistent with previous measurements on these samples, including hints of a 'kink' in the dispersions below a threshold energy close to the Fermi energy. This

spectral feature has been well characterised in previous studies (e.g. [149, 166]) and is a hallmark of electron-phonon coupling present in this material, and is not a focal point of the thesis.

Figures 5.11b-f show the spin-resolved normal state ($T = 80$ K) electronic structure measured at $h\nu = 22$ eV by spin-ARPES at MAX Lab. Plotted are the true-spin EDCs (eq. 3.21) which account for the underlying spin-polarisation and the detection inefficiency. We have set up the experiment such that we are measuring the component of spin perpendicular to the surface plane, S_z. Shown are the spin-up (blue) and spin-down (red) EDCs. The spin-resolved EDCs demonstrate a striking spin-polarisation of the bands composing the Fermi surface, by the asymmetry of the spin-up and spin-down traces. For example, figure 5.11d shows the spin-resolved EDC at a momentum corresponding to the band bottom of these quasi-2D Nb $4d$ bands (the saddle point). From this, there are two clear peaks in the true-spin: a spin-up peak at $E_B \approx 100$ meV, and a spin-down peak at $E_B \approx 230$ meV. These correspond to the bands composing the outer and inner $\bar{\mathrm{K}}$ barrels (at higher in-plane momentum) and disperse to form the $\bar{\Gamma}$ barrels (at lower in-plane momentum), as measured in the conventional ARPES spectra (fig. 5.11a). The main difference is that these peaks are much broader in our spin-ARPES measurements. The efficiency of spin-ARPES being much lower than conventional ARPES requires that the resolution of the measurements must be reduced in order to gain intensity and acquire measurements in a reasonable time. This is often (but not exclusively) done by opening the beamline exit slits, increasing the intensity of the light but sacrificing the energy resolution, which leads to energy broadening. There is an additional large source of energy broadening determined by the size of the hole used to channel electrons into the spin transfer lens section (in principle this can be changed for other smaller holes as with analyser entrance slits). Gaussian fits at the Fermi edge for a known measurement temperature, under typical measurement settings, indicate energy resolutions of $\Delta E \sim 100$ meV (roughly an order of magnitude greater than typical measurement settings for conventional ARPES).

The spin-resolved EDC at this point (fig. 5.11d) shows that the inner and outer $\bar{K}$ barrels (as well as the inner and outer $\bar{\Gamma}$ barrels) possess opposite spin-polarisation. This is seen additionally from tracing the peak position from figure 5.11c-f. The spin-down trace disperses to lower binding energy and the spin-up trace is also seen to disperse up to the Fermi level, where the spin-resolved spectral weight begins to decrease, consistent with the peak centre dispersing further above the Fermi level. This follows the dispersion measured with conventional ARPES. This shows that there is a spin-polarisation of these bands even at the Fermi level, demonstrating the existence of spin-polarised quasiparticles in this centrosymmetric crystal structure.

In order for there to be any spin-polarisation (given the presence of upheld time reversal symmetry) it was thought to be strictly required that inversion symmetry is broken. The unit cell for the full crystal structure is inversion symmetric as discussed, however the centre of inversion lies between the two layers. Inversion symmetry is preserved only by considering both monolayers of $NbSe_2$ together in the unit cell. Individually, each monolayer of the 2H-$NbSe_2$ compound locally breaks inversion symmetry. In $NbSe_2$ this is due to the position of the Nb atom not being centred in the cage of chalcogen atoms (e.g. recalling fig. 5.3). This therefore allows the spin-orbit interaction to lift the spin-degeneracy locally within each layer [167, 168]. This is only the case if interlayer interactions are sufficiently weak, meaning the wavefunction describing the states is predominantly localised to one of the monolayers (fig. 5.12a). The existence of this spin-polarisation is seemingly opposed to conventional considerations of inversion symmetry and time reversal symmetry, and represents a significant paradigm shift in the way spin-orbit coupling is considered to affect materials. Our work is among the first works demonstrating that in addition to global inversion symmetry, the local inversion symmetry can have a significant role in lifting the spin-degeneracy of the band structure.

In work by Zeng *et al.* it was shown that without SOI the bands close to

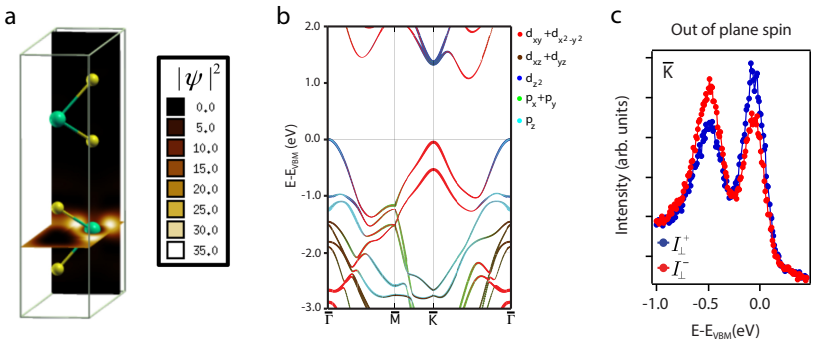

FIGURE 5.12: Layer-localised wavefunctions from a combination of spin-orbit interactions and orbital character. a) Electron density for a Bloch state $|K,\uparrow\rangle$ in bilayer WS_2 is strongly layer-localised. b) Orbitally-projected DFT calculations for WSe_2, showing the bands at the K point to be strongly in-plane d orbital derived, and bands at the Γ point to be mostly out-of-plane p orbital derived. c) Spin-resolved EDC at the $\bar{K}$ point of WSe_2 showing a strong out-of-plane spin-polarisation. a) Reproduced from [169], b-c) reproduced from [168].

the K point are split into two bands by bilayer splitting and a three dimensional manifold builds up by including additional layers [169]. However, they show that including SOI provides a significant energy cost to hopping between layers, reducing the electronic dimensionality. Spin-valley coupling enforces that states in the same valence band (e.g. the upper valence band (UVB)) at a given K_ξ are oppositely spin-polarised between the first (L1) and second layer (L2), i.e. $E^{\mathrm{UVB}}(K_\xi^{L1},\uparrow) = E^{\mathrm{UVB}}(K_\xi^{L2},\downarrow)$. This therefore requires a spin-flipping interaction to accompany any interlayer hopping (or a large transfer of in-plane momentum, or a change in energy corresponding to the spin-orbit splitting of the valence bands). This then imposes a strongly 2D layer-localised nature on the bands at the K points, where the valley index is well defined [169] (fig. 5.12a).

It was then shown by Zhang *et al.* that if the individual point group symmetry of a monolayer in a multilayer crystal structure breaks inversion symmetry, a real spin-polarisation can be supported by the electronic structure, irrespective of a globally preserved inversion symmetric crystal structure [167]. This layer-localised spin-polarisation was also independently demonstrated to exist in 2H-WSe_2, the semiconducting sister compound to $NbSe_2$, by our group [168]. In the Riley *et al.* study, it was shown through DFT

calculations and ARPES measurements that the wavefunctions for states at the $\bar{\mathrm{K}}$ points have a highly 2D nature mediated by the strong SOC, which greatly suppresses interlayer hopping. This effect is compounded by their in-plane orbital character close to the $\bar{\mathrm{K}}$ point, which is mostly d_{xy,x^2-y^2} as a result of strong spin-orbit mixing (fig. 5.12b). These bands then support a strong spin-polarisation measurable by spin-ARPES [168] (fig. 5.12c). Since the crystal structure of $NbSe_2$ is very similar to WSe_2, we can expect an equivalent orbital composition of the bands, but with a shifted Fermi level corresponding to $NbSe_2$ being a metal (fig. 5.6). It is worth noting that the wavefunction is most strongly 2D exactly at the valence band maxima, at the $\bar{\mathrm{K}}$ points in WSe_2. While this is below the Fermi level in semiconducting WSe_2, it is well above the Fermi level in $NbSe_2$. It was not initially clear that spin-polarised states would still be obtained here. This work, however clearly demonstrates that spin-polarisation persists up to the Fermi surface and should have consequences for the 2H-TMD metals and their collective phases. It additionally demonstrates the importance of interlayer hopping, going beyond the argument of simply 2D vs 3D states, discussed below.

In both WSe_2 and $NbSe_2$, the underlying mechanism is the same: the local inversion symmetry breaking of the monolayer, as opposed the global inversion symmetry of the full unit cell due to the 180^{o} rotation of the two constituent monolayers. The 180^{o} rotated monolayer layers have the effect that the spin-orbit field is completely reversed between the two monolayers of the unit cell. The spin-orbit field is given by $\boldsymbol{B}_{SO} \propto (\boldsymbol{\nabla V} \times \boldsymbol{k})$ so this 180^{o} rotation corresponds to a sign change of $\boldsymbol{\nabla V}$. Since the sign of the spin-polarisation is governed by the spin-orbit field, the spin-polarisation for the two layers is also entirely opposite such that combining these two layers restores full spin-degeneracy, and hence global inversion symmetry (fig. 5.3b,c). Since ARPES is a surface sensitive technique, we are able to measure predominantly the spin-polarisation localised to a single monolayer (the top layer) of cleaved samples of bulk $NbSe_2$. At this photon energy, the inelastic mean free path of a photoemitted electron at E_F is $\lambda \approx 5$ Å, which is significantly smaller than the c-axis lattice parameter $c = 12.55$ Å [147].

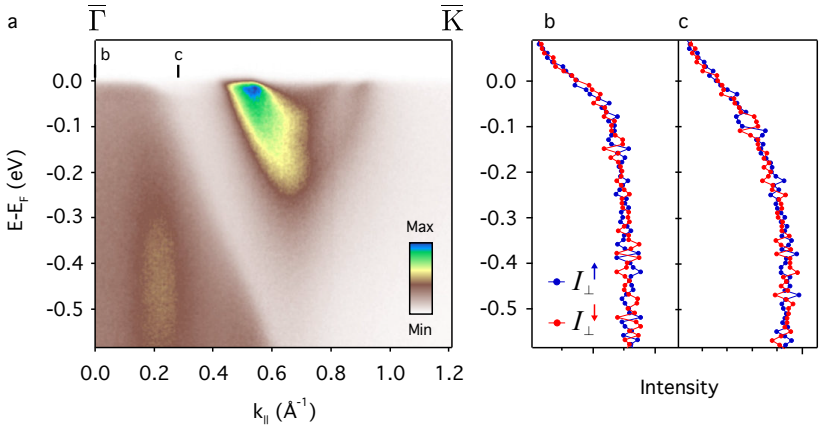

FIGURE 5.13: Spin-resolved bulk electronic structure showing spin-degeneracy. a) Dispersion measured by ARPES at $h\nu = 22$ eV along the $\bar{\Gamma}$-$\bar{K}$ direction. b-d) Spin-ARPES EDCs measured at the marked momenta. The spin-up (blue) and spin-down (red) traces are completely degenerate at these momenta.

From a Beer-Lambert law calculation for photoemission, close to normal emission, the signal for the second monolayer is decreased from the first by $I_{L2} \approx 0.3 I_{L1}$. Since the second layer has an opposite spin-polarisation and the intensity of this layer as measured from photoemission is not zero, the total measured spin integrated over all layers probed will be reduced from the absolute magnitude as projected onto a single layer. This can be further complicated by photoelectron interlayer interference effects, as described in the previous chapter [105]. These effects have been shown to reduce the measured spin-polarisation in WSe_2 to almost zero, by tuning the photon energy, becoming sensitive to a coherent superposition of the top two monolayers equally [168]. Despite this potential interference effect, and the inelastic mean free path, we are likely to be probing the spin texture of predominantly the top monolayer. In our measurements for $NbSe_2$, we are clearly not averaging both layers or the spin-resolved EDCs in figure 5.11 would show exactly zero spin-polarisation.

The spin-polarisation is therefore strongly tied to the dimensionality and orbital character of the underlying electronic states. This is well exemplified in figure 5.13. Here, alongside the conventional ARPES electronic structure, we show two spin-resolved EDCs. The $\bar{\Gamma}$ point (fig. 5.13b) is a time reversal

invariant momentum point (TRIM point) and so is necessarily doubly spin-degenerate, as we observe from our measurements. At a $\boldsymbol{k}_{||}$ corresponding to the chalcogen band, where there is no such TRIM double-degeneracy requirement, the states are still fully spin-degenerate. The states here are Se p_z derived and so naturally have a greater interlayer hopping due to their extended nature along the c-axis, and the smaller separation of Se atoms between layers, making the wavefunction more 3D. The extended nature of the wavefunction (or equivalently, the greater interlayer hopping) then means the electrons are influenced by the fully inversion symmetric unit cell. We can then understand the lack of spin-polarisation measured in figure 5.13 as being attributed to the more 3D chalcogen p_z bands (hybridised with d_{z^2}). These are both spatially extended in the z direction and the wavefunction experiences the global inversion symmetry being upheld (in addition to time reversal symmetry). The electrons therefore experience the exactly opposite spin-orbit fields of both layers in the 2H structure. As briefly suggested, suppression of interlayer hopping has intricacies beyond simply a binary allowing or forbidding of the spin-polarisation, which we will return to in detail at the end of the chapter.

As well as being locked to the layer index, the spin-polarisation is also locked to valley index, ξ, which can be seen in figure 5.14. This shows the electronic structure measured along $\bar{\mathrm{K}}$-$\bar{\mathrm{M}}$-$\bar{\mathrm{K}}'$ and corresponding spin-polarisation. There are four Fermi crossings in the dispersion measurement from conventional ARPES (fig. 5.14a), corresponding to the two trigonally warped $\bar{\mathrm{K}}$ barrels, for both a $\bar{\mathrm{K}}$ and a $\bar{\mathrm{K}}'$ point. The measured spin polarisation at the Fermi level is shown in the spin-resolved MDC above, corresponding to a $\boldsymbol{k}_{||}$ given by the solid black line (i.e. crossing all four bands). The inner $\bar{\mathrm{K}}$ barrel is spin-down (red), and the outer $\bar{\mathrm{K}}'$ barrel is spin-up (blue). This is exactly reversed for the $\bar{\mathrm{K}}'$ Fermi surfaces, where the inner (outer) barrel is spin-up (spin-down) respectively. This preserves time reversal symmetry, as it should, given the spin-orbit Hamiltonian is time reversal symmetric. This is exactly equivalent to the requirement for the spin-polarisation to be locked to the valley index, which again results directly

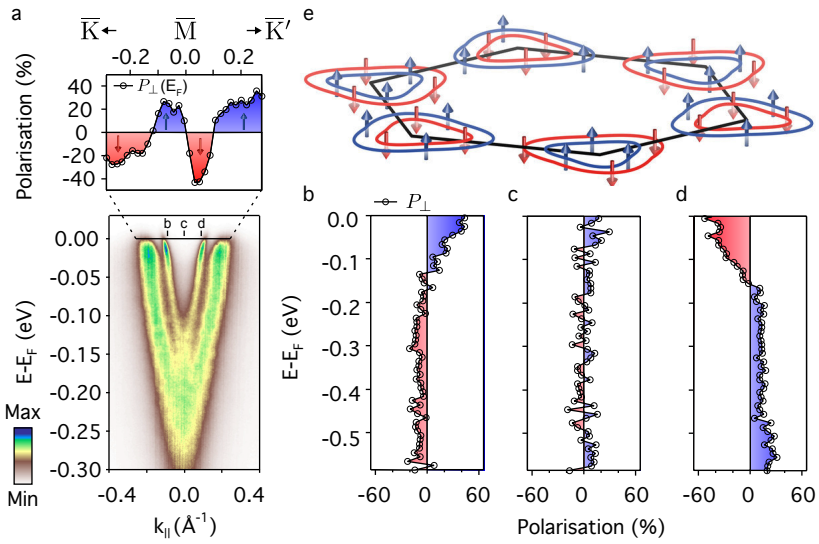

FIGURE 5.14: Spin-valley locking at the Fermi surface of $NbSe_2$. a) Dispersion measured along $\bar{K}$-$\bar{M}$-$\bar{K}'$ at $h\nu = 22$ eV, and spin-polarisation MDC at the Fermi level. b-d) Spin-polarisation EDCs at the marked momenta showing a valley-dependent switching of spin, shown schematically in (e).

from the effective Hamiltonian (eq. 5.15).

We can support this spin-resolved MDC with a series of spin-resolved EDCs at characteristic points: cutting the outer FS corresponding to a band towards the $\bar{K}$ point (fig. 5.14b); at a band towards the $\bar{K}'$ point (fig. 5.14d); and at the $\bar{M}$ point (fig. 5.14c). In the spin-polarisation EDC corresponding to bands towards the $\bar{K}$ point (fig. 5.14b), there are two regions of non-zero spin-polarisation. These correspond to the sharper outer band, and a broader inner band, which are shown to have opposite spin-polarisation as expected. This switches between bands centred around $\bar{K}$ and $\bar{K}'$ (fig. 5.14d) supporting the results from the spin-resolved MDC. The $\bar{M}$ point, another TRIM, is then necessarily spin-degenerate as shown from the polarisation EDC. This confirms that the spin-resolved MDC does indeed go through zero spin-polarisation exactly at the $\bar{M}$ point.

The requirement of the out-of-plane component of spin-polarisation to be zero at the $\bar{M}$ point has another consequence. States can have non-zero S_z away from high symmetry points. This must obey time reversal symmetry

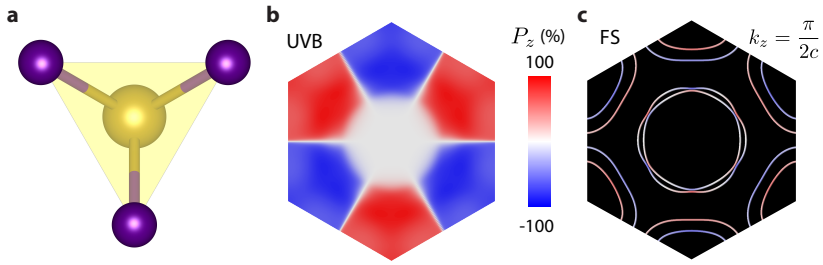

FIGURE 5.15: Symmetry enforced spin-degeneracy along Γ-M line. a) Crystal structure of monolayer trigonally coordinated TMD (e.g. $NbSe_2$, WSe_2) having C_3v point group symmetry. Symmetric under 3-fold rotation about the c-axis. b) Calculated z component of spin-polarisation of the upper valence band (UVB) in WSe_2. c) Calculated z component of spin-polarisation for the Fermi surface (FS) of $NbSe_2$ for an out-of-plane momentum away from high symmetry points (at $k_z = \frac{\pi}{2c}$). In b,c) since Γ and M are TRIM points, and the spin-polarisation must be both time reversal symmetric and 3-fold rotationally symmetric, the out-of-plane component of spin is necessarily zero along Γ-M. (b) Reproduced from [168]

(so must have an opposite sign between $\boldsymbol{k}$ and $-\boldsymbol{k}$). This must additionally be symmetric under 3-fold rotation about the c-axis, due to the 3-fold rotational symmetry operator of the C_3v point group (fig. 5.15a). The out-of-plane component must therefore go to exactly zero for states at any $\boldsymbol{k}$ anywhere along the Γ-M line in order for the out of plane component of the spin to change sign. This is seen for example in calculations of the out-of-plane component of spin-polarisation of the upper valence bands of WSe_2 (fig. 5.15b). This is additionally seen in calculations for $NbSe_2$ where the out-of-plane spin-polarisation is projected onto the Fermi surface, away from an out-of-plane momentum high symmetry point at $k_z = \frac{\pi}{2c}$ (fig. 5.15c). This explains the spin degeneracy measured in figure 5.11b. This measurement crosses the quasi-2D states forming the $\bar{\Gamma}$ barrels. Being quasi-2D in nature would suggest that suppressed interlayer hopping should lead to a measurable spin-polarisation as discussed. However, the measurement shows the bands in figure 5.11b to be exactly spin-degenerate, which is supported by calculations.

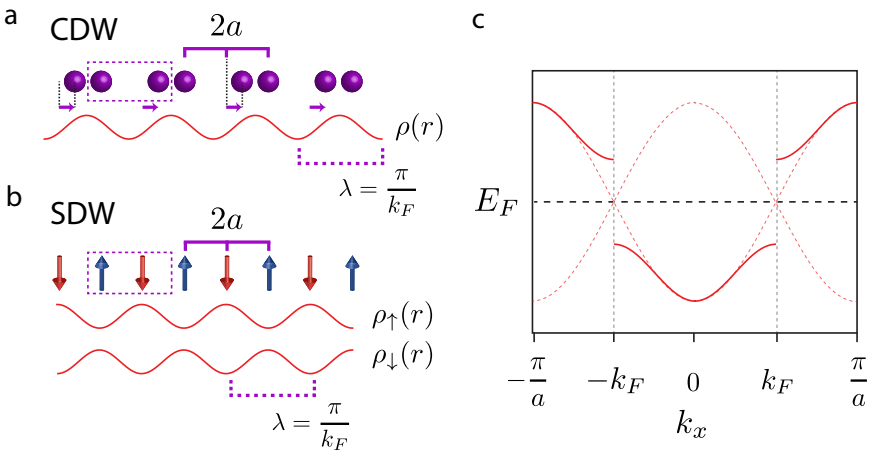

FIGURE 5.16: Examples of a 1D chain of atoms with one electron per atom. a) Displacing every other atom modulates the charge density with a periodicity twice the original lattice spacing, $2a$. b) Imposing an anti-alignment of neighbouring spins modulates the spin density by twice the original lattice spacing, $2a$. c) Dispersion relation for these instabilities inducing a gap at k_F. Adapted from [170].

5.3.3 Effect of spin-valley locking on the collective phases

We have established now that the normal state Fermi surface of $NbSe_2$ hosts spin-valley locking. This could have significance then on the collective phases which present upon cooling. The instabilities must be formed from quasiparticles at these normal state Fermi surfaces. The largest gaps opened by the CDW form on the inner $\bar{K}$ barrels along the $\bar{K}$-$\bar{M}$-$\bar{K}'$ directions [149] where we have just established there to be a large spin-polarisation within each monolayer of $NbSe_2$. Also the CDW wavevector discussed previously can be written as $\boldsymbol{q}_{CDW} = \{(1-\delta)a^*/3, 0, 0\}$ i.e. there is no z component [147]. Within each layer, interactions modulating the charge density corresponding to a Fermi surface centred at a K or K′ valley will therefore be interacting with spin-polarised quasi-particles, as opposed to previous assumptions that these were spin-degenerate.

Periodic modulations of spin-polarised charge density are termed spin-density waves (SDW), in analogy to charge density waves [171] (fig. 5.16). Spin-density waves periodically modulate the spin density in space. For example, equally spaced atoms forming a 1D chain with one electron per atom that alternates spin-up then spin-down per atom can be described as a

spin-density wave (fig. 5.16b). Considering the spin-polarised charge density, the spin-up charge density is periodic and has twice as long a period as the atomic spacing (fig. 5.16b). The spin-down charge density is identical to the spin-up charge density but out of phase by π (fig. 5.16b). Imposing this spin configuration corresponds to a doubling of the period of translational symmetry of the lattice, which then halves the Brillouin zone and reduces the kinetic energy (through SDW formation), analogous to the Peierls distortion described previously for CDWs (fig. 5.16c). From the figure (fig. 5.16) it may appear that the SDW leads to a constant charge density, however this is only the case in this special example and is often not the case. Another difference noticeable from CDWs is that the SDW is not accompanied by a lattice distortion, which is not the case for a CDW. Additionally, just as it is possible to describe an SDW as two CDWs out of phase, it is conversely possible to describe a CDW by two SDWs that are in phase with each other. Given we have shown the existence of spin-polarised bands in $NbSe_2$, the origin of the CDW may be related to a spin-density wave order. The CDW phase could be a combination of spin-density waves that are in phase with each other between neighbouring layers of the unit cell, where the different layer index imposes a sign change of the spin. Measurements show that there is certainly a lattice distortion however so there certainly must be a CDW component.

We were able to perform similar measurements as with our $NbSe_2$ spin-polarisation study on the related compound 2H-$TaSe_2$. This has an identical crystal structure to $NbSe_2$ with a stronger spin-orbit strength from the heavier Ta atoms. The underlying physics should therefore be well-comparable. The CDW phase in $TaSe_2$ has a much higher onset, with an incommensurate CDW phase setting in at $T_{CDW}^{IC} = 122$ K, and a lock-in commensurate CDW phase at $T_{CDW}^{C} = 90$ K [147]. We have been able to take preliminary spin-ARPES measurements of the out-of-plane component of spin in the commensurate CDW phase in $TaSe_2$ (at $T \approx 15$ K) along the $\bar{\Gamma}$-$\bar{M}$-$\bar{\Gamma}'$ direction (fig. 5.17). The dispersion along this direction looks qualitatively similar to that of $NbSe_2$ along this same direction (fig. 5.14a). The greater

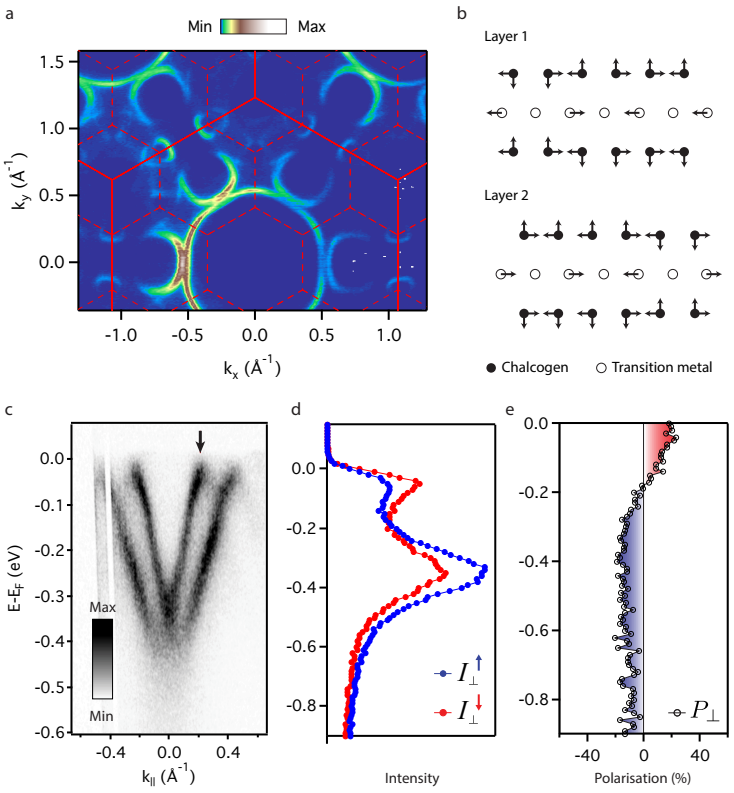

FIGURE 5.17: Spin-ARPES measurements showing spin-polarisation in the CDW phase of $TaSe_2$. a) Fermi surface of $TaSe_2$ measured with ARPES. Solid red lines mark the normal state Brillouin zone, and dashed lines marked the reconstructed zone in the commensurate (3×3) CDW phase. b) The CDW mediated lattice distortion in $TaSe_2$, adapted from [147]. Despite the complicated lattice distortion, the inversion symmetry between the two layers is upheld. c) Dispersion measured along $\bar{K}$-$\bar{M}$-$\bar{K}'$ at $T \approx 15$ K for $TaSe_2$. d) True-spin EDC at the momentum marked by the arrow in (c), for spin-up (blue) and spin-down (red) traces. e) The spin-polarisation, obtained using a Sherman function of $S = 0.3$ at the APE beamline of Ellettra.

spin-orbit strength produces a greater splitting of these bands as compared with $NbSe_2$.

Another key difference between the two compounds is that with the commensurate lock-in phase, there is a 3×3 reconstruction leading to a backfolding of the normal state bands (fig. 5.17a). The solid red lines corresponds to the normal state Brillouin zone, whereas dashed red lines correspond to the backfolded bands in the reconstructed Brillouin zone in the CDW phase. In the commensurate CDW phase, each reconstructed zone can be considered as containing a replica set of the normal state bands (in

a similar sense to the schematic in figure 5.7). Where these bands cross, this leads to a backfolding of the bands and CDW gaps open, lowering the system energy. This has been observed and well studied in $TaSe_2$ through ARPES recently e.g.[172–174] with an extensive review on the CDW phase found in [145]. The outer band along $\bar{K}$-$\bar{M}$-$\bar{K}'$ has some additional spectral weight with opposite velocity below where the CDW gap is formed (fig. 5.17c). This is broadly consistent with previous findings that these bands are gapped from the CDW phase and experience some backfolding. This shows we have measurements demonstrating the samples to be in the CDW phase, consistent with previous studies which focussed on the details of this phase (comprehensively covered in [145]).

Figures 5.17d,e show the measured true-spin EDCs and the spin-polarisation (in direct comparison to the same measurements in the normal state of $NbSe_2$ of figure 5.14). The true spin-resolved EDC has two clear peaks which are strongly and oppositely spin-polarised: one at the Fermi level, and one deeper in binding energy, corresponding to cutting both bands along this direction (fig. 5.17d). This is also evident from the sign change in the polarisation (fig. 5.17e).

Both $TaSe_2$ and $NbSe_2$ undergo a structural distortion into the CDW phase. In $TaSe_2$ the greatest atomic displacement is the Ta atoms moving $\delta \approx 0.048$ Å, compared with the in-plane lattice constant of $a = 3.436$ Å, so at most a 1.4% atomic displacement [147]. The lattice distortion is depicted in figure 5.17b, adapted from [147]. The lattice distortion still preserves global inversion symmetry (visible from the exact 180^o rotation between the two layers) and still breaks local inversion symmetry within each monolayer [147]. Our results then give direct evidence that the spin-polarisation carries through into the CDW phase despite any structural distortion, making this discovery directly relevant to the CDW phases across the TMD family.

The spin-polarised Fermi sea could also have implications for the superconducting phase. The largest gaps in the superconducting state form around the $\bar{\Gamma}$ barrels. The magnitude of the gaps on these sheets has a six-fold rotational symmetry, with the smallest gap sizes along the $\bar{\Gamma}$-$\bar{M}$

direction [149] (fig. 5.8b), strikingly similar to the symmetry of the spin-polarisation within a given layer. Given that time reversal symmetry is upheld, it is still possible to create zero momentum pseudo-spin-singlet Cooper pairs [175, 176]. Given the presence of strong spin-orbit coupling, it was theoretically shown that the order parameter can be a mixture of spin-singlet and spin-triplet pairing channels [177]. With inversion symmetry broken (within each monolayer), the same-spin triplet pairing channels are suppressed for zero momentum Cooper pairs (since there is no longer a state with the same spin at negative momentum) but spin-singlet-spin-triplet mixing can occur through the opposite spin channels [178]. This symmetry being globally preserved but locally broken within each layer could feasibly impose restrictions on the form of the order parameter [179, 180]. With the changing sign of the spin-polarisation between the two layers, it is possible that the order parameter could be characterised by a phase locking, giving an $s^{\pm}$ type order parameter, where the magnitude of the gap is the same but the phase is opposite in certain parts of the BZ. This kind of order has been studied in the context of multilayer non-centrosymmetric superconductors, described as an odd-parity pair-density wave state, where a staggered non-centrosymmetry and strong spin-orbit interactions are found to be necessary [179, 181]. A layer-dependent phase would mean the gap on the first and second layer would have opposite phase so the gap must close leading to a node. Since bulk probes find no evidence for nodes, this is not a likely scenario. It is possible that the phase could be band or valley dependent, where the size of the gap for a given band is unchanged but the phase between two valleys is opposite to form the $s^{\pm}$ state. After our $NbSe_2$ study, recent theoretical efforts have turned to understanding the order parameter in light of the spin-valley-layer locking clearly present [180]. In this work [180] they find a rich phase diagram of unconventional superconducting phases through a combination of inter- and intralayer spin-singlet pairing and interlayer spin-triplet pairing interactions. The consensus to-date is that the gap has different magnitudes on the different FS sheets and is certainly not isotropic.

Additionally, recent measurements on electrically gated monolayer MoS_2 have reported an 'Ising superconductivity' [182, 183], as well as on monolayer films of $NbSe_2$ [184]. MoS_2 is nominally insulating but ionic gating forms a 2DEG at the surface, where electrons are confined to the topmost layers. As discussed, in monolayers of both MoS_2 and $NbSe_2$ the single layers of the two layer unit cells individually break inversion symmetry, leading to an out-of-plane spin-polarisation locked to the valley index. Since these bands have a strongly $\pm\sigma_z$ spin vector aligned parallel to the spin-orbit field, this can be described as an Ising-like spin (as in fig. 5.14e). This is therefore referred to as 'Ising superconductivity' [182–184]. The proposed Ising superconductivity in these materials was used to explain the resilience of the superconducting state to an applied magnetic field. In both gated MoS_2 and monolayer $NbSe_2$ samples, the magnetic field required to break apart the Cooper pairs (the upper critical field H_{c2}) was found to vary significantly with the direction of the applied field. For an applied magnetic field aligned in the a-b plane of the sample, perpendicular to the spin-polarisation axis, H_{c2} was found to be far larger than the expected Pauli paramagnetic limit.

Pauli pair breaking (or Pauli paramagnetic limiting) is one of the two means by which magnetic fields can break apart Cooper pairs, the other being orbital pair breaking [185]. In a simple picture, Pauli pair breaking occurs by the change in energy gained by the alignment of a spin to the applied field, breaking a Cooper pair formed of opposite spins by inducing a Zeeman splitting. If the system can reduce its total energy by keeping the electrons in Cooper pairs, it will, until it becomes energetically favourable for the spins to align with the field. Orbital depairing breaks Cooper pairs by forming circulating currents (vortices) perpendicular to the applied field. These can be thought of as imposing a drift momentum $\boldsymbol{q}$ onto the electrons, which then implies that time reversal symmetry is now broken for these states since $E(\boldsymbol{k}+\boldsymbol{q},\uparrow) \neq E(-\boldsymbol{k}+\boldsymbol{q},\downarrow)$.

It was additionally shown that the enhancement of $H_{c2}^{||}$ decreases going from monolayer to bulk, which was attributed to the loss of the spin-valley

physics due to the restored inversion symmetry. However it is worth noting, the magnitude of orbital depairing for thin films for an applied magnetic field parallel to the film (i.e. same geometry as the measured $H_{c2}^{||}$), depends on d^2 where d is the thickness, and no such dependence exists for $H_{c2}^{\perp}$ [185]. Therefore even in conventional superconductors, thinning them down will anyway reduce the effect of orbital depairing and enhance $H_{c2}^{||}$ above the Pauli limit. The Pauli limit is however still surpassed by the large Zeeman energy required to overcome the pinning of the spin vector to the out-of-plane direction from alignment with the spin-orbit field. These studies have focussed on creating a 2D electronic environment where inversion symmetry is explicitly broken but from our measurements we now know that spin-valley locking persists even in the bulk.

5.3.4 Interplay between interlayer hopping and dimensionality

Moving away from the monolayer limit to bulk $NbSe_2$, we find that interlayer interactions play a significant role in determining the spin-polarisation. Our collaborator, M.S. Bahramy at RIKEN, Japan, has performed fully relativistic DFT calculations which are downfolded using maximally localised Wannier functions of Nb $4d$ and Se $4p$ orbitals to produce a tight binding Hamiltonian. The resulting Fermi surface spin-polarisation is found to have a rich dependence on the interlayer hopping, which will be discussed here.

Figure 5.18 shows the Fermi surface, with the S_z component of the spin projected onto the first and second monolayers of $NbSe_2$, displaying a pronounced polarisation throughout the bulk band structure. The two layers have exactly opposite magnitude spin-polarisation from our calculations such that the total spin-polarisation of the two layers combined is zero. This confirms that it is the local inversion symmetry breaking and opposite spin-orbit fields from the 180^o rotation of the two layers, which drives the spin-polarisation discussed above. Our measurements are therefore able to probe a non-equal combination of the layers such that we can resolve the spin-polarisation attributed to a single layer.

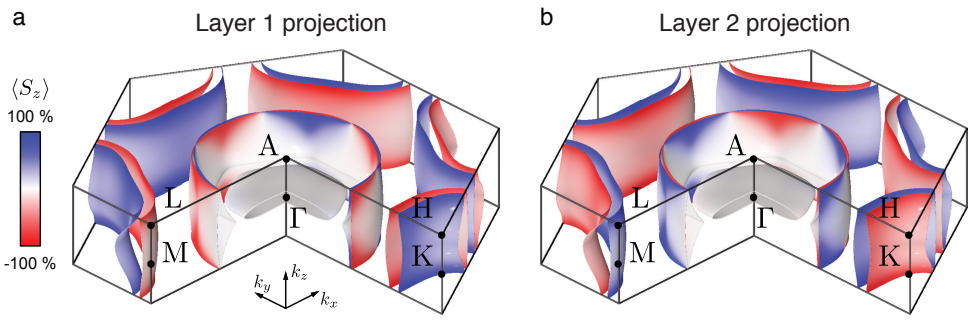

FIGURE 5.18: Out-of-plane component of the spin at the Fermi surface of $NbSe_2$ projected onto the first (a) and second (b) layers, showing pronounced spin-polarisation throughout the Brillouin zone. The spin-polarisation is exactly opposite between the two layers consistent with this being driven by local inversion symmetry breaking but upholding global inversion symmetry.

The local inversion symmetry breaking only induces spin-polarised bands if the interlayer hopping is small enough that the wavefunction does not have a great spatial extent over the fully inversion symmetric unit cell. Conversely, for large values of interlayer hopping, leading to a highly three-dimensional dispersion or equivalently a wavefunction highly delocalised over both layers of the unit cell, the spin-polarisation is completely suppressed. This is seen from the calculations for the spin-projection onto the highly 3D, pancake-like Fermi surface at the bulk Γ point. This has negligible spin-polarisation in both layers, consistent with our assignment from spin-ARPES (fig. 5.13).

In the opposite limit, if the interlayer hopping is almost negligible, we would expect nearly 100% spin-polarisation. This is the case in monolayer samples, where there are no layers to hop between in the perpendicular direction, and so the spin-polarisation is correspondingly very strong [168]. This is also the case in bulk WSe_2 where the bands at the $\bar{\text{K}}$ points are highly 2D (from the in-plane d orbitals, fig. 5.12b), leading to spin-polarisations of above 90% [168].

In our calculations, the strongest spin-polarisations are found at the Brillouin zone boundaries in out-of-plane momentum, $k_z = \pm\pi/c$ (fig. 5.18). In a tight binding picture, inter-unit cell hopping and intra-unit cell hopping

between monolayers of $NbSe_2$ have opposite phases. The interlayer hopping is then completely cancelled by these equivalent hoppings with opposite phase, at $k_z = \pm\pi/c$. With no interlayer hopping, this renders the Brillouin zone boundary effectively equivalent to an isolated monolayer. This explains the spin-polarisations of $> 90\%$ that we observe from our calculations in this plane ($k_z = \pm\pi/c$). In addition, the horizontal (x-y) mirror plane from the monolayer point group symmetry enforces that the spin-polarisation is zero along the A-L direction. This follows from the combination of preserved time-reversal symmetry and 3-fold rotational symmetry, as discussed before for the same direction at a different k_z (fig. 5.15). However, at the $k_z = \pm\pi/c$ plane, the complete suppression of interlayer hopping (rendering this plane equivalent to a monolayer) means the bands naturally support a spin-polarisation through spin-orbit interactions. Therefore, the required spin-degeneracy along the A-L direction is achieved by an enforced crossing of the oppositely spin-polarised bands (fig. 5.18).

This can be seen directly by the dispersion along k_z, and comparing the band dispersions with, and without spin-orbit interactions (fig. 5.19). Along the H-A-L plane ($k_z = \pm\pi/c$), without spin-orbit interactions, the complete suppression of interlayer hopping forces a fourfold degeneracy of the bands. That is: a spin-up and spin-down state, for the first and for second layer, for a total of four states (fig. 5.19a). The two Fermi crossings along H-A and the one Fermi crossing along A-L are therefore fourfold degenerate. Still considering the case without spin-orbit interactions, away from the H-A-L plane ($k_z = \pm\pi/c$), interlayer interactions open up a gap, as the bands disperse in k_z, which can be seen in figure 5.19a.

With the spin-orbit interaction included, the bands are allowed to further hybridise. Along the A-H direction, the spin-orbit interaction opens a gap, which lifts the fourfold degeneracy of the bands, even at $k_z = \pm\pi/c$. It can then be seen that the opening of the gap from spin-orbit interactions corresponds to the bands becoming more two-dimensional, from the reduced dispersion in k_z (fig. 5.19b). This is evidence in this material for a spin-orbit mediated suppression of interlayer hopping. This is the same mechanism

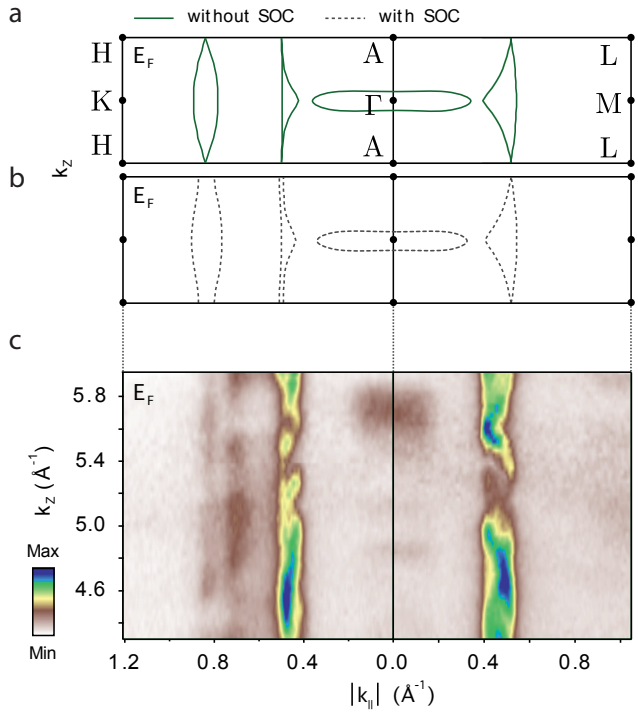

FIGURE 5.19: a,b) Calculated dispersion along k_z from DFT calculations for the bands at the Fermi level with and without the spin-orbit interaction (b and a respectively). c) Band structure at the Fermi level ($E_F \pm 15$ meV) along k_z as measured by ARPES. Measured between $h\upsilon = 60 - 130$ eV, using p-polarised light.

as described previously for the bulk semiconducting compounds. That is to say that spin-valley-layer locking suppresses interlayer hopping by the sign change of the electrons spin between the first and second layer ($L1$ and $L2$ respectively) for a given valley, i.e. $E(K_\xi^{L1}, \uparrow) = E(K_\xi^{L2}, \downarrow)$ [168, 169].

However, the fourfold degeneracy is not lifted by inclusion of spin-orbit interactions along A-L. This direction is the equivalent of the Γ-M direction (k_z=0) at a different k_z (fig. 5.19b). As discussed, time-reversal symmetry plus the 3-fold rotational symmetry about the c-axis ensures that the Γ-M ($k_z = 0$) and also the A-L direction ($k_z = \pm\pi/c$) are fully spin-degenerate. The added constraint that interlayer and intralayer hopping are effectively cancelled at $k_z = \pm\pi/c$ then also ensures that these states are fourfold-degenerate along the A-L direction (since there is no gap opened by interlayer hopping, or by spin-orbit interactions). Together this implies that the

dimensionality of the bands is intrinsically linked to the spin-orbit interaction through the spin-valley-layer locking even in the bulk.

The quasi-2D nature of the bands is confirmed from our measurements using photon energy dependent ARPES (fig. 5.19c). We see the same bands crossing the Fermi level as in the DFT calculations. For the quasi-2D bands composing the $\bar{\Gamma}$ sheets ($\boldsymbol{k}_{||} \approx 0.55$ Å^{-1}), we see some non-zero dispersion along the k_z direction, broadly consistent with the calculations. We see the additional bands forming the $\bar{\mathrm{K}}$ barrels at $\boldsymbol{k}_{||} \approx 0.8$ Å^{-1}, which seem to have a negligible dispersion, to within the resolution that we measure here. The diffuse patch of spectral weight at $\bar{\Gamma}$ that is localised in k_z clearly corresponds to the pancake-like Fermi surface. The dimensionality, being reinforced by the spin-orbit suppression, is then intricately linked to the spin-polarisation.

The link between dimensionality and spin-polarisation can also be seen from the calculated Fermi surface along the K-M-K direction (fig. 5.18). The inner band around the K point along the Γ-K-H-A direction is highly 2D but along the K-M-K direction this band has a more pronounced dispersion along k_z. This is evident both from the calculated Fermi surface, as well as in the dispersion measured using ARPES in figure 5.14a. That is to say, in the dispersion measured using ARPES in figure 5.14a, the outer bands are broader from their larger k_z dispersion compared with the inner band, which is sharper from the quasi-two-dimensionality. The comparatively larger k_z dispersion then leads to a correspondingly smaller spin-polarisation as seen in the calculated Fermi surface (fig. 5.18).

In bulk $NbSe_2$, the increased interlayer hopping giving rise to quasi-2D bands has another significant effect on the spin-polarisation as compared with the monolayer case. In the monolayer limit, the electronic momentum is entirely in-plane. This causes the spin-orbit field ($B_{so} \propto \nabla \boldsymbol{V} \times \boldsymbol{k}$) to lie entirely out of the surface plane, producing out-of-plane spin-polarisations of nearly 100%. In the bulk, finite interlayer interactions allow for an out-of-plane momentum, which can act to cant the spin-orbit field. This can lead to a non-negligible in-plane spin-polarisation, if the spin-orbit field is

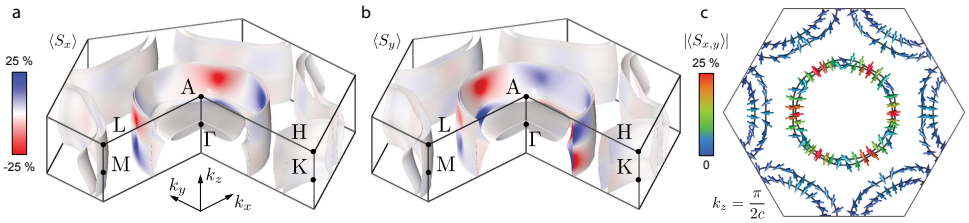

FIGURE 5.20: a) S_x and b) S_y components of the spin at the Fermi surface of $NbSe_2$ projected onto the first layer, showing that a non-negligible in-plane spin-polarisation can arise under certain conditions. The Γ barrels develop a disparate radial spin texture which is strongest along the Γ-K direction. c) Schematic of the in-plane spin-polarisation for $k_z = \pm\pi/2c$, where the spin-polarisation is shown to be greatest.

no longer fully along the z direction. This can be achieved when the total momentum vector is no longer entirely in-plane.

The resulting in-plane Fermi surface spin texture is shown for the S_x and S_y components of the spin (fig. 5.20a,b). At the K points in $NbSe_2$, the in-plane momentum is $\boldsymbol{k}_{||} \sim 1.2$ Å^{-1}. The maximum possible out-of-plane momentum available in the reduced zone scheme is $k_z = \pm\pi/c \sim 0.25$ Å^{-1}, so the momentum vector is predominantly in-plane here. The in-plane spin-polarisation projected onto the K barrels in our calculations, is almost negligible consistent with the interpretation of the total momentum vector of the spin-orbit field governing the strength of the spin-polarisation (fig. 5.20). Additionally, the in-plane spin-polarisation vanishes completely at $k_z = 0$ and $k_z = \pm\pi/c$. In both these cases, the total momentum vector can be viewed as being entirely in-plane (in the case of the Brillouin zone boundary, this is due to the opposite phase in a tight binding formalism), therefore providing an entirely out-of-plane spin-orbit field.

Considering now the Γ barrels, these are also quasi-2D and also have a Fermi surface spanning the full Brillouin zone in k_z, but at a comparatively smaller in-plane momentum. These are therefore present where the total momentum vector $\boldsymbol{k}$ has a similar magnitude of in-plane to out-of-plane momentum, $\boldsymbol{k}_{||}$ to k_z. This cants the total momentum vector, $\boldsymbol{k}$, towards the out-of-plane direction, which drives an in-plane spin-polarisation. Our

calculations show that these Γ barrels then host a significant in-plane spin-polarisation, reaching $\sim 25\%$ (fig. 5.20). This spin texture is predominantly radial, with an opposite sign for the two sheets, and strongly peaked along the Γ-K directions. This is seen most clearly in the schematic of the in-plane spin-vector for $k_z = \pi/2c$ (fig. 5.20c). While this demonstrates the existence of this theoretically, we will need to perform additional measurements to confirm and comprehensively map this in-plane spin texture.

5.4 Conclusions

Nonetheless, though this combined spin-ARPES and DFT study of bulk 2H-$NbSe_2$ we have demonstrated that a pronounced spin-valley-layer locking exists even in the bulk globally symmetric compound. This supports and extends our previous establishment of spin-valley locking in the related bulk compound, 2H-WSe_2 [168]. In accordance with predictions [167], this is shown then to be a generic consequence of the local inversion symmetry breaking within the globally inversion symmetric crystal structure. Spin-ARPES measurements exploiting selection rules of circularly polarised light have recently demonstrated spin-valley locking in bulk MoS_2 [186]. This has also been observed across a range of mono- and tri-layer $MoSe_2$ and WSe_2 using spin-ARPES [187]. Interestingly, they are unable to see the expected spin-polarisation in the bi-layer samples in this study, but this could be an experimental artefact. Domains that are multiples of 60^o rotated are energetically equivalent in growth but would superpose the electronic structure of a $\bar{\mathrm{K}}$ and a $\bar{\mathrm{K}}'$ point so measurements integrating over equal parts of these domains in real space would lead to a measurement of zero spin-polarisation. Several other effects could act to reduce the polarisation such as interference effects [105, 168].

Beyond providing additional evidence for spin-valley locking, our work demonstrates that this is not an effect limited to the semiconducting families, where the band maxima are well below the Fermi level. This is an

effect that persists in the collective phases and can potentially have a significant effect which will need considerable theoretical attention [180]. The quasi-2D nature of this material opens up the potential to explore the surrounding phase diagram through intercalation and doping: controlling the crystal structure and electronic structure to produce tailored exotic phases and explore the interplay of the spin-orbit interaction with dimensionality and symmetry breaking.

Chapter 6

Conclusions and outlook

This concludes the experimental work on the electronic structure of BiTeI and 2H-$NbSe_2$. Using spin- and angle-resolved photoemission spectroscopy, supported by density functional theory calculations provided by our collaborators, the underlying spin-resolved electronic structure of these materials was investigated.

Presented in this thesis is original work demonstrating a momentum-space ordering of the atomic orbitals in the bulk Rashba semiconductor BiTeI. This kind of momentum-space orbital polarisation was suggested in similar materials to be a hallmark of the topological surface states. However, our work on this related but topologically trivial material shows it to be a generic consequence of strong spin-orbit coupling. Revealing the orbital polarisation was achieved through exploiting one-electron matrix element spectral weight suppression through light polarisation dependent ARPES, to gain sensitivity to a particular component of the atomic orbitals. We also demonstrated how we were able to additionally gain atomic sensitivity through resonant enhancements from shallow core levels. Using both light polarisation and resonant enhancements in spin-ARPES we showed how the disparate atomic orbital textures of the bulk Rashba split bands drove characteristic spin textures. This is supported by our collaborators' density function theory calculations projecting the momentum dependence of the spin-polarisation arising from a particular atomic orbital onto the individual atomic layers. Together these findings demonstrate a previously undiscovered hierarchy of atomic species dependent coupled spin-orbital textures in this material, as a consequence simply of spin-orbit interactions.

This has implications in general for materials with strong spin-orbit interactions, suggesting a route to controlling spin-splitting through orbital manipulation.

The main focus of the chapter was the published result discussed above but throughout this chapter many findings were discussed that suggest opportunities for future work. Firstly, multiple reports have suggested the band dispersion in BiTeI to be non-parabolic (while others have ignored it completely). We demonstrate that this is certainly the case and suggest possible explanations. This however will need some theoretical consideration and some further analysis to fully uncover. Our work also provides evidence for the quantum well nature of the state observed in VUV-ARPES in BiTeI, which has been a matter of dispute. The photon energy dependence we show clearly has negligible k_z dispersion of all subbands over a full Brillouin zone. We show results from circular dichroism on BiTeI which we compare with our projections of the orbital angular momentum. This is in accordance with similar findings in topological insulator surface states, however, whether there is any link between circular dichroism and spin-angular momentum is still debatable. Finally, our work, and the independent work of Reinert's group, have begun to disentangle the spin-orbital texture through experimental measurements of BiTeI. Understanding how this can be controlled and manipulated (e.g. through chemical substitution or straining) in this material as well as potential candidate spintronic materials will no doubt be a fruitful area of research in the future.

Additionally presented was our original work on the spin-valley-layer locking in $NbSe_2$. Here we showed this to be a result of the local inversion symmetry breaking (in contrast to the case for BiTeI). The spin-polarisation was found to persist up to the Fermi surface of $NbSe_2$. We also report measurements on the sister compound $TaSe_2$ demonstrating that the spin-polarisation is still present in the charge density wave phase. This finding is therefore directly relevant to at least the charge density wave phase, and potentially other collective phases. Extending the idea of 2D versus 3D wavefunctions from our earlier work on WSe_2, our results on $NbSe_2$ clearly

highlight the importance of a continuous range of interlayer hopping. From our collaborators' density theory calculations, we illustrate that through the wavevector dependence of the spin-orbit field, the underlying bands can even develop an in-plane spin-polarisation. There are then a selection of parameters that can be tuned to drive this and related materials into nearby exotic phases.

This is the major question which calls for ongoing research, both theoretical and experimental. In the thesis we suggest and review some of the potential effects that the spin-polarised Fermi sea can have on the collective phases. Clearly however, detailed theoretical mechanisms and calculations are beyond the scope of the thesis. We began to measure the spin-polarisation in the CDW phase of $TaSe_2$, showing this to be experimentally accessible, however this will require comprehensive further study. Additionally, the details of the crystal structure are themselves not specifically important: rather it is the underlying symmetries. This suggests the results presented to be relevant to a wide range of materials that possess staggered non-centrosymmetry. In addition, while we show from theory the existence of an in-plane spin-polarisation, this was experimentally difficult to access. Mapping this spin texture and its dependence on the interlayer interactions will provide one route for ongoing work. Finally, given that the results presented depend so sensitively on interlayer hopping, this calls for experiments which can tune and control this parameter, and exploring its effect on the spin-polarisation. This can be achieved by mechanical strain or stress, as well as intercalation to offset the layers, chemical substitution, or simply by research across the range of TMDs.

Overall the work presented here opens up a realm of possibilities in these materials. In fact, given the importance of the underlying crystal symmetries and the orbital character governing the relative interlayer hopping strengths, there are a wide range of applicabilities providing a fruitful and lasting area of condensed matter research.

Bibliography

1. Manchon, A, Koo, H. C., Nitta, J, Frolov, S. M. & Duine, R. A. New perspectives for Rashba spin-orbit coupling. *Nature Materials* **14,** 871–882 (2015).
2. Bychkov, Y. A. & Rashba, E. I. Oscillatory effects and the magnetic susceptibility of carriers in inversion layers. *Journal of Physics C: Solid State Physics* **17,** 6039–6045 (1984).
3. Datta, S. & Das, B. Electronic analog of the electro-optic modulator. *Applied Physics Letters* **56,** 665–667 (1990).
4. Krasovskii, E. E. Spin-orbit coupling at surfaces and 2D materials. *Journal of Physics C* **27,** 493001 (2015).
5. Kane, C. L. & Moore, J. Topological Insulators. *Physics World* **24,** 31–36 (2007).
6. Hasan, M. Z. & Kane, C. L. Colloquium: Topological insulators. *Reviews of Modern Physics* **82,** 3045–3067 (2010).
7. Klitzing, K. V., Dorda, G. & Pepper, M. New method for high-accuracy determination of the fine-structure constant based on quantized hall resistance. *Physical Review Letters* **45,** 494–497 (1980).
8. Thouless, D. J., Kohmoto, M., Nightingale, M. P. & Den Nijs, M. Quantized hall conductance in a two-Dimensional periodic potential. *Physical Review Letters* **49,** 405–408 (1982).
9. Bahramy, M. S. *et al.* Ubiquitous formation of type-II bulk Dirac cones and topological surface states from a single orbital manifold in transition-metal dichalcogenides. *arXiv:1702.08177* (2017).
10. Kittel, C. *Introduction to solid state physics* 8th ed. (John Wiley & Sons, NJ, USA, 2005).
11. Ashcroft, N. W. & Mermin, N. D. *Solid State Physics* 1st ed. (Brooks/Cole, CA, USA, 1975).
12. Simon, S. H. *Solid State Basics* 2nd ed. (Oxford University Press, 2013).
13. Ibach, H. & Lüth, H. *Solid-State Physics* 4th ed. (Springer, Verlag, 2009).
14. Yu, P. & Cardona, M. *Fundamentals of Semiconductors - Physics and Materials Properties* 3rd ed. (Springer, Verlag, 2001).
15. Pauling, L. & Wilson, E. B. *Introduction to Quantum Mechanics* 1st ed. (McGraw-Hill, 1935).
16. Condon, E. & Shortley, G. *Theory of Atomic Spectra* 2nd ed. (Cambridge University Press, 1951).
17. Marzari, N., Mostofi, A. A., Yates, J. R., Souza, I. & Vanderbilt, D. Maximally localized Wannier functions: Theory and applications. *Reviews of Modern Physics* **84,** 1419 (2012).

18. Slater, J. C. & Koster, G. F. Simplified LCAO method for the periodic potential problem. *Physical Review* **94,** 1498–1524 (1954).
19. Schiff, L. I. *Quantum Mechanics* 3rd ed. (McGraw, 1968).
20. Lüth, H. *Solid Surfaces, Interfaces and Thin Films* 5th ed. (Springer, 2010).
21. Hüfner, S. *Photoelectron Spectroscopy: Principles and Applications* 3rd ed. (Springer, Verlag, 2003).
22. Sakurai, J. J. *Modern Quantum Mechanics* 2nd ed. (Addison, Wesley, 1994).
23. Winkler, R. *Spin-Orbit Coupling Effects in Two-Dimensional Electron and Hole Systems* 1st ed. (Springer, Verlag, 2003).
24. Petersen, L. & Hedegård, P. Simple tight-binding model of spin-orbit splitting of sp-derived surface states. *Surface Science* **459,** 49–56 (2000).
25. LaShell, S., McDougall, B. & Jensen, E. Spin Splitting of an Au(111) Surface State Band Observed with Angle Resolved Photoelectron Spectroscopy. *Physical Review Letters* **77,** 3419–3422 (1996).
26. Hoesch, M. *et al.* Spin structure of the Shockley surface state on Au(111). *Physical Review B* **69,** 241401 (2004).
27. Damascelli, A. Probing the Electronic Structure of Complex Systems by ARPES. *Physica Scripta* **T109,** 61 (2004).
28. Hertz, H. Ueber einen Einfluss des ultravioletten Lichtes auf die electrische Entladung. *Annalen der Physik* **31,** 983 (1887).
29. Einstein, A. Ueber einen die Erzeugung und Verwandlung des Lichtes betreffenden heuristischen Gesicht- spunkt. *Ann. Physik* **14,** 132 (1905).
30. Seah, M. P. & Dench, W. A. Quantitative Electron Spectroscopy of Surfaces: A Standard Data Base for Electron Inelastic Mean Free Paths in Solids. *Surface and Interface Analysis* **1,** 2–11 (1979).
31. Landolt, G. *Spin- and Angle-Resolved Photoelectron Spectroscopy on Topological Insulators and Bulk Rashba Systems* PhD thesis (University of Zurich, Switzerland, 2014).
32. Koo, H. C. *et al.* Control of Spin Precession in a Spin-Injected Field Effect Transistor. *Science* **325,** 1515–1519 (2009).
33. Berntsen, M. H. *et al.* A spin- and angle-resolving photoelectron spectrometer. *Review of Scientific Instruments* **81,** 035104 (2010).
34. Bigi, C. *et al.* Very Efficient Spin Polarization Analysis (VESPA): New Exchange Scattering-based Setup for Spin-resolved ARPES at APE-NFFA Beamline at Elettra. *arXiv:1610.06922* (2016).
35. Mott, N. F. The Scattering of Fast Electrons by Atomic Nuclei. *Proceedings of the Royal Society of London Series A* **124,** 425 (1929).
36. Mott, N. F. & Gonville, M. A. The Polarisation of Electrons by Double Scattering. *Proceedings of the Royal Society of London Series A* **135,** 429 (1932).
37. Mobilio, S., Boscherini, F. & Meneghini, C. *Synchrotron Radiation: Basics, Methods, and Applications* 1st ed. (Springer Heidelberg, 2015).
38. Panaccione, G. *et al.* Advanced photoelectric effect experiment beamline at Elettra: A surface science laboratory coupled with Synchrotron Radiation. *Review of Scientific Instruments* **80,** 4 (2009).

39. Bihlmayer, G, Rader, O & Winkler, R. Focus on the Rashba effect. *New Journal of Physics* **17,** 050202 (2015).
40. Nicolay, G, Reinert, F, Hu, S & Blaha, P. Spin-orbit splitting of the L-gap surface state on Au(111) and Ag(111). *Physical Review B,* 033407.
41. Koroteev, Y. M. *et al.* Strong spin-orbit splitting on Bi surfaces. *Physical Review Letters* **93,** 046403 (2004).
42. Varykhalov, A *et al.* Ir(111) Surface State with Giant Rashba Splitting Persists under Graphene in Air. *Physical Review Letters* **108,** 066804 (2012).
43. Reinert, F. Spin-orbit interaction in the photoemission spectra of noble metal surface states. *Journal of Physics: Condensed Matter* **15,** 693–705 (2003).
44. Tamai, A. *et al.* Spin-orbit splitting of the Shockley surface state on Cu(111). *Physical Review B* **87,** 075113 (2013).
45. Nicolay, G and Reinert, F and Forster, F and Ehm, D and Schmidt, S and Eltner, B, and Hüfner, S. About the stability of noble-metal surfaces during VUV-photoemission experiments. *Surface Science* **543,** 47–56 (2003).
46. Forster, F., Bendounan, A., Ziroff, J. & Reinert, F. Systematic studies on surface modifications by ARUPS on Shockley-type surface states. *Surface Science* **600,** 3870–3874 (2006).
47. Bihlmayer, G, Koroteev, Y. M., Echenique, P. M., Chulkov, E. V. & Blügel, S. The Rashba effect at metallic surfaces. *Surface Science* **600,** 3888–3891 (2006).
48. Krupin, O. *et al.* Rashba effect at magnetic metal surfaces. *Physical Review B* **71,** 201403 (2005).
49. Ast, C. R. *et al.* Giant spin splitting through surface alloying. *Physical Review Letters* **98,** 186807 (2007).
50. Bentmann, H. *et al.* Spin orientation and sign of the Rashba splitting in Bi/Cu(111). **84,** 115426 (2011).
51. Pacilé, D *et al.* Electronic structure of an ordered Pb/Ag(111) surface alloy: Theory and experiment. *Physical Review B* **73,** 245429 (2006).
52. Gierz, I *et al.* Silicon Surface with Giant Spin Splitting. *Physical Review Letters* **103,** 046803 (2009).
53. Premper, J, Trautmann, M, Henk, J & Bruno, P. Spin-orbit splitting in an anisotropic two-dimensional electron gas. *Physical Review B* **76,** 073310 (2007).
54. Bihlmayer, G., Blügel, S. & Chulkov, E. V. Enhanced Rashba spin-orbit splitting in Bi/Ag(111) and Pb/Ag(111) surface alloys from first principles. *Physical Review B* **75,** 195414 (2007).
55. Bahramy, M. S. & Ogawa, N. Bulk Rashba Semiconductors and Related Quantum Phenomena. *Advanced Materials,* 1605911 (2017).
56. Shevelkov, A. V., Dikarev, E. V., Shpanchenko, R. V. & Popovkin, B. A. Crystal Structures of Bismuth Tellurohalides BiTeX (X = Cl, Br, I) from X-Ray Powder Diffraction Data. *Journal of Solid State Chemistry* **114,** 379–384 (1995).

57. Ishizaka, K *et al.* Giant Rashba-type spin splitting in bulk BiTeI. *Nature Materials* **10,** 521–526 (2011).

58. Lee, J. S. *et al.* Optical response of relativistic electrons in the polar BiTeI semiconductor. *Physical Review Letters* **107** (2011).

59. Tomokiyo, A., Okada, T. & Kawano, S. Phase diagram of system (Bi_2Te_3)-(BiI_3) and crystal structure of BiTeI. *Japanese Journal of Applied Physics* **16,** 291–298 (1977).

60. Dich, N. T., Lošťák, P. & Horák, J. Preparation and basic physical properties of BiTeI single crystals. *Czechoslovak Journal of Physics B* **28,** 11 (1978).

61. Landolt, G. *et al.* Disentanglement of surface and bulk Rashba spin splittings in noncentrosymmetric BiTeI. *Physical Review Letters* **109,** 116403 (2012).

62. Eremeev, S. V., Nechaev, I. A. & Chulkov, E. V. Giant Rashba-type spin splitting at polar surfaces of BiTeI. *JETP Letters* **96,** 437–444 (2012).

63. Crepaldi, A. *et al.* Giant ambipolar rashba effect in the semiconductor BiTeI. *Physical Review Letters* **109,** 096803 (2012).

64. Sakano, M. *et al.* Strongly spin-orbit coupled two-dimensional electron gas emerging near the surface of polar semiconductors. *Physical Review Letters* **110,** 107204 (2013).

65. Eremeev, S. V., Rusinov, I. P., Nechaev, I. A. & Chulkov, E. V. Rashba split surface states in BiTeBr. *New Journal of Physics* **15,** 075015 (2013).

66. Landolt, G. *et al.* Bulk and surface Rashba splitting in single termination BiTeCl. *New Journal of Physics* **15,** 085022 (2013).

67. Sakano, M. *et al.* Three-dimensional bulk band dispersion in polar BiTeI with giant Rashba-type spin splitting. *Physical Review B* **86,** 085204 (2012).

68. Bahramy, M. S., Arita, R. & Nagaosa, N. Origin of giant bulk Rashba splitting: Application to BiTeI. *Physical Review B* **84,** 2–5 (2011).

69. Zhang, H. *et al.* Topological insulators in Bi_2Se_3, Bi_2Te_3 and Sb_2Te_3 with a single Dirac cone on the surface. *Nature Physics* **5,** 438–442 (2009).

70. Bahramy, M., Yang, B.-J., Arita, R. & Nagaosa, N. Emergence of non-centrosymmetric topological insulating phase in BiTeI under pressure. *Nature Communications* **3,** 679 (2012).

71. Hsieh, D *et al.* A tunable topological insulator in the spin helical Dirac transport regime. *Nature* **460,** 1101–1105 (2009).

72. Xia, Y. *et al.* Observation of a large-gap topological-insulator class with a single Dirac cone on the surface. *Nature Physics* **5,** 18 (2009).

73. Chen, Y. L. *et al.* Massive Dirac fermion on the surface of a magnetically doped topological insulator. *Science* **329,** 659–662 (2010).

74. Xi, X. *et al.* Signatures of a Pressure-Induced Topological Quantum Phase Transition in BiTeI. *Physical Review Letters* **111,** 155701 (2013).

75. Chen, Y. *et al.* High-Pressure Phase Transitions and Structures of Topological Insulator BiTeI. *Journal of Physical Chemistry C* **117,** 25677–25683 (2013).

76. Tran, M. K. *et al.* Infrared- and Raman-Spectroscopy Measurements of a Transition in the Crystal Structure and a Closing of the Energy Gap of BiTeI under Pressure. **112,** 047402 (2014).

77. Ideue, T. *et al.* Pressure variation of Rashba spin splitting toward topological transition in the polar semiconductor BiTeI. *Physical Review B* **90,** 161107 (2014).

78. VanGennep, D *et al.* Pressure tuning the Fermi level through the Dirac point of giant Rashba semiconductor BiTeI. *Journal of Physics Condensed Matter* **26,** 342202 (2014).

79. Park, J. *et al.* Quantum Oscillation Signatures of Pressure-induced Topological Phase Transition in BiTeI. *Scientific Reports* **5,** 15973 (2015).

80. Berry M, V. Quantal phase factors accompanying adiabatic changes. *Proceedings of the Royal Society of London Series A* **392,** 45–57 (1984).

81. Mikitik, G. P. & Sharlai, Y. V. Manifestation of Berry's Phase in Metal Physics. *Physical Review Letters* **82,** 2147 (1999).

82. Fu, L. & Kane, C. L. Topological insulators with inversion symmetry. *Physical Review B* **76,** 045302 (2007).

83. Murakawa, H *et al.* Detection of Berry's phase in a Bulk Rashba semiconductor. *Science* **342,** 1490–1493 (2013).

84. Bell, C *et al.* Shubnikov-de Haas oscillations in the bulk Rashba semiconductor BiTeI. *Physical Review B* **87,** 081109 (2013).

85. Ye, L., Checkelsky, J. G., Kagawa, F. & Tokura, Y. Transport signatures of Fermi surface topology change in BiTeI. *Physical Review B* **91,** 201104 (2015).

86. Ideue, T *et al.* Thermoelectric probe for Fermi surface topology in the three-dimensional Rashba semiconductor BiTeI. *Physical Review B* **92,** 115144 (2015).

87. Butler, C. J. *et al.* Mapping polarization induced surface band bending on the Rashba semiconductor BiTeI. *Nature Communications* **5,** 4066 (2014).

88. King, P. D. C., Veal, T. D. & McConville, C. F. Nonparabolic coupled Poisson-Schrödinger solutions for quantized electron accumulation layers: Band bending, charge profile, and subbands at InN surfaces. *Physical Review B* **77,** 125305 (2008).

89. Fu, L. Hexagonal warping effects in the surface states of the topological insulator Bi_2Te_3. *Physical Review Letters* **103,** 266801 (2009).

90. Frantzeskakis, E. & Grioni, M. Anisotropy effects on Rashba and topological insulator spin-polarized surface states: A unified phenomenological description. *Physical Review B* **84,** 155453 (2011).

91. Souma, S. *et al.* Direct measurement of the out-of-plane spin texture in the Dirac-cone surface state of a topological insulator. *Physical Review Letters* **106,** 216803 (2011).

92. Kane, E. O. Band structure of indium antimonide. *Journal of Physics and Chemistry of Solids* **1,** 249–261 (1957).

93. Michiardi, M. *et al.* Strongly anisotropic spin-orbit splitting in a two-dimensional electron gas. *Physical Review B* **91,** 035445 (2015).

94. Vajna, S. *et al.* Higher-order contributions to the Rashba-Bychkov effect with application to the Bi/Ag(111) surface alloy. *Physical Review B* **85,** 075404 (2012).

95. Osikowicz, W. *et al.* Site-specific electronic structure of an oligo - ethylenedioxythiophene derivative probed by resonant photoemission. *New Journal of Physics* **7,** 104 (2005).

96. Magnuson, M. *Electronic Structure Studies Using Resonant X-Ray and Photoemission Spectroscopy* PhD thesis (University of Uppsala, Sweden, 1999).

97. Fano, U. Effects of Configuration Interaction on Intensities and Phase Shifts. *Physical Review* **124,** 6 (1961).

98. Guillot, C. *et al.* Resonant Photoemission in Nickel Metal. *Physical Review Letters* **39,** 1632–1635 (1977).

99. Gudat, W, Alvarado, S, Campagna, M & Pëtroff, Y. Optics and photoemission Fano-resonances, surface and bulk effects in photoemission from the rare earths. *Journal de Physique Colloques* **41** (1980).

100. Marinho, R. R. T. *et al.* Interference between direct and resonant channels in near-resonance photoemission in argon. *Physical Review A* **63,** 032514 (2001).

101. Sistrunk, E. *et al.* Resonant photoemission at the iron M-edge of $Fe(CO)_5$. *Journal of Chemical Physics* **139,** 164318 (2013).

102. Yeh, J. J. & Lindau, I. Atomic subshell photoionization cross sections and asymmetry parameters: $1 \leq Z \leq 103$. *Atomic Data and Nuclear Tables* **32,** 1–155 (1985).

103. Cao, Y. *et al.* Coupled Spin-Orbital Texture in a Prototypical Topological Insulator. *arXiv:1211.5998* (2014).

104. Mapping the orbital wavefunction of the surface states in three-dimensional topological insulators. *Nature Physics* **9,** 499–504 (2013).

105. Zhu, Z. H. *et al.* Layer-by-layer entangled spin-orbital texture of the topological surface state in Bi_2Se_3. *Physical Review Letters* **110,** 216401 (2013).

106. Bawden, L. *et al.* Hierarchical spin-orbital polarisation of a giant Rashba system. *Science Advances* **1,** 1500495 (2015).

107. Zhang, H., Liu, C. X. & Zhang, S. C. Spin-orbital texture in topological insulators. *Physical Review Letters* **111,** 066801 (2013).

108. Jozwiak, C. *et al.* Photoelectron spin-flipping and texture manipulation in a topological insulator. *Nature Physics* **9,** 293–298 (2013).

109. Zhu, Z. H. *et al.* Photoelectron spin-polarization control in the topological insulator Bi_2Se_3. *Physical Review Letters* **112,** 076802 (2014).

110. Xie, Z. *et al.* Orbital-selective spin texture and its manipulation in a topological insulator. *Nature Communications* **5,** 3382 (2014).

111. Maaß, H. *et al.* Spin-texture inversion in the giant Rashba semiconductor BiTeI. *Nature Communications* **7,** 11621 (2016).

112. Xu, S.-Y. *et al.* Topological phase transition and texture inversion in a tunable topological insulator. *Science* **332,** 6029 (2011).

113. Bahramy, M. S. *et al.* Emergent quantum confinement at topological insulator surfaces. *Nature Communications* **3,** 1157–1159 (2012).

114. Park, S. R. *et al.* Chiral orbital-angular momentum in the surface states of Bi_2Se_3. *Physical Review Letters* **108,** 046805 (2012).

115. Park, J. H., Kim, C. H., Rhim, J. W. & Han, J. H. Orbital Rashba effect and its detection by circular dichroism angle-resolved photoemission spectroscopy. *Physical Review B* **85,** 195401 (2012).

116. Wang, Y. H. *et al.* Observation of a warped helical spin texture in Bi_2Se_3 from circular dichroism angle-resolved photoemission spectroscopy. *Physical Review Letters* **107,** 207602 (2011).

117. Jung, W. *et al.* Warping effects in the band and angular-momentum structures of the topological insulator Bi_2Te_3. *Physical Review B* **84,** 245435 (2011).

118. Crepaldi, A. *et al.* Momentum and photon energy dependence of the circular dichroic photoemission in the bulk Rashba semiconductors BiTeX (X = I, Br, Cl). *Physical Review B* **89,** 125408 (2014).

119. Neupane, M. *et al.* Oscillatory surface dichroism of the insulating topological insulator Bi_2Te_2Se. *Physical Review B* **88,** 165129 (2013).

120. Scholz, M. R. *et al.* Reversal of the circular dichroism in angle-resolved photoemission from Bi_2Te_3. *Physical Review Letters* **110,** 216801 (2013).

121. Ärrälä, M., Nieminen, J., Braun, J., Ebert, H. & Lindroos, M. Photon energy dependence of circular dichroism of the Au(111) surface state. *Physical Review B* **88,** 195413 (2013).

122. Noguchi, R. *et al.* Direct mapping of spin and orbital entangled wave functions under interband spin-orbit coupling of giant Rashba spin-split surface states. *Physical Review B* **95,** 041111 (2017).

123. Waugh, J. A. *et al.* Minimal Ingredients for Orbital Texture Switches at Dirac Points in Strong Spin-Orbit Coupled Materials. *NPJ Quantum Materials* **1,** 16025 (2016).

124. Liu, Q., Zhang, X., Waugh, J. A., Dessau, D. S. & Zunger, A. Orbital mapping of energy bands and the truncated spin polarization in three-dimensional Rashba semiconductors. *Physical Review B* **94,** 125207 (2016).

125. Raza, H. *Graphene Nanoelectronics* 1st ed. (Springer-Verlag Berlin, 2012).

126. Castro Neto, A. H., Guinea, F., Peres, N. M. R., Novoselov, K. S. & Geim, A. K. The electronic properties of graphene. *Reviews of Modern Physics* **81,** 109–162 (2009).

127. Saito, R, Dresselhaus, G. & Dresselhaus, M. S. *Physical Properties of Carbon Nanotubes* 1st ed. (Imperial College Press, London, UK, 1998).

128. Wallace, P. R. The Band Theory of Graphite. *Physical Review* **71,** 9 (1947).

129. Xiao, D., Liu, G. B., Feng, W., Xu, X. & Yao, W. Coupled spin and valley physics in monolayers of MoS_2 and other group-VI dichalcogenides. *Physical Review Letters* **108,** 196802 (2012).

130. Mattheiss, L. F. Band structures of transition-metal-dichalcogenide layer compounds. *Physical Review B* **8,** 3719 (1973).

131. Doran, N. J., Ricco, B, Titterington, D. J. & Wexler, G. A tight binding fit to the bandstructure of 2H-$NbSe_2$ and NbS_2 A tight binding fit to the bandstructure of 2H-$NbSe_2$ and NbS_2. *Journal of Physics C: Solid State Physics* **11** (1978).

132. Xu, X., Yao, W., Xiao, D. & Heinz, T. F. Spin and pseudospins in layered transition metal dichalcogenides. *Nature Physics* **10,** 343–350 (2014).

133. Zeng, H., Dai, J., Yao, W., Xiao, D. & Cui, X. Valley polarization in MoS_2 monolayers by optical pumping. *Nature Nanotechnology* **7,** 490–493 (2012).

134. Mak, K. F., He, K., Shan, J. & Heinz, T. F. Control of valley polarization in monolayer MoS_2 by optical helicity. *Nature Nanotechnology* **7,** 494–498 (2012).

135. Cao, T. *et al.* Valley-selective circular dichroism of monolayer molybdenum disulphide. *Nature Communications* **3,** 887 (2012).

136. Suzuki, R. *et al.* Valley-dependent spin polarization in bulk MoS_2 with broken inversion symmetry. *Nature Nanotechnology* **9,** 611–617 (2014).

137. Sugawara, K., Sato, T., Tanaka, Y., Souma, S. & Takahashi, T. Spin- and valley-coupled electronic states in monolayer WSe_2 on bilayer graphene. *Applied Physics Letters* **107,** 071601 (2015).

138. Wilson, J. A. & Yoffe, A. D. The transition metal dichalcogenides discussion and interpretation of the observed optical, electrical and structural properties. *Advances in Physics* **18,** 193–335 (1969).

139. Chhowalla, M. *et al.* The chemistry of two-dimensional layered transition metal dichalcogenide nanosheets. *Nature Chemistry* **5,** 263–275 (2013).

140. Lee, H. N. S., Garcia, M., McKinzie, H. & Wold, A. The low-temperature electrical and magnetic properties of $TaSe_2$ and $NbSe_2$. *Journal of Solid State Chemistry* **1,** 190–194 (1970).

141. Wilson, J. A., Di Salvo, F. J. & Mahajan, S. Charge-density waves in metallic, layered, transition-metal dichalcogenides. *Physical Review Letters* **32,** 882–885 (1974).

142. Moncton, D., Axe, J. & DiSalvo, F. Study of Superlattice Formation in 2H-$NbSe_2$ and 2H-$TaSe_2$ by Neutron Scattering. *Physical Review Letters* **34,** 12 (1975).

143. Naito, M. & Tanaka, S. Electrical Transport Properties in 2H-NbS_2, $NbSe_2$, TaS_2 and $TaSe_2$. *Journal of the Physical Society of Japan* **51,** 219–227 (1982).

144. Peierls, R. E. *Quantum theory of solids* (Oxford University Press, UK, 2001).

145. Rossnagel, K. On the origin of charge-density waves in select layered transition-metal dichalcogenides. *Journal of Physics: Condensed Matter* **23,** 213001 (2011).

146. Kohn, W. Image of the fermi surface in the vibration spectrum of a metal. *Physical Review Letters* **2,** 393–394 (1959).

147. Moncton, D. E., Axe, J. D. & DiSalvo, F. J. Neutron scattering study of the charge-density wave transitions in 2H-$TaSe_2$ and 2H-$NbSe_2$. *Physical Review B* **16,** 801–819 (1977).

148. Borisenko, S. V. *et al.* Two Energy Gaps and Fermi-Surface 'Arcs' in $NbSe_2$. *Physical Review Letters* **102,** 166402 (2009).

149. Rahn, D. J. *et al.* Gaps and kinks in the electronic structure of the superconductor 2H-$NbSe_2$ from angle-resolved photoemission at 1 K. *Physical Review B* **85,** 224532 (2012).

150. Doran, N. J. A calculation of the electronic response function in 2H-$NbSe_2$ including electron-phonon matrix element effects. *Journal of Physics C: Solid State Physics* **11,** L959–L962 (1978).

151. Straub, T. *et al.* Charge-Density-Wave Mechanism in 2H-$NbSe_2$: Photoemission Results. *Physical Review Letters* **82,** 4504–4507 (1999).

152. Rossnagel, K. *et al.* Fermi surface of 2H-$NbSe_2$ and its implications on the charge-density-wave mechanism. *Physical Review B* **64,** 235119 (2001).

153. Valla, T. *et al.* Quasiparticle Spectra, Charge-DensityWaves, Superconductivity, and Electron-Phonon Coupling in 2H-$NbSe_2$. *Physical Review Letters* **92,** 086401 (2004).

154. Kiss, T. *et al.* Charge-order-maximized momentum-dependent superconductivity. *Nature Physics* **3,** 720–725 (2007).

155. Rice, T. M. & Scott, G. K. New mechanism for a charge-density-wave instability. *Physical Review Letters* **35,** 120–123 (1975).

156. Weber, F. *et al.* Extended phonon collapse and the origin of the charge-density wave in 2H-$NbSe_2$. *Physical Review Letters* **107,** 107403 (2011).

157. Flicker, F. & van Wezel, J. Charge order from orbital-dependent coupling evidenced by $NbSe_2$. *Nature Communications* **6** (2015).

158. Johannes, M., Mazin, I. & Howells, C. Fermi-surface nesting and the origin of the charge-density wave in $NbSe_2$. *Physical Review B* **73,** 205102 (2006).

159. Weber, F. *et al.* Optical phonons and the soft mode in 2H-$NbSe_2$. *Physical Review B* **87,** 245111 (2013).

160. Yokoya, T *et al.* Fermi Surface Sheet-Dependent Superconductivity in 2H-$NbSe_2$. *Science* **294,** 2518 (2001).

161. Zehetmayer, M. & Weber, H. W. Experimental evidence for a two-band superconducting state of $NbSe_2$ single crystals. *Physical Review B* **82,** 014524 (2010).

162. Noat, Y. *et al.* Signatures of multigap superconductivity in tunneling spectroscopy. *Physical Review B* **82,** 014532 (2010).

163. Huang, C. *et al.* Experimental evidence for a two-gap structure of superconducting $NbSe_2$: A specific-heat study in external magnetic fields. *Physical Review B* **76** (2007).

164. Boaknin, E *et al.* Heat Conduction in theVortex State of $NbSe_2$: Evidence for Multiband Superconductivity. *Physical Review Letters* **90,** 107202 (2003).

165. Fletcher, J. D. *et al.* Penetration depth study of superconducting gap structure of 2H-$NbSe_2$. *Physical Review Letters* **98,** 057003 (2007).

166. Hüfner, S. *Very High Resolution Photoelectron Spectroscopy* 1st ed. (Springer, Berlin-Heidelberg, 2007).

167. Zhang, X., Liu, Q., Luo, J.-W., Freeman, A. J. & Zunger, A. Hidden spin polarization in inversion-symmetric bulk crystals. *Nature Physics* **10,** 387–393 (2014).

168. Riley, J. M. *et al.* Direct observation of spin-polarized bulk bands in an inversion-symmetric semiconductor. *Nature Physics* **10,** 835–839 (2014).

169. Zeng, H. *et al.* Optical signature of symmetry variations and spin-valley coupling in atomically thin tungsten dichalcogenides. *Scientific Reports* **3,** 1608 (2013).

170. Grüner, G. *Density Waves in Solids* 1st ed. (Perseus Publishing, Cambridge MA, USA, 1994).

171. Grüner, G. The dynamics of spin-density waves. *Reviews of Modern Physics* **66,** 1 (1994).

172. Borisenko, S. V. *et al.* Pseudogap and charge density waves in two dimensions. *Physical Review Letters* **100,** 196402 (2008).

173. Rossnagel, K., Rotenberg, E., Koh, H., Smith, N. V. & Kipp, L. Fermi surface, charge-density-wave gap, and kinks in 2H-$TaSe_2$. *Physical Review B* **72,** 121103 (2005).

174. Inosov, D. S. *et al.* Temperature-dependent Fermi surface of 2H -$TaSe_2$ driven by competing density wave order fluctuations. *Physical Review B* **79,** 125112 (2009).

175. Sigrist, M. *Introduction to unconventional superconductivity* **165,** 165–243 (2005).

176. Sigrist, M. *Introduction to unconventional superconductivity in non - centrosymmetric metals* **55,** 55–96 (2009).

177. Gor'kov, L. P. & Rashba, E. I. Superconducting 2D system with lifted spin degeneracy: mixed singlet-triplet state. *Physical review letters* **87,** 037004 (2001).

178. Smidman, M., Salamon, M. B., Yuan, H. Q. & Agterberg, D. F. Superconductivity and spin-orbit coupling in non-centrosymmetric materials: a review. *Reports on Progress in Physics* **80,** 036501 (2017).

179. Sigrist, M. *et al.* Superconductors with staggered non-centrosymmetricity. *Journal of the Physical Society of Japan* **83,** 6 (2014).

180. Liu, C.-X. Unconventional superconductivity in bilayer transition metal dichalcogenides. *Physical Review Letters* **118,** 087001 (2017).

181. Yoshida, T., Sigrist, M. & Yanase, Y. Pair-density wave states through spin-orbit coupling in multilayer superconductors. *Physical Review B* **86,** 134514 (2012).

182. Saito, Y. *et al.* Superconductivity protected by spin-valley locking in ion-gated MoS_2. *Nature Physics* **12,** 144–149 (2015).

183. Lu, J. M. *et al.* Evidence for two-dimensional Ising superconductivity in gated MoS_2. *Science* **350,** 1353–1357 (2015).

184. Xi, X. *et al.* Ising pairing in superconducting $NbSe_2$ atomic layers. *Nature Physics* **12,** 139–144 (2015).

185. Tinkham, M. *Introduction to superconductivity* 2nd ed. (McGraw-Hill, 1996).

186. Razzoli, E. *et al.* Selective Probing of Hidden Spin-Polarized States in Inversion-Symmetric Bulk MoS_2. *Physical Review Letters* **118,** 086402 (2017).

187. Mo, S.-K. *et al.* Spin-resolved photoemission study of epitaxially grown $MoSe_2$ and WSe_2 thin films. *Journal of Physics: Condensed Matter* **28,** 454001 (2016).